

AD-780 563

**BLEACHABLE ABSORBER LASER AMPLIFIER
AND DETECTOR (BALAD)**

James T. LaTourrette, et al

Polytechnic Institute of New York

Prepared for:

**Advanced Research Projects Agency
Rome Air Development Center**

February 1974

DISTRIBUTED BY:

NTIS

**National Technical Information Service
U. S. DEPARTMENT OF COMMERCE
5285 Port Royal Road, Springfield Va. 22151**

UNCLASSIFIED

SECURITY CLASSIFICATION OF THIS PAGE (When Data Entered)

REPORT DOCUMENTATION PAGE		READ INSTRUCTIONS BEFORE COMPLETING FORM	
1. REPORT NUMBER RADC-TR-74-60		2. GOVT ACCESSION NO.	3. RECIPIENT'S CATALOG NUMBER AD-780 563
4. TITLE (and Subtitle) BLEACHABLE ABSORBER LASER AMPLIFIER AND DETECTOR: Balad		5. TYPE OF REPORT & PERIOD COVERED Final 1 Jan 72 - 31 Dec 72	
7. AUTHOR(s) James T. LaTourrette S.Y. Szeto Maurice Newstein N. Wright		6. PERFORMING ORG. REPORT NUMBER PINYEP-74-136	
9. PERFORMING ORGANIZATION NAME AND ADDRESS Polytechnic Institute of New York 333 Jay St Brooklyn, NY 11201		8. CONTRACT OR GRANT NUMBER(s) F30602-72-C-0245	
11. CONTROLLING OFFICE NAME AND ADDRESS Advanced Research Projects Agency The Pentagon, Room 3D148 Washington, D.C. 20301		10. PROGRAM ELEMENT, PROJECT, TASK AREA & WORK UNIT NUMBERS 12790011	
14. MONITORING AGENCY NAME & ADDRESS (if different from Controlling Office) Rome Air Development Center OCTP Griffiss AFB, NY 13441		12. REPORT DATE Feb 74	
		13. NUMBER OF PAGES 99	
		15. SECURITY CLASS. (of this report) UNCLASSIFIED	
		15a. DECLASSIFICATION/DOWNGRADING SCHEDULE	
16. DISTRIBUTION STATEMENT (of this Report) Approved for public release; distribution unlimited.			
17. DISTRIBUTION STATEMENT (of the abstract entered in Block 20, if different from Report)			
18. SUPPLEMENTARY NOTES Reproduced by NATIONAL TECHNICAL INFORMATION SERVICE U S Department of Commerce Springfield VA 22151			
19. KEY WORDS (Continue on reverse side if necessary and identify by block number) Laser amplifier Absorber Sulfur hexafluoride Low-noise detector Laser receiver Bleachable absorber Optical waveguide Coherent detector Laser detector Saturable absorber Optical radar Narrow band filter CO ₂ laser Gaseous absorber Optical Communications Spatial filter Xenon laser Optical filter Wide-angle detector			
20. ABSTRACT (Continue on reverse side if necessary and identify by block number) This report describes the continued development of the wide-angle, low noise BALAD receiver (Bleachable Absorber Laser Amplifier and Detector). A xenon-xenon 3.5um BALAD receiver system has been tested. Experimental results are given. The experiments were hampered by excess noise in the xenon absorber discharge. The three dimensional analysis of the propagation of coherent optical pulses with limited transverse extent, predicts a non-linear self-focusing effect. A modified design of the BALAD receiver using a geometrical loss filter			

**BLEACHABLE ABSORBER LASER AMPLIFIER AND DETECTOR
(BALAD)**

**James T. LaTourrette
Maurice Newstein
S. Y. Szeto
N. Wright**

**Contractor: Polytechnic Institute of New York
(formerly Polytechnic Institute of Brooklyn)
Contract Number: F30602-72-C-0245
Effective Date of Contract: 1 January 1972
Contract Expiration Date: 31 December 1972
Amount of Contract: \$96,730.00
Program Code Number: OE20**

**Principal Investigator: G. Gould
Phone: 516 694-5500**

**Project Engineer: J. LaTourrette
Phone: 516 694-5500**

**Contract Engineer: W. C. Quinn
Phone: 315 330-4381**

**Approved for public release;
distribution unlimited.**

**This research was supported by the
Defense Advanced Research Projects
Agency of the Department of Defense
and was monitored by W.C. Quinn
RADC (OCTP), GAFB, NY 13441 under
Contract F30603-72-C-0245.**

UNCLASSIFIED

SECURITY CLASSIFICATION OF THIS PAGE(When Data Entered)

based on this effect is presented and analyzed. The design would facilitate the rejection of noise from the other laser amplifier transitions

UNCLASSIFIED

SECURITY CLASSIFICATION OF THIS PAGE(When Data Entered)

TABLE OF CONTENTS

	<u>Page</u>
Abstract	iii
List of Figures	vi
List of Tables	vi
1.0 Summary	1
1.1 Objective	1
1.2 Background	1
1.3 Plan	1
1.4 Technical Problems, Methodology, and Results	2
1.4.1 Experimental Study of the Xenon-Xenon BALAD Receiver System	2
1.4.2 Transverse and Spatial Evolution of Optical Pulses in a Saturated Absorber	3
1.4.3 Possible Improved Design of the BALAD Receiver Using Non-Linear Self-Focussing	3
1.5 Implications for the Department of Defense	3
1.6 Implications for further Research and Development	3
2.0 Experimental Study of a Xenon-Xenon BALAD Receiver System	4
2.1 Introduction	4
2.2 Equipment	4
2.2.1 Power Supplies	4
2.2.2 Detectors	4
2.2.3 Oscilloscope	4
2.2.4 Gas Handling and Vacuum Station	4
2.2.5 Optical Bench	5
2.3 Structure of the Plasma Tubes	5
2.3.1 He-Xe Laser	5
2.3.2 He-Xe Amplifier	5
2.3.3 Xe Absorber	6
2.4 Experimental Study of the Components of the Xenon-Xenon BALAD System	6
2.4.1 The Xenon Absorption Coefficient Versus Discharge Current	6
2.4.2 The Absorption Coefficient Versus Input Power	8
2.4.3 The Output Power Versus Frequency	10
2.5 Transmission Characteristics of the BALAD System	16
2.6 Conclusions of the Experimental Study	24
3.0 Theoretical Investigation of Coherence Pulse Propagation and Self-Focussing of Coherent Pulses	25
3.1 Introduction	25
3.2 Field and Material System Equations	26
3.3 Transverse Effects in Absorbers	28
3.3.1 One Dimension	28
3.3.2 Three Dimensions	29
3.4 Summary	32
4.0 Possible Improvements in the BALAD Receiver System	34
4.1 Comments on Alternative BALAD Geometries	34
4.2 The Application of Non-Linear Self-Focussing to a Geometrical Loss Filter	38
4.3 Design of a Geometrical Loss Filter Using Non-Linear Self-Focussing	38
4.4 The Geometrical Loss Filter - A Universal Attenuator	44

TABLE OF CONTENTS (Con't.)

	<u>Page</u>
5.0 System Hazard Analysis.....	46
6.0 Conclusions and Recommendations	48
References.....	50
Appendix A - Propagation of a CW Gaussian Beam in a Saturable Absorber.....	A-1
Appendix B - Analysis and Description of Numerical Procedure.....	B-1

LIST OF FIGURES

<u>Figure</u>	<u>Page</u>
1 Xenon absorption cell structure with hot cathode.....	7
2 Absorption coefficient of 5mm I.D. Xenon absorber vs. d.c. discharge current	9
3a Transmission characteristics of Xenon absorber vs. input power	11
3b Transmission characteristics of Xenon absorber vs. input power	12
4 Weak signal transmission of the Xenon absorber while it is saturated by a strong signal vs. short cavity tuning length. Horizontal scale is approximately 8.84MHz/box.....	14
5 Experimental set-up for measurements of transmission character- istics of a Xe-Xe BALAD system	17
6a Transmission characteristics of He-Xe amplifier vs. input power	19
6b Transmission characteristics of He-Xe amplifier vs. input power	20
7 Transmission characteristics of the Xe-Xe BALAD system vs. input power	21
8 Absorber, one dimensional propagation.....	30
9 Absorber, three dimensions	31
10 Absorber, three dimensions	33
11a BALAD receiver	35
11b BALAD receiver	35
12 BALAD receiver with optical waveguides	36
13 BALAD receiver with Fly's Eye Lens Train.....	37
14 BALAD receiver with a Self-Focussing Saturable Absorber	39
15 Aspects of geometrical filters	41
A.1 Beam radius vs. frequency deviation	A-13
A.2 Wave front curvature	A-14
B.1 Main subroutine.....	B-5
B.2 Integration subroutine SUM.....	B-6
B.3 Integration subroutine SUM.....	B-7
B.4 Evaluation of the eigenvalues for the amplification matrix of the numerical scheme.....	B-12

LIST OF TABLES

<u>Table</u>	<u>Page</u>
1 Xe-Xe BALAD Receiver Characteristics.....	49

1.0 SUMMARY

1.1 Objective

The objective of this contract is the investigation of Saturable Absorbers at 10.6μ and 3.5μ , and their application to BALAD receivers.

1.2 Background

In the BALAD (Bleachable Absorber Laser Amplifier and Detector) concept, the gaseous absorber is designed to saturate at an average intensity above the amplified spontaneous emission. Thus, the spontaneous emission and other background light is absorbed. The bleachable gas acts as an optical squelch filter suppressing the background radiation which does not coincide with the signal beam in direction, polarization, frequency and time. In addition, the signal beam, being of somewhat higher intensity, is focused down on the absorber, "burns a hole" in it, and passes through with relatively little attenuation. Only light which is spatially coherent with the signal gets through to the detector.

During the first year's effort under Contract F30602-71-C-0024, a search was made for useful absorbers in the 10.6μ and 3.5μ ranges, and a design study was pursued. As a result, the gas SF_6 was found to possess adequate properties for the 10.6μ wavelength and xenon was found to have very good properties at 3.5μ . Demonstration of the BALAD principle at 3.5μ with xenon appeared to be much more straightforward and considerably less costly than a similar experiment at 10.6μ with SF_6 . The present effort is a logical continuation of the work previously performed under Contract F30602-71-C-0024, and includes the areas defined in Tasks 4.1.1 through 4.1.3.

1.3 Plan

The study and investigation for the development, design, test, and analysis of the concept of a Bleachable Absorber Laser Amplifier and Detector (BALAD) has been delineated into the following four tasks:

Task 4.1.1: Development of design techniques for the BALAD concept. In part this will involve refinement of the concepts developed under Contract F30602-71-C-0024.

Task 4.1.2: Develop techniques for filtering out radiation from all but the working line in the 10.6μ CO_2 laser amplifier and in amplifiers in the 3.5μ spectral range with the objective of determining the optimum technique to be used in a BALAD receiver.

Task 4.1.3: Experimental demonstration of a BALAD receiver utilizing xenon both as the absorbing and amplifying gases; in particular, using a pulse modulated xenon oscillator as a source, measure and compare with theoretical predictions the performance of the BALAD receiver as a function of input pulse energy,

duration and direction of propagation with respect to the parameters: pulse energy amplification, amplification bandwidth, absorber filter bandwidth, field of view, absorber geometry, no detection and false detection error rates in the pulsed case, signal to noise ratio in the CW case.

Task 4.1.4: System Safety Analysis. In the conduct of design and fabrication of hardware, a system safety analysis shall be performed and documented. These studies shall be in accordance with Paragraph 5.8.2.1 of MIL-STD-822 where applicable.

1.4 Technical Problems, Methodology, and Results

During this period a xenon-xenon BALAD receiver system has been operated and tested. The results are reported here. The results of the theoretical analysis of the propagation of a realistic optical pulse with limited transverse extent are also reported.

The theory predicts focusing of the optical pulse in a saturable absorber. An analysis is presented which illustrates how this effect can be utilized to improve the BALAD receiver system. The following subsections summarize the developments in each of these topics.

1.4.1 Experimental Study of the Xenon-Xenon BALAD Receiver System

A BALAD receiver is composed of a laser preamplifier and a saturable absorber. In the present case, both components employ xenon as the active medium.

The desired conditions of high gain with a large saturation intensity in the amplifier, compared to high absorption and small saturation intensity in the absorber, were achieved by optimizing the operating conditions in each case. In the 1cm I.D. amplifier a gain coefficient of 31dB/m was achieved with a gas mixture of 2 Torr helium plus 0.1 Torr xenon and a current of 20mA. In the 0.5cm I.D. absorption cell, an absorption coefficient of 60dB/m was achieved with low saturation intensity using pure xenon at 0.1 Torr and a current of 125mA.

The experimental investigation of the performance of the amplifier and absorber, both separately and combined together as a BALAD receiver system is described in Section 2.4. The general performance was in agreement with the theoretical predictions. However, the detailed investigation of the signal-to-noise properties of this BALAD receiver system was hampered by the noise generated by the xenon discharge in the absorption cell. We were unable to achieve quiet operation of this discharge under the conditions which produced the strong absorption.

1.4.2 Transverse and Spatial Evolution of Optical Pulses in a Saturated Absorber

The theoretical analysis of the propagation of an optical pulse in a saturated absorber has been significantly advanced. The analysis, which is described in Section 3, treats the realistic case of a pulse of limited transverse dimensions. The results indicate that a strong self focussing effect occurs. The implications of this effect are summarized in the next subsection and are discussed in Section 4. The propagation of a CW beam, which does not exhibit the self focussing effect, is discussed in Appendix A.

1.4.3 Possible Improved Design of the BALAD Receiver using Non-Linear Self-focussing

The existence of non-linear self-focussing suggests the possibility of using geometrical filtering to enhance the capabilities of the BALAD receiver. In the BALAD receiver as presently envisioned, the bleachable absorber must attenuate the amplified background noise by a large factor.

As detailed in the previous contract reports,¹ this required the use of a rather long absorber. However, as detailed in Section 4, non-linear self-focussing would allow the use of geometrical filtering to accomplish the required attenuation. The saturable absorber would then function primarily as a wave guide although the attenuation which it provides would still be beneficial.

1.5 Implications for the Department of Defense

The previous study¹ indicated that a BALAD receiver for 10.6 μm CO_2 laser signals as reported in RADC-TR-72-313, is feasible for application in an optical radar. Its usefulness would be to detect a target of uncertain position. For example, the receiver could be remote from the transmitter. The BALAD receiver could also sensitively receive several separated signals simultaneously, or even an entire image. The spatial and spectral resolution of a SF_6 saturable absorber in a BALAD receiver has been experimentally verified.

A BALAD receiver utilizing xenon gas could function in a shorter range but higher resolution optical radar than the CO_2 system. This wide-angle receiver also could be utilized in a lightweight secure communication system. Discharge noise in the xenon absorber may limit the usefulness of the xenon-xenon BALAD system.

1.6 Implications for Further Research and Development

The difficulties encountered with the xenon absorber discharge noise point up the need for further research to achieve quiet discharge conditions while achieving the desired high absorption coefficient.

The self focussing effect, indicated by the numerical analysis of the propagation of a spatially limited pulse in a saturated absorber should be investigated further. If the effect is sufficiently strong, it could result in a significant improvement in BALAD receiver design.

2.0 EXPERIMENTAL STUDY OF A XENON-XENON BALAD RECEIVER SYSTEM

2.1 Introduction

We have studied the properties of the BALAD receiver system composed of an He-Xe amplifier and an Xe absorber. Since the pure xenon discharge was observed to be noisy, in most of the measurements, phase sensitive detection was used to improve the signal-to-noise ratio.

2.2 Equipment

The supportive equipment used in these experiments, grouped by category, will be briefly described; after which, a more detailed discussion of the elements of the BALAD system will be given.

2.2.1 Power Supplies

Three high voltage, low ripple power supplies capable of operating in the range of (i) 5kV, 100mA, (ii) 20kV, 50mA, and (iii) 1kV, 500mA were used for the He-Xe laser, He-Xe amplifier, and the Xe absorber, respectively. A Kepco dc supply with range 10 V and 6 A was used for the hot cathode filament of the Xe absorption cell. Also a Lambda regulated 500 volt dc supply was used to bias the PZT transducer of the laser.

2.2.2 Detectors

A liquid nitrogen cooled (78°K) Ge-Au detector was used to detect the signal. The bandwidth of the detector is about 10MHz. The output from the detector was connected to a Princeton Applied Research JB5 lock-in amplifier. The reference frequency was set at 500Hz which was the frequency of the chopper. The response of the detection system was calibrated against an Epply thermopile. The laser output was monitored with a Philco L4530 InAs detector and an oscilloscope. A calibrated Epply thermopile with sensitivity 6mW/mV was used to calibrate all detectors. The thermopile voltage was measured with a Keithley microvolt-ammeter.

2.2.3 Oscilloscope

In all the measurements, a Tektronix Type 551 dual beam oscilloscope was used to monitor the laser signal and observe the noise properties of the system.

2.2.4 Gas Heating and Vacuum Station

The station consisted of a diffusion pump and a mechanical forepump. One liter bottles of helium and natural xenon from Matheson Gas Products were attached to the station by Granville-Philips variable leak valves. Gas pressures were measured with an MKS Baratron Capacitance Manometer. The plasma tubes of the He-Xe laser, the He-Xe amplifier, and the Xe absorber were attached to the station via Granville-Philips Type C valves. The vacuum station could be pumped down to 10^{-7} Torr after thorough baking of the glass walls and the valves by heating tapes.

2.2.5 Optical Bench

All of the experiments were performed on a 98" x 50" heavy cast iron bench. The bench was isolated from the floor by shock absorbing rubber pads.

2.3 Structure of the Plasma Tubes

The basic elements of the BALAD system were the xenon amplifier and xenon absorber. In addition, the signal source was a xenon laser.

2.3.1 He-Xe Laser

The He-Xe laser consisted of a 5mm I.D. quartz tube with a dc discharge length of 26 cm. The plasma tube had 2mm thick quartz windows oriented at Brewster's angle (56°). The quartz windows were sealed with B. F. Goodrich A-1177-B epoxy. In order to reduce cathoporesis of xenon during the dc discharge, a long non-excited by-pass was provided between the anode and the cathode. The anode was made of nickel and the cold cathode was made of aluminum alloy 2024. The plasma tube was mounted within the laser resonator which had three invar rods held in circular aluminum bulk-heads. The resonator mirror mounts had three point fine screw orientation adjustments. The resonator was a high-loss Fabry-Perot type.² It consisted of a gold-coated flat mirror on one end and a 1mm diameter gold dot on the center of a flat quartz substrate on the other end. The gold mirror was mounted on a stack of PZT elements which had a response of $53 \text{ \AA}/\text{volt}$. The useful laser output was the "diffraction loss" around the dot. The length of the resonator was 33.6 cm long which corresponds to a free spectral range of

$$\Delta\nu = \frac{c}{2L} = 447 \text{ MHz} .$$

Due to the large mode pulling effect, the actual oscillation range of the laser was determined to be only 239 MHz. Since the full doppler linewidth of xenon is about 110 MHz, single mode oscillation was obtained. During the experiments, the He-Xe laser was filled with a pressure of 3 Torr of helium and 0.08 Torr of xenon. With a 200 Ω ballast resistor, quiet operation with negligible excess noise was obtained at 10mA discharge current. The supply voltage was 3kV. The maximum CW output from the laser was about 0.2mW.

2.3.2 He-Xe Amplifier

Similar to the plasma tube structure of the He-Xe laser, the amplifier tube consisted of a 1 cm I.D. quartz tube and a dc discharge length of 69 cm. Quartz Brewster windows were used. There was a cold aluminum cathode, a large ballast volume, and an anode to cathode bypass. The amplifier was filled with 2 Torr of helium and 100mTorr of xenon. At a current of 20mA, the small signal gain coefficient of the amplifier was 31dB/m. The amplifier plasma tube was also mounted on a laser

structure as described in Section 2.3.1. During the hole burning effect observation in xenon absorber as will be described in Section 2.4.3, the He-Xe amplifier was converted to a laser by mounting two mirrors to form a high loss Fabry and Perot resonator. The dot reflector had a 1.5 mm diameter gold dot. The maximum output power from the laser was about 0.6 mW.

2.3.3 Xe Absorber

The absorption cell had a 5 mm I.D. and a dc discharge length of 20 cm. A hot cathode was used to avoid sputtering at high currents and low xenon pressures. The filament was made from a 12 cm long piece of RCA N91E1 oxide coated nickel filament wire. The long spiral filament was supported on a quartz tube to avoid sagging. Getters were included to aid in removing impurities. A by-pass was also provided between the anode and the cathode. Quartz windows were used. The windows were only slightly tilted from normal to the optic axis, to avoid feedback into the laser without causing a polarization dependent transmission through the cell. The structure of the absorption cell is shown in Fig. 1. The following procedure was used to process the hot cathode: The entire cell was first outgassed with heater tapes and pumped down to about 10^{-6} Torr. Then the filament was heated by enough current to increase the system pressure to no more than 10^{-5} Torr. The heater current was slowly increased until the filament was heated to a dull orange color. The getters were then fired. The whole tube was baked overnight again with heating tapes. The absorption cell was then filled with xenon as desired for the investigations.

2.4 Experimental Study of the Components of the Xenon-Xenon BALAD System

The absorption cell was first systematically studied as a separate system element. The amplifier was similarly studied and then the properties of the combined system were investigated.

2.4.1 The Xenon Absorption Coefficient Versus Discharge Current

The $3.5 \mu\text{m}$ signal from the He-Xe laser was chopped at 500 Hz in order to use phase sensitive detection of weak signals and to distinguish fluorescence from the absorber discharge. A 50% beam splitter was used to direct half of the laser power to an InAs detector. The other half of the laser output was sent, single pass, through the absorption cell. The InAs detector signal was amplified and displayed on an oscilloscope to monitor the input signal power and control the oscillation frequency near line center. The oscillation frequency was manually re-adjusted to the atomic line center by applying dc voltage to the PZT transducer. The output signal from the absorption cell was detected by a liquid nitrogen cooled Ge-Au detector. The output from the detector was fed into a lock-in amplifier. The reference signal was derived from the chopper. A plot of the absorption coefficient (dB/m) versus discharge current

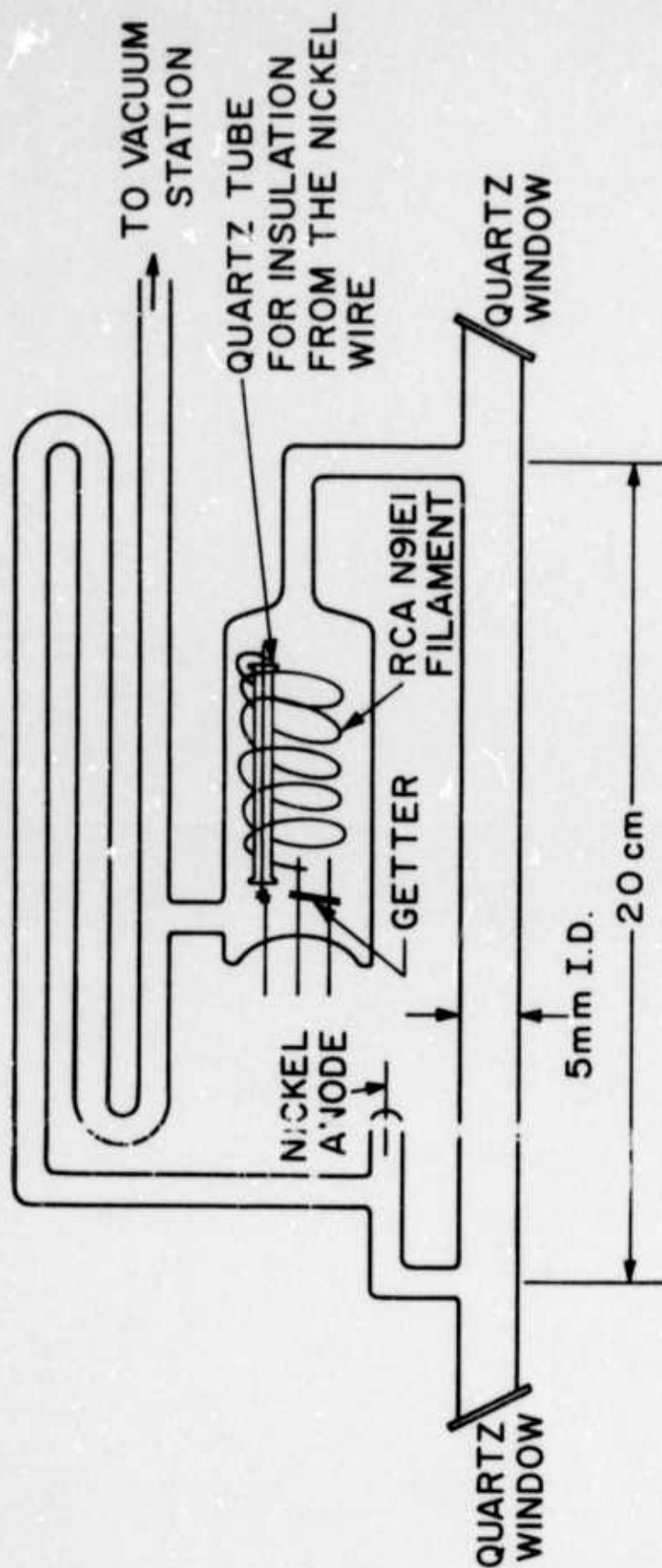


Fig. 1 - Xenon absorption cell structure with hot cathode

of the xenon absorber is shown in Fig. 2. It can be seen from the figure that maximum absorption of ~60dB/m can be achieved at a pressure of 100mTorr and at a current of 125mA. Comparing this to previous data³ one finds that, quite analogous to the gain coefficient, the maximum absorption coefficient is inversely proportional to the tube diameter.

2.4.2 The Absorption Coefficient Versus Input Power

Our analysis of the saturation of absorption coefficient vs. input power is based on the work of C.P. Christensen et al.,⁴ who studied the gain versus input power characteristic in a CO₂ amplifier. The absorption coefficient for an inhomogeneously broadened medium is given by

$$-\frac{1}{I} \frac{dI}{dz} = \alpha = \frac{\alpha_0}{\sqrt{1 + \frac{I}{I_s}}} \quad (1)$$

where

α_0 is the small signal absorption coefficient

I is the intensity at z

I_s is the saturation intensity of the medium.

For small intensity, i.e., $I/I_s \ll 1$, Eq. (1) can be approximated by

$$-\frac{1}{I} \frac{dI}{dz} = \alpha_0 \left(1 - \frac{1}{2} \frac{I}{I_s}\right) \quad (2)$$

After integrating this equation over the length of the absorber L , the result is

$$\frac{I_{in}}{I_{out}} = e^{\alpha_0 L} \left(1 + \frac{e^{-\alpha_0 L} - 1}{2} \frac{I_{in}}{I_s}\right) \quad (3)$$

Equation (3) serves as a means to determine I_s in a plot of I_{in}/I_{out} vs. I_{in} .

If the laser beam has a constant size and shape throughout the absorber, the intensity can be integrated over the beam cross-section to yield a relation between the input and output power. For example, if the incident beam is Gaussian of the form $I_{in} = I_0 \exp(-r^2/\omega^2)$ where ω is the beam radius at $1/e$ intensity, then the power input is given by integrating over the area of the beam, i.e.,

$$P_{in} = \int_0^\infty I_{in} 2\pi r dr = I_0 (\pi \omega^2) \quad ,$$

or

$$I_{in} = \frac{P_{in}}{\pi \omega^2} \exp\left(-\frac{r^2}{\omega^2}\right) \quad (4)$$

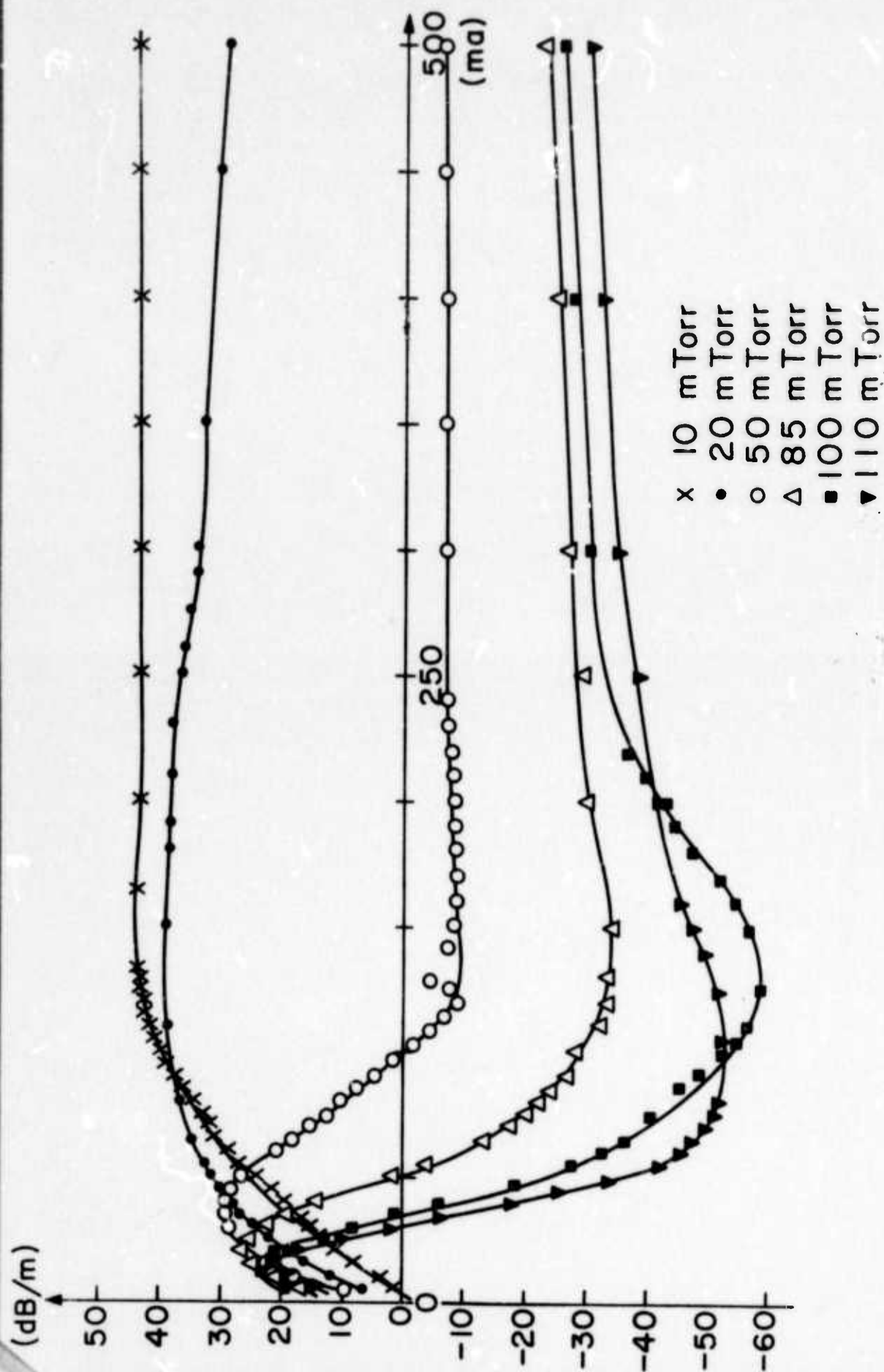


Fig. 2 - Absorption coefficient of 5 mm I.D. Xenon absorber vs. d.c. discharge current

Similarly, the output intensity is given by

$$I_{\text{out}} = \frac{P_{\text{out}}}{\pi \omega^2} \exp\left(-\frac{r^2}{\omega^2}\right) \quad (5)$$

Substituting these results into Eq. (3) and integrating over the cross-sectional area yields:

$$\frac{P_{\text{in}}}{P_{\text{out}}} = e^{a_o L} \left(1 + \frac{e^{-a_o L} - 1}{4} \frac{P_{\text{in}}}{\pi \omega^2 I_s} \right) \quad (6)$$

Equation (6) shows a straight line in the $P_{\text{in}}/P_{\text{out}}$ vs. P_{in} plot. The intercept at $(P_{\text{in}}/P_{\text{out}}) = 0$ gives the value of saturation intensity I_s which is

$$I_s = \frac{P_{\text{in}}}{\pi \omega^2} \left(\frac{1 - e^{-a_o L}}{4} \right) \quad (7)$$

A typical plot of the ratio of input power to output power vs. input power is shown in Figs. 3a and 3b. From Fig. 3b, the slope at the small input power gives an intercept at $16 \mu\text{W}$. The average beam size in the absorber was about $\omega = 0.5 \text{mm}$ and

$$e^{a_o L} = \frac{I_{\text{in}}}{I_{\text{out}}} \bigg|_{\text{max}} \approx 16$$

From Expression (7), the saturation intensity of the absorber is estimated to be $I_s \approx 0.51 \text{mW/cm}^2$ in good agreement with the previous measurements of xenon gain saturation.²

2.4.3 The Output Power Versus Frequency

The $3.5 \mu\text{m}$ output from a strong He-Xe laser was sent through the absorption cell after being collimated by a pair of concave mirrors with radii of curvature $R_1 = 92 \text{cm}$ and $R_2 = 42 \text{cm}$ used as a simple telescope. A weak signal from a second He-Xe laser which served as the probe signal was also directed through the above collimator before reaching the absorption cell. The weak beam was arranged to overlap the strong beam within the absorption cell, but it propagated at a small angle relative to the strong beam so that the beams could be separated and only the weak signal reached the Ge-Au detector. The frequency of the strong laser output was fixed. The PZT transducer of the weak laser was swept by a sawtooth output voltage from an oscilloscope to obtain the frequency tuning profile of its output power. A large amount of noise from the absorption cell was obtained along with the weak signal when the cell was operating at a current of 100mA and at a pressure of 100mTorr . It was impossible to observe the hole burning effect directly from the oscilloscope. Phase sensitive detection was

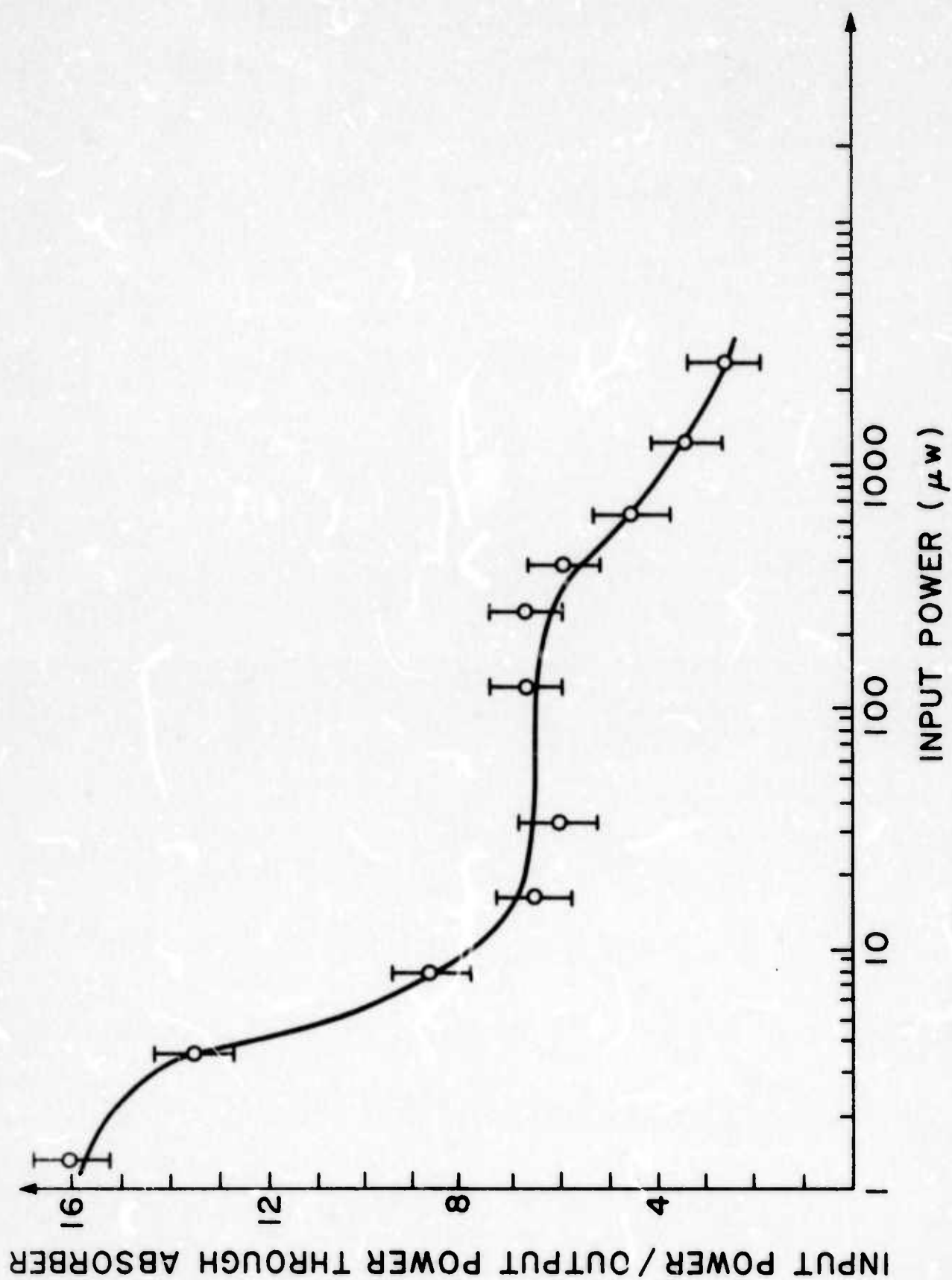


Fig. 3a - Transmission characteristics of x-ray absorber vs. input power

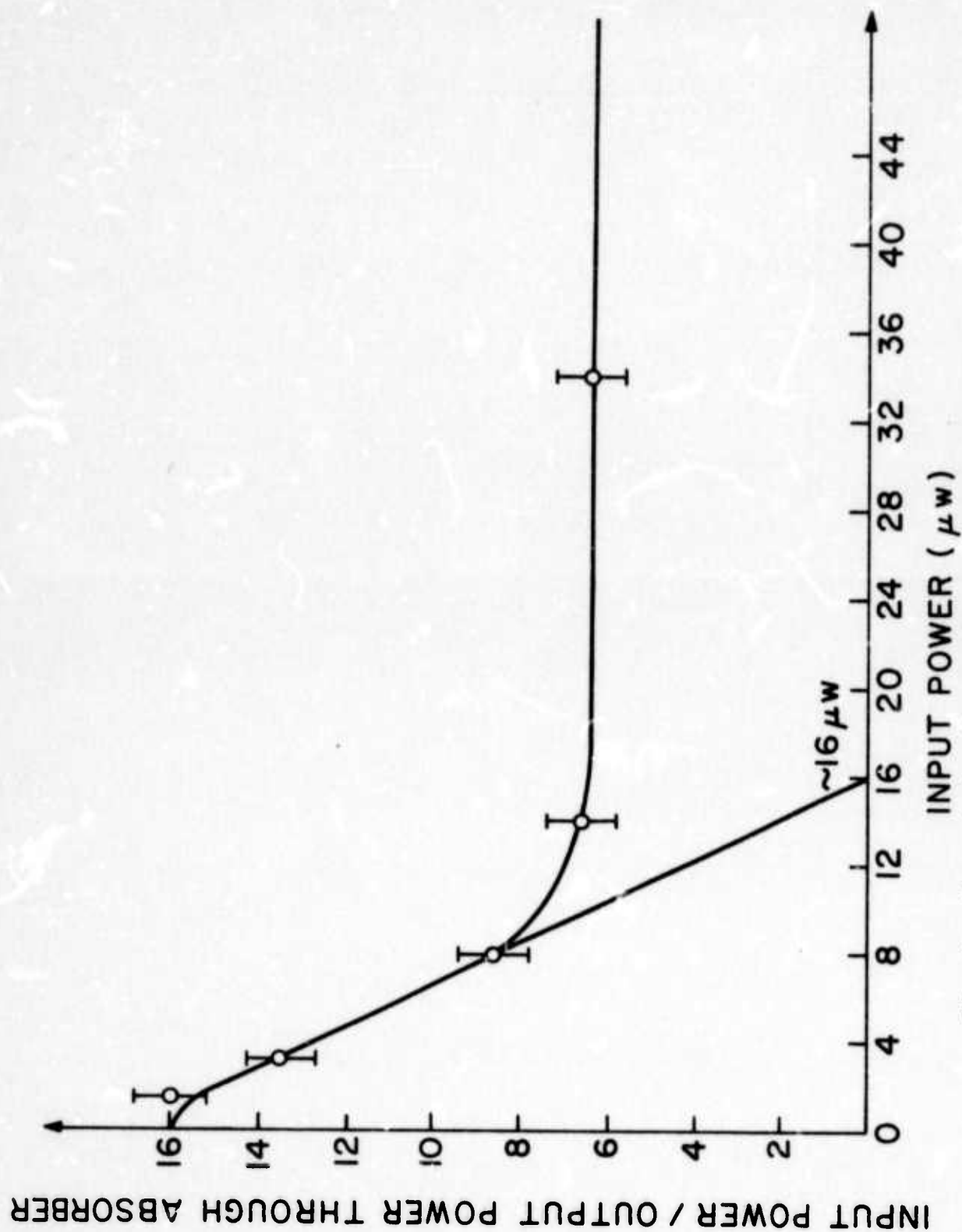


Fig. 3b - Transmission characteristics of xenon absorber vs. input power

used to improve the signal-to-noise ratio. The weak signal was chopped at 500Hz and sent through the absorption cell. The detected signal then went to a lock-in amplifier. The output from the lock-in amplifier was connected to the oscilloscope which was swept synchronously with the weak laser. The hole burning effect was observed as shown in Fig. 4.

The absorption coefficient of the weak signal in the presence of a strong saturating beam of intensity I at frequency ν_1 is given by

$$\alpha[\nu, I(\nu_1)] = \int_{-\infty}^{\infty} \sigma(\nu_{\xi}) \Delta N[\nu_{\xi}, I(\nu_1)] d\nu_{\xi} \quad (8)$$

where

$$\sigma(\nu_{\xi}) = \frac{\sigma_0}{1 + 4\left(\frac{\nu_{\xi} - \nu_0}{\Delta\nu}\right)^2} \quad (9)$$

$\Delta N[\nu_{\xi}, I(\nu_1)]$ is the population difference between the lower and upper state of the atom in the presence of a strong saturating signal,

ν_{ξ} is the atomic line center of those atoms with non-zero velocity,

ν_0 is the atomic line center of those atoms with zero velocity,

$\Delta\nu$ is the full homogeneous line width of the atom at half intensity,

$\sigma_0 = (\lambda/2\pi)^2 (1/t_s \Delta\nu)$ is the absorption cross-section of the atom,

λ is the wavelength of the laser,

t_s is the spontaneous lifetime of the atom.

If we neglect the fluctuation of the population due to the beat frequency between the two lasers, the population difference can be written as

$$\Delta N[\nu_{\xi}, I(\nu_1)] = \frac{\Delta N^0 p(\nu_{\xi})}{1 + \frac{I}{I_s} \frac{1}{1 + 4\left(\frac{\nu - \nu_1}{\Delta\nu}\right)^2}} \quad (10)$$

where

ΔN^0 is the population difference of the medium without incident field,

I_s is the saturation intensity of medium,

$p(\nu_{\xi})$ is the weighting function of the atom at ν_{ξ} with respect to ν_0 .

The latter quantity is given by

$$p(\nu_{\xi}) = \frac{2\sqrt{\ln 2}}{\sqrt{\pi} \Delta\nu_D} \exp\left[-\left(2\sqrt{\ln 2} \frac{\nu_{\xi} - \nu_0}{\Delta\nu_D}\right)^2\right] \quad (11)$$

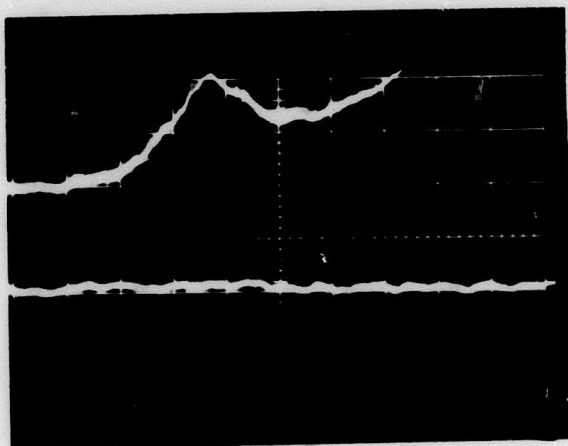


Fig. 4 - Weak signal transmission of the xenon absorber while it is saturated by a strong signal vs. short cavity tuning length. Horizontal scale is approximately 8.84 MHz/box

where

$$\Delta \nu_D = \sqrt{\frac{8 \ln^2 2 k T}{M c^2}} \nu_0 \text{ is the full doppler line width,}$$

k = Boltzmann's constant, T = temperature, M = atomic weight, and
 c = velocity of light.

Substituting Eqs. (9-11) into Eq. (8) and performing the integration in the limit of broad doppler line width, one finds

$$a[\nu, I(\nu_1)] = a_0(\nu) \left[1 - \frac{I/I_s}{\sqrt{1 + I/I_s} \left(1 + \sqrt{1 + I/I_s} \right)} \frac{1}{1 + 4 \left(\frac{\nu - \nu_1}{\Delta \nu (1 + \sqrt{1 + I/I_s})} \right)^2} \right] \quad (12)$$

where

$$a_0(\nu) = \Delta N^0 \frac{\lambda^2}{8 \pi t_s} \frac{2 \sqrt{\ln 2}}{\sqrt{\pi} \Delta \nu_D} \exp \left[- \left(2 \sqrt{\ln 2} \frac{\nu - \nu_0}{\Delta \nu_D} \right)^2 \right] \quad (13)$$

is the small signal absorption coefficient of the medium. From Eq. (12), we have at $\nu = \nu_1$

$$a(\nu_1) = \frac{a_0(\nu_1)}{\sqrt{1 + I/I_s}} \quad (14)$$

The output intensity I_{out} of the weak signal from an absorber of length L is related to the input intensity I_{in} by

$$I_{out} = I_{in} \exp(-aL) \quad (15)$$

where a is given by (12). At $\nu = \nu_1$, the weak signal output from the absorber in the presence of the strong signal can be obtained from (15), i.e., $I_{out} = I_{in} \exp[-a(\nu_1)L] = I_{in} \exp[-a_0(\nu_1)L/\sqrt{1 + (I/I_s)}]$. When there is no strong signal, the weak signal output from the absorber at $\nu = \nu_1$ is simply given by $I_{out} = I_{in} \exp[-a_0(\nu_1)L]$. The depth of the hole is thus given by the difference

$$I_{in} \left[\exp \left(- \frac{a_0 L}{\sqrt{1 + (I/I_s)}} \right) - \exp(-a_0 L) \right]$$

The full width of the hole at half of the hole depth can be obtained by solving the following equation

$$I_{in} e^{-a_0 L} + \frac{1}{2} I_{in} \left[\exp \left(\frac{-a_0 L}{\sqrt{1 + (I/I_s)}} \right) - \exp(-a_0 L) \right] = I_{in} e^{-a[\nu, I(\nu_1)]L}$$

which gives after some calculation

$$\left. \begin{array}{l} \text{full} \\ \text{hole} \\ \text{width} \end{array} \right\} = 2(\nu - \nu_1) = \Delta\nu \left(1 + \sqrt{1 + \frac{I}{I_s}} \right) \left\{ \frac{\frac{a_o L (I/I_s)}{\sqrt{1 + (I/I_s)} [1 + \sqrt{1 + (I/I_s)}]}}{\ln \frac{1}{2} \left[1 + \exp \left(a_o L - \frac{a_o L}{\sqrt{1 + (I/I_s)}} \right) \right]} - 1 \right\}^{1/2} \quad (16)$$

The experimental data gives at $\nu = \nu_1$,

$$\left. \frac{I_{in}}{I_{out}} \right|_{\max} = e^{a_o L} \approx 16$$

and

$$\left. \frac{I_{in}}{I_{out}} \right|_{\min} = \exp \left(\frac{a_o L}{\sqrt{1 + (I/I_s)}} \right) \approx 11$$

Hence one finds $(I/I_s) \approx 0.33$. From (16), we then obtain

$$2(\nu - \nu_1) \approx 1.97 \Delta\nu \quad (17)$$

The full natural line width of xenon at $3.5\mu\text{m}$ is about 3.66 MHz ,⁵ and the pressure broadening of the homogeneous line width is about 60 MHz/Torr .³ For 100 mTorr of xenon used in the absorber, the pressure broadened homogeneous line width is $\sim 6\text{ MHz}$. Hence we have $\Delta\nu \approx 9.75\text{ MHz}$. From Eq. (17), we can estimate the full width of the hole burned in the absorption curve is about 19 MHz which is in fair agreement with the measured 16 MHz width.

2.5 Transmission Characteristics of the BALAD System

The $3.5\mu\text{m}$ output from the He-Xe laser was sent through the He-Xe amplifier after reflection from a long radius concave mirror of $R = 500\text{ cm}$. The amplified beam was focused into the center of the Xe absorber by a short radius concave mirror of $R = 41.8\text{ cm}$. The output from the absorber was collected by a concave mirror of $R = 30\text{ cm}$ onto a Ge-Au detector at 77°K . Phase sensitive detection was used in the measurements as described in Section 2.4.1. A beam splitter was used to monitor part of the laser output. The schematic diagram of the experimental set up is given in Fig. 5. Part of the signal from the Ge-Au detector was fed to the oscilloscope to observe the signal and noise properties of the BALAD system. Glass microscope slides were used to attenuate the laser output power. The slides have an attenuation factor of about 50 percent.

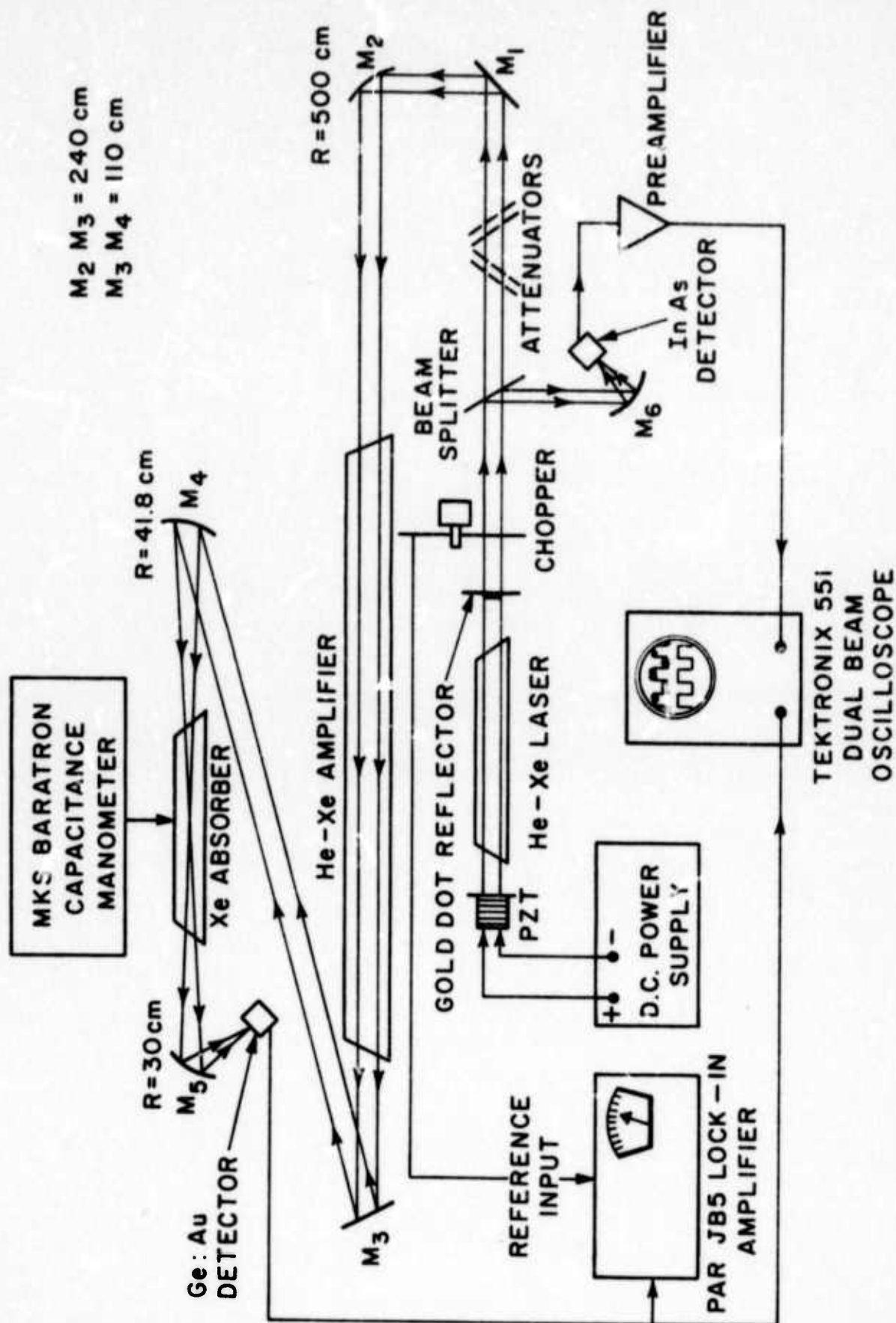


Fig. 5 - Experimental set-up for measurements of transmission characteristics of a Xe-Xe BALAD system

The following procedures were followed during the measurements. The signal power from the He-Xe laser was measured by the lock-in amplifier with the discharge in both the amplifier and absorber off. The noise voltage of the signal was measured from the oscilloscope. Then the amplifier was turned on. The amplified signal power and the noise were measured by the lock-in amplifier and the oscilloscope. Finally, both the amplifier and the absorber were turned on and the transmitted signal power and noise were measured. The glass attenuators were inserted in front of the laser one at a time and the above procedure was repeated. During the experiment, the current of the He-Xe laser was fixed and the laser oscillation frequency was readjusted to the line center by manual control of the laser PZT transducer voltage. The amplifier pressure was 2 Torr of helium and 100mTorr of xenon. The discharge current was maintained at 20mA. The xenon pressure in the absorber was 100mTorr and the discharge current was maintained at about 125mA. The plot of transmission (= output power/input power) vs. input power for the amplifier and the BALAD system are shown in Figs. 6a, 6b, and 7. In the case of absorber, the ratio input power/output power vs. input power is plotted in Figs. 3a and 3b.

For the high helium and xenon pressure used in the amplifier, the gain becomes essentially homogeneously broadened.⁶ The saturation intensity of the amplifier can be roughly determined by the intercept of the slope at small input power by the relation⁴

$$I_s = \frac{P_{in}}{\pi \omega^2} \left(\frac{e^{a_o L}}{2} - 1 \right) \quad (18)$$

From Fig. 6b, one finds $P_{in} \approx 12.6 \mu W$,

$$\left. \frac{P_{out}}{P_{in}} \right|_{\max} = e^{a_o L} = 130$$

and the beam size in the amplifier is about $\omega = 3 \text{ mm}$. The saturation intensity of the amplifier is calculated from Eq. (18) to be about 2.5 mW/cm^2 .

Figure 7 shows a peak in the transmission of the signal through the BALAD system which occurs at input power to the amplifier of about $0.28 \mu W$. Since the saturation intensity of xenon absorber is very small, saturation processes started when the signal power to the amplifier was only $0.02 \mu W$. At such an input power, the amplifier was not saturated. The input signal was amplified by a factor of one hundred and thirty times through the amplifier to give an input of $2.6 \mu W$ to the absorber. At the above input power, there was only about a factor of 14.5 attenuation through the absorber as compared to the factor of 16 unsaturated small signal attenuation. Hence there was a relative increase of signal power through the BALAD system. As the input signal level

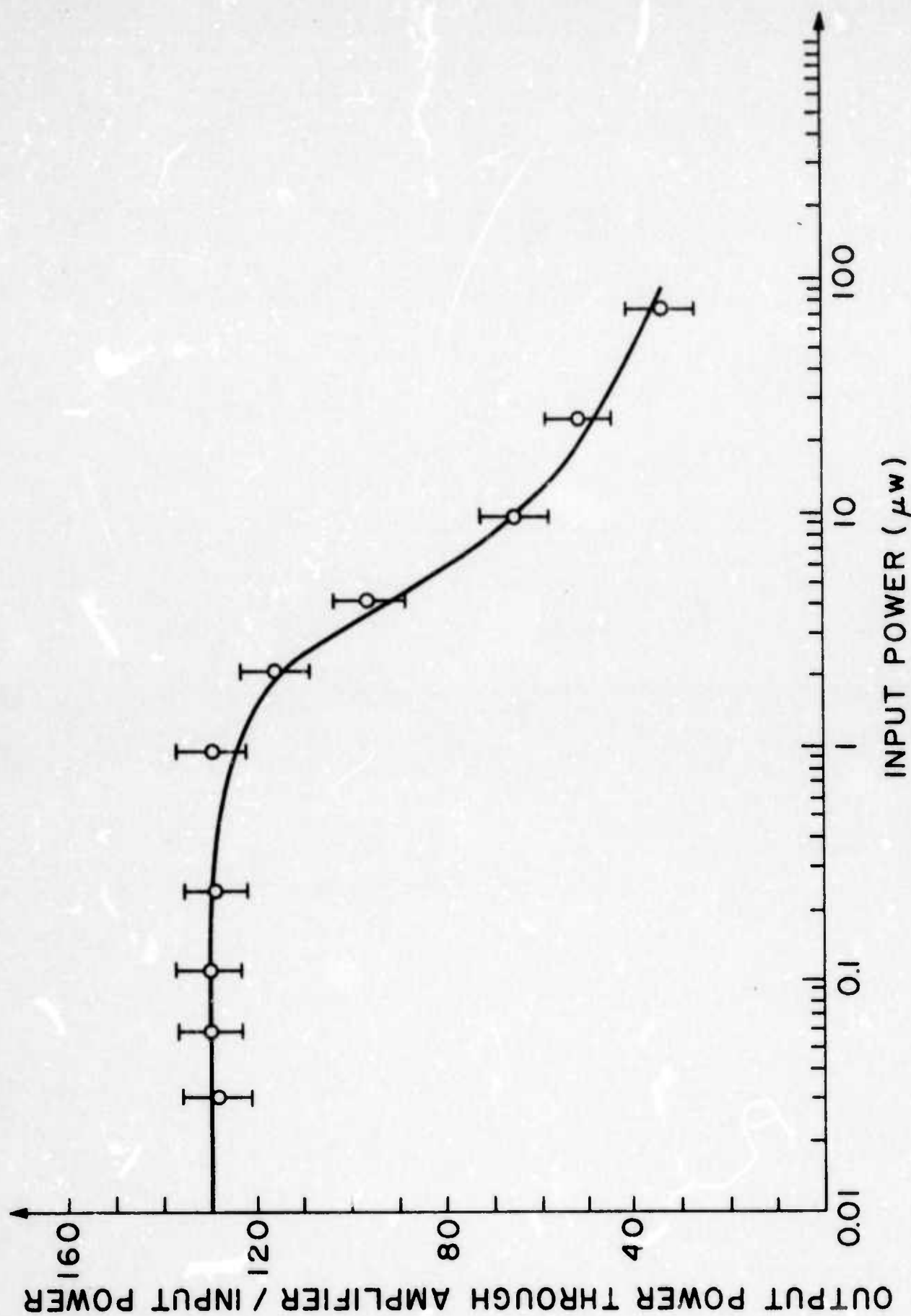


Fig. 6a - Transmission characteristics of He-Ne amplifier at p.p.w.

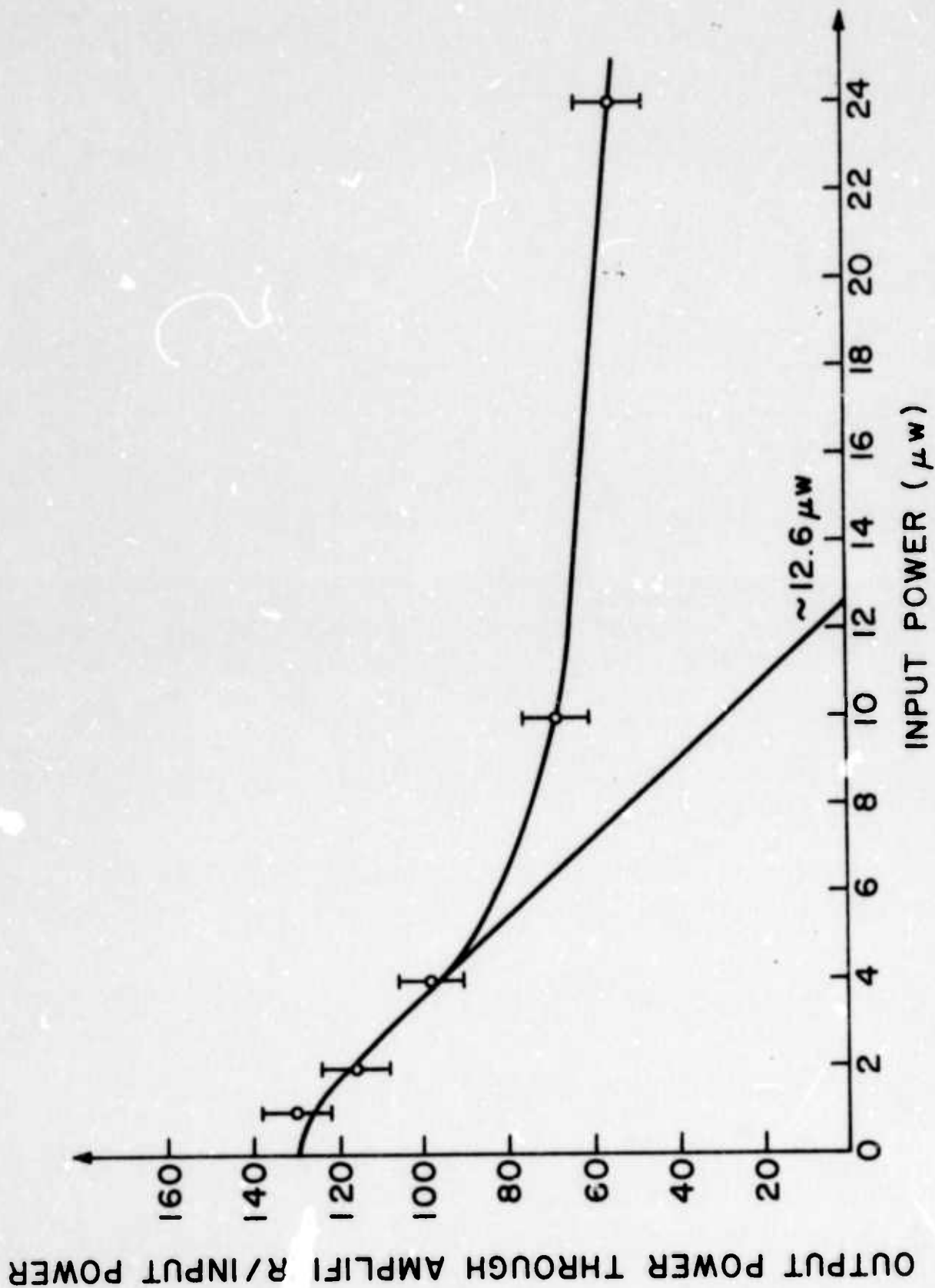


Fig. 6b - Transmission characteristics of He-Xe amplifier vs. input power

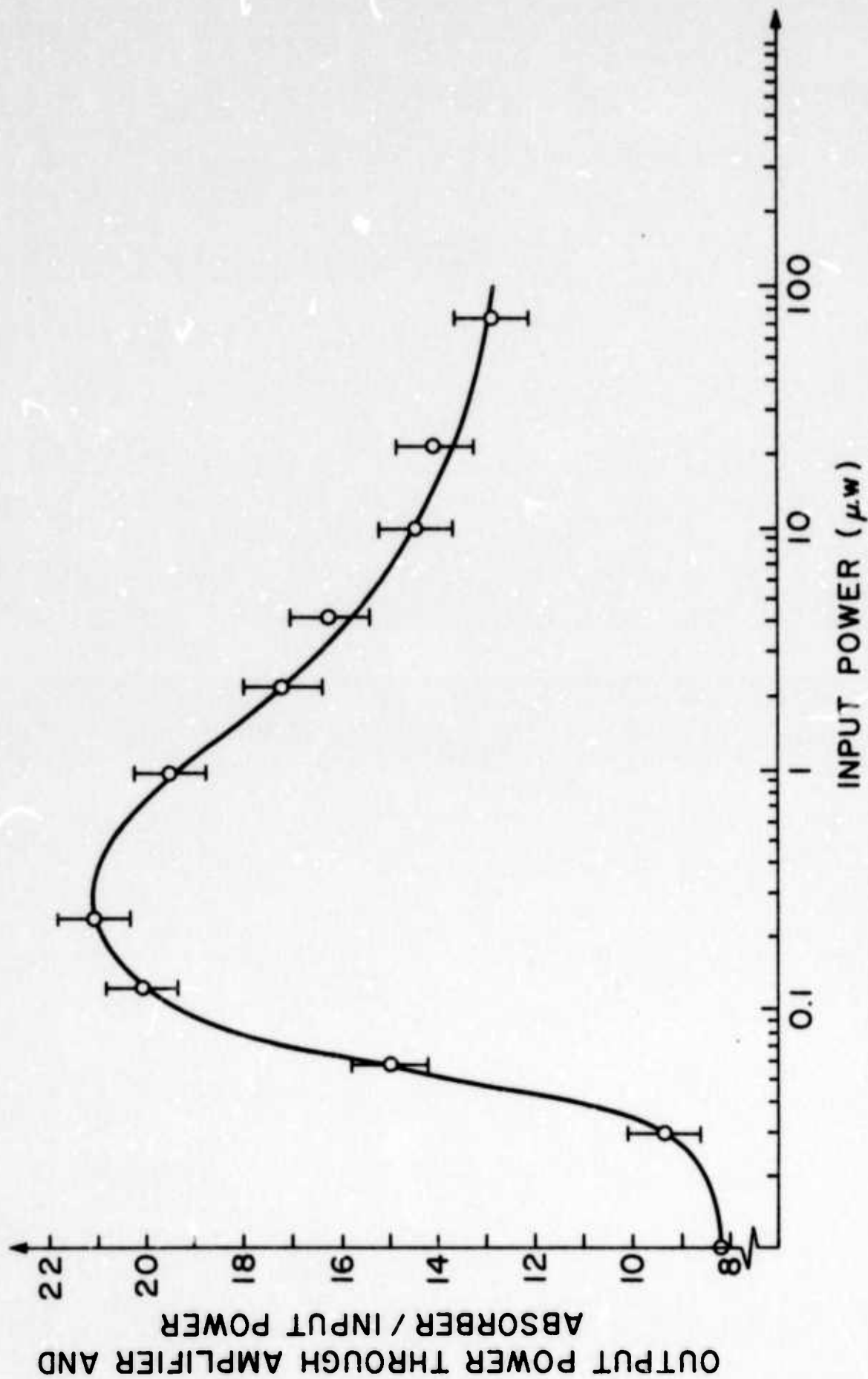


Fig. 7 - Transmission characteristics of the Xe-Xe BALAD system vs. input power

to the amplifier was increased, it was linearly amplified through the amplifier and the absorber was nonlinearly decreasing its absorption ability while it continued to be saturated. More transmission through the BALAD system would be expected. When the input signal to the amplifier reached the level of about 0.28 W, it started to saturate the amplifier. The amplification factor decreased while the absorber was almost at a constant attenuation. The transmission through the BALAD system decreased. As the input signal to the amplifier was further increased, the amplifier was saturated faster than the absorber as can be seen from Figs. 3a and 6a. The transmission continued to decrease as shown in Fig. 7.

In order to investigate the propagation of the beam through the BALAD system, one has to start from the equations which govern the propagation of Gaussian beam. The following discussion will presume "free space" propagation. The modifications due to radial variations in gain or absorption will be discussed in Appendix A. The evolution of short pulses will be discussed in Section 3 and Appendix B. For a given waist spot size ω_0 at $z=0$, the spot size ω and the radius of curvature of the beam, R , at a distance z are given by

$$\omega(z) = \omega_0 \sqrt{1 + (\lambda z / \pi \omega_0^2)^2} \quad (19)$$

$$R(z) = z [1 + (\pi \omega_0^2 / \lambda z)^2] \quad (20)$$

where λ is the wavelength of the beam. Solving Eqs. (19) and (20) for ω_0 and z in terms of $\omega(z)$ and $R(z)$, one gets

$$z = \frac{R}{1 + \left(\frac{\lambda R}{\pi \omega^2}\right)^2} \quad (21)$$

$$\omega_0 = \frac{\omega}{\sqrt{1 + \left(\frac{\pi \omega^2}{\lambda R}\right)^2}} \quad (22)$$

When a Gaussian beam with radius of curvature R_1 incidents on a concave mirror with focal length f . The radius of curvature R_2 of the reflected beam will be transformed according to the lens law

$$\frac{1}{R_2} = \frac{1}{R_1} - \frac{1}{f} \quad (23)$$

The radius of curvature of the beam from the 3.5 μ m He-Xe laser at mirror M_2 was about 285 cm and the spot size at M_2 was found to be $\omega_{M_2} = 3$ mm. From Eqs. (21), (22), and (23), the waist spot size ω_0 and its distance L_1 from M_2 is calculated to be

about 2.8 mm and 290 cm, respectively. The angular field of view of the amplifier for 1 mode is given by

$$\Omega_{\text{amp}}(1 \text{ mode}) = \frac{\lambda^2}{\pi \omega_0^2} = 0.5 \times 10^{-6} \text{ steradians} \quad (24)$$

The angular field of view of the amplifier in all modes is given by

$$\Omega_{\text{amp}}(\text{all modes}) = \frac{\pi(D/2)^2}{(L_1 - d_1)^2} = 0.24 \times 10^{-4} \text{ steradians} \quad (25)$$

where

$D_1 = 1 \text{ cm}$ is the diameter of the amplifier

$d_1 = 110 \text{ cm}$ is the distance from the mirror M_2 to the window of the amplifier.

The number of modes (or resolution elements) m of the amplifier is given by

$$m(\text{amplifier}) = \frac{\Omega_{\text{amp}}(\text{all modes})}{\Omega_{\text{amp}}(1 \text{ mode})} = 48 \quad (26)$$

By substituting $z = M_2M_3 + M_3M_4 - L_1 = 240 + 110 - 290 = 60 \text{ cm}$ into Eq. (19) and Eq. (20), one finds the spot size and radius of curvature of the beam at mirror M_4 to be $\omega_{M_4} = 2.8 \text{ mm}$ and $R = 8.6 \times 10^5 \text{ cm}$. Using Eqs. (21), (22), and (23), the waist spot size and its distance from M_4 is given by $\omega_0 = 0.17 \text{ mm}$, and $L_2 \approx 20.9 \text{ cm}$. The angular field of view of the absorber for 1 mode is given by

$$\Omega_{\text{abs}}(1 \text{ mode}) = \frac{\lambda^2}{\pi \omega_0^2} = 1.35 \times 10^{-4} \text{ steradians} \quad (27)$$

The angular field of view of the absorber in all modes is given by

$$\Omega_{\text{abs}}(\text{all modes}) = \frac{\pi(D_2/2)^2}{(L_2 - d_2)^2} = 1.97 \times 10^{-3} \text{ steradians} \quad (28)$$

where

$D_2 = 0.5 \text{ cm}$ is the diameter of the absorber

$d_2 = 10 \text{ cm}$ is the distance from M_4 to the window of the absorber.

The number of modes m of the absorber is

$$m(\text{absorber}) = \frac{\Omega_{\text{abs}}(\text{all modes})}{\Omega_{\text{abs}}(1 \text{ mode})} = 7 \quad (29)$$

The spot size at mirror M_5 is about $\omega_{M_5} = 1.3$ cm and the radius of curvature of the beam after reflecting from M_5 is about 26 cm. Similarly, from Eqs. (22) and (23), the waist spot size ω_0 and the distance is calculated to be 0.22×10^{-2} cm and 26 cm, respectively. The number of modes that the Ge-Au detector is able to receive is given by

$$m(\text{detector}) = \frac{\text{Area of detector}}{\pi \omega_0^2} = \frac{7.9 \times 10^{-3} \text{ cm}^2}{\pi \omega_0^2} \approx 500 \quad (30)$$

2.6 Conclusions of the Experimental Study

This completes the description of the experimental demonstration of the xenon-xenon BALAD system. The conclusions of this study are presented along with other results in Section 6.

3.0 THEORETICAL INVESTIGATION OF COHERENCE PULSE PROPAGATION AND SELF FOCUSING OF COHERENT PULSES

3.1 Introduction

When optical pulses propagate coherently through resonant media, dramatic differences in behavior from ordinary propagation occur. These effects depend on the resonant interaction of the polarizable medium with pulses short compared to the phase memory time. An example is the phenomenon of "Self-Induced Transparency."⁷ A review paper by G. L. Lamb, Jr.⁸ surveys the work in this area. Gibbs and Slusher^{9, 10} have obtained experimental verification of important aspects of coherent pulse propagation phenomena. In the published work, the emphasis has been on configurations without spatial variations in the directions transverse to the direction of propagation. Coherent propagation with transverse variation has been discussed by McCall and Hahn¹¹ using a generalization of one-dimensional "Pulse Area-Pulse Energy" theorems. Barone and Chi¹² have shown how the inclusion of transverse effects in the theory can lead to qualitative changes in the behavior of the predicted steady state pulses. In connection with studies involving an absorber driven by strong pulses, Rhodes and Szoke¹³ have noted effects which they attributed to transverse variations in the optical beam.

Transverse phenomena have, of course, been emphasized in the work dealing with self-focussing of optical pulses, but these usually have been concerned with the effects of non-resonant non-linearities. A review paper by S. A. Akhmanov, A. P. Sukhorukov, and R. V. Khokhlov contains a bibliography of work up to¹⁴ 1967. Self-focussing involving resonant interactions has been studied by A. Javan and P. L. Kelley¹⁵ and by D. Grischkowsky and J. A. Armstrong.¹⁶ Both of these investigations rely on the dispersive part of the susceptibility on the wings of the resonance line to provide the non-linear index of refraction. The response of the medium is describable in terms of a simple intensity dependent susceptibility, rather than a more general functional of the applied field. In the first paper, this was possible because the field is slowly varying in a relaxation time, and in the second because its variation in time is consistent with the approximations which lead to "adiabatic following."

When there is a susceptibility, the mathematical formulation of self-focussing can be made equivalent to the mechanical problem of particle motion in a potential well with friction; the shape of the well being determined by the form of the susceptibility. Thus, one can easily visualize the formation of self-focussing modes. In the more general case, this useful model is not available and greater reliance is had on numerical integration of the coupled field material equations.

J. A. Fleck, Jr. and C. Layne¹⁷ have included the effect of resonant interactions in their numerical study of self-focussing damage in a Nb-glass amplifier. Their formulation was capable of handling coherent effects since the resonant interaction was

described in terms of Bloch's equations. However, for the system of interest, these equations were solved in the rate equation approximation and hence did not include coherent effects.

We have been studying the propagation of short optical pulses through resonant media with emphasis on transverse effects associated with coherent interactions between the field and the material system. When the incident field has substantial transverse variation over the input aperture significant alterations of transverse structure are to be expected under certain conditions, even within the "near field" region of the effective input aperture. This expectation is based on the dependence of the velocity of a one-dimensional pulse on the pulse area and shape. The dominant feature of coherent pulse propagation in absorbers are the reshaping toward a steady state form and pulse speeds that are considerably less than the speed of light in the medium. In the three-dimensional problem, we would expect a region surrounding each ray to at first propagate like the corresponding one-dimensional input field of the same amplitude. However, after a certain distance longitudinal reshaping will lead different rays to carry pulses with different speeds. This, in turn, will lead to transverse reshaping. When this occurs, the radial derivatives in the wave equation can lead to significant transverse phase variations and energy flow. Because of the complexity of the coupled field-material system equations, we have used numerical integration to investigate these effects.

3.2 Field and Material System Equations

In our work, the electric field is assumed to be plane polarized transverse to the direction of propagation, z , and of the form

$$E = \delta e^{-i\theta} + \delta^* e^{i\theta} \quad , \quad (31)$$

with

$$\theta = \omega t - \omega n z / c \quad , \quad (32)$$

where n is the index of refraction associated with the non-resonant part of the material system and ω is the carrier frequency. The resonant part of the material polarization is taken to be of the form

$$P = -i\theta e^{-i\theta} + i\theta^* e^{i\theta} \quad . \quad (33)$$

Assuming that the complex amplitudes δ and θ vary slowly in their z and t dependence compared to the high frequency variations of the carrier, the wave equation in cylindrical coordinates simplifies to

$$\left[-i \frac{c}{2n\omega} \frac{\partial^2}{\partial r^2} + \frac{1}{r} \frac{\partial}{\partial r} + \frac{\partial}{\partial z} + \frac{n}{c} \frac{\partial}{\partial t} \right] \delta = \frac{2\pi\omega}{nc} \theta \quad . \quad (34)$$

This form of the wave equation has been used in discussions of self-focussing¹³ with the polarization amplitude \mathcal{E} expressed as a non-linear function of the field amplitude \mathcal{E} . For coherent interactions, the polarization amplitude is a functional of the field. In order to be capable of describing coherent effects, we model our material system by a gas of two level atoms. A general description of such a system would include the effects of degeneracy and inhomogeneous broadening. The polarization amplitude would be a sum over a degeneracy index j and an integral over an inhomogeneous line:

$$P = \sum_j N_j \int g(\Delta\omega) P_j(\Delta\omega) d\Delta\omega \quad (35)$$

where N_j is the number density corresponding to the degeneracy index j and $g(\Delta\omega)d(\Delta\omega)$ is the fraction of molecules in the interval $d\Delta\omega$ whose central resonant frequency differs from the inhomogeneous line center by the frequency interval $\Delta\omega$. Each polarization amplitude $P_j(\Delta\omega)$ satisfies the Bloch equations.⁸

$$\left(\frac{d}{dt} + \frac{1}{T_2} + i\Delta\omega\right)P_j = \frac{|\mu_j|^2}{\hbar} \mathcal{E} W_j \quad (36)$$

$$\left(\frac{d}{dt} + \frac{1}{T_1}\right)(W_j - W_j^0) = -\frac{2}{\hbar} (\mathcal{E} P_j^* + \mathcal{E}^* P_j) \quad (37)$$

In this section we will report on the study of transverse effects in non-degenerate homogeneous systems. In Eq. (35), the degeneracy index j , takes on only the value 1, and the line shape function $g(\Delta\omega)$ is a delta function, $g(\Delta\omega) = \delta(\Delta\omega)$. We have studied amplifiers and absorbers and cases where the input pulse duration is short as well as comparable to the relaxation times. When the pulse duration is comparable to and longer than the relaxation time, it is appropriate to describe the system in terms of a linear gain or loss coefficient a_0 in units of cm^{-1} . In our notation a_0 is given by:

$$a_0 = \frac{2\pi\omega}{nc} N W^0 \frac{|\mu|^2}{\hbar} T_2 \quad (38)$$

This quantity, the Fresnel number of the aperture (diameter $2\rho_0$) corresponding to the distance a_0^{-1} , $\rho_0^2/\lambda a_0^{-1}$, and the ratio of relaxation times T_1/T_2 provide three independent parameters to define the solution. We have chosen these parameters to be consistent with $\lambda = 10^{-4} \text{ cm}$, $a_0 = \pm(1/20 \text{ cm})$, $\rho_0 = 1 \text{ cm}$, $T_2 = 10^{-9} \text{ sec}$, $T_1/T_2 = 2$. The sign of a_0 depends on whether we are dealing with an attenuator or absorber.

When the pulse duration T_p , is short compared to the relaxation time T_2 , it is no longer appropriate to refer to the linear absorption length. In that case, we scale to T_p the quantities that were previously referred to T_2 , and take $T_p = 10^{-9} \text{ sec}$, $T_2/T_p \gg 1$. In the calculations reported on below, we use $T_2 = 10T_p$, and $T_2 = T_p$.

In this section, we will describe the results of our calculations of transverse effects associated with coherent propagation through absorbers. We will relate the results of our numerical analysis of propagation in 3 dimensions with corresponding calculations for the one-dimensional configuration. It will be seen that significant self-focussing can occur when coherent pulses propagate through a resonant absorbing medium. We differentiate between "transverse reshaping" and "self-focussing." The latter is associated with the transverse flow of energy. This "current" may be identified from the energy equation derivable from Eqs. (34)-(37).

$$\nabla \cdot \vec{J} = - \frac{\partial}{\partial t} \left[\frac{n^2 |\delta|^2}{2} + \frac{N\hbar\omega}{2} W \right] - \frac{N\hbar\omega}{2} \left(\frac{W - W_0}{T_1} \right), \quad (39)$$

where the radial and longitudinal components of the intensity vector J_ρ , and J_z are given by

$$J_\rho = \frac{c^2}{2\omega} i(\delta \nabla \delta^* - \delta^* \nabla \delta) \quad (40)$$

and

$$J_z = nc |\delta|^2. \quad (41)$$

In terms of the amplitude $|\delta|$ and phase, φ , of the complex amplitude:

$$\delta = |\delta| e^{i\varphi} \quad (42)$$

we have

$$J_\rho = \frac{c^2}{\omega} |\delta|^2 \frac{\partial \varphi}{\partial \rho}.$$

Thus transverse energy flow is associated with a radial variation of the phase of the complex amplitude δ .

3.3 Transverse Effects in Absorbers

3.3.1 One Dimension

In our discussion of absorbers, we first consider the case of one-dimensional pulse propagation with the pulse duration much shorter than both T_1 and T_2 . Analytic distortionless solutions of the material-field equations are known⁸ of the form

$$\frac{|\delta|}{\hbar} = \frac{2}{\tau_p} \operatorname{sech} \frac{[t - (z/v)]}{\tau_p} \quad (43)$$

where v is the pulse velocity given in terms of the pulse length τ_p by

$$\frac{1}{v} = \frac{n}{c} + \frac{a_0}{T_2} \tau_p^2. \quad (44)$$

This is the 2π pulse:

$$\int_{-\infty}^{\infty} dt \frac{|\mu| \delta}{h} = 2\pi \quad (45)$$

In Fig. 8, we present the results of numerical integration of the one-dimensional field equation for the case that the input pulse is a gaussian in time of input area 2π .

Figures 8(a) through 8(c) show the pulse reshaping. In this, and succeeding figures, the symbol τ stands for the time counted from the instant when a signal traveling at the speed of light in the medium reaches the point z , thus

$$\tau = t - \frac{n}{c} z \quad (46)$$

The units of τ are nanoseconds. After 300 cm the pulse shape closely matches the sech form. From the measured width after 300 cm the analytic expression for the pulse velocity is $(v/c) = 0.7$. In Fig. 8(d), we have plotted the integrated intensity ($\text{Energy}/\text{cm}^2 = \int d\tau |\delta|^2$), pulse area, and time delay of the peak all against the propagation distance z . The time delay is the difference between the final and initial values of τ at the peak of the pulse. This quantity measures the velocity of the peak relative to the speed of light.

$$\frac{v}{c} = \left[\frac{1}{c(\Delta\tau/\Delta z) + 1} \right] \quad (47)$$

where $\Delta\tau$ is the time delay accumulated in the interval Δz . We note that the pulse area remains at the input value 2π and the pulse energy decreases linearly with distance as the pulse reshapes from gaussian toward sech. This decrease is associated with the non-vanishing (but small) value of T_1^{-1} . The pulse peak moves more slowly than the speed of light. After 300 cm, the numerical pulse velocity is 0.7 times the speed of light. This corresponds to the speed of the sech pulse of the same width.

3.3.2 Three Dimensions

Figure 8 is to be contrasted with Fig. 9 which presents the results of numerical integration of the three-dimensional field equations for the same parameters. The input pulse has a gaussian variation with radius, ρ , as well as with time, τ , in the input plane $z = 0$. This is illustrated in Fig. 9(a) where the units of ρ are cm. In this figure, the dependence of the field amplitude $|\delta|$ on τ is shown for three values of ρ , $\rho = 0$, $5/14$ cm, and $5/7$ cm. Up to about 40 cm, the variation with τ along the axis $\rho = 0$ is the same as it was in the one-dimensional problem previously treated. After 50 cm, there is a strong departure from one-dimensional behavior. Figures 9(b) and 9(c) show the development of transverse reshaping and self-focussing. The pulse characteristics as a function of propagation distance z are summarized in Fig. 9(d). For the first 40 centimeters, the area and intensity along the axis $\rho = 0$ do not differ significantly from

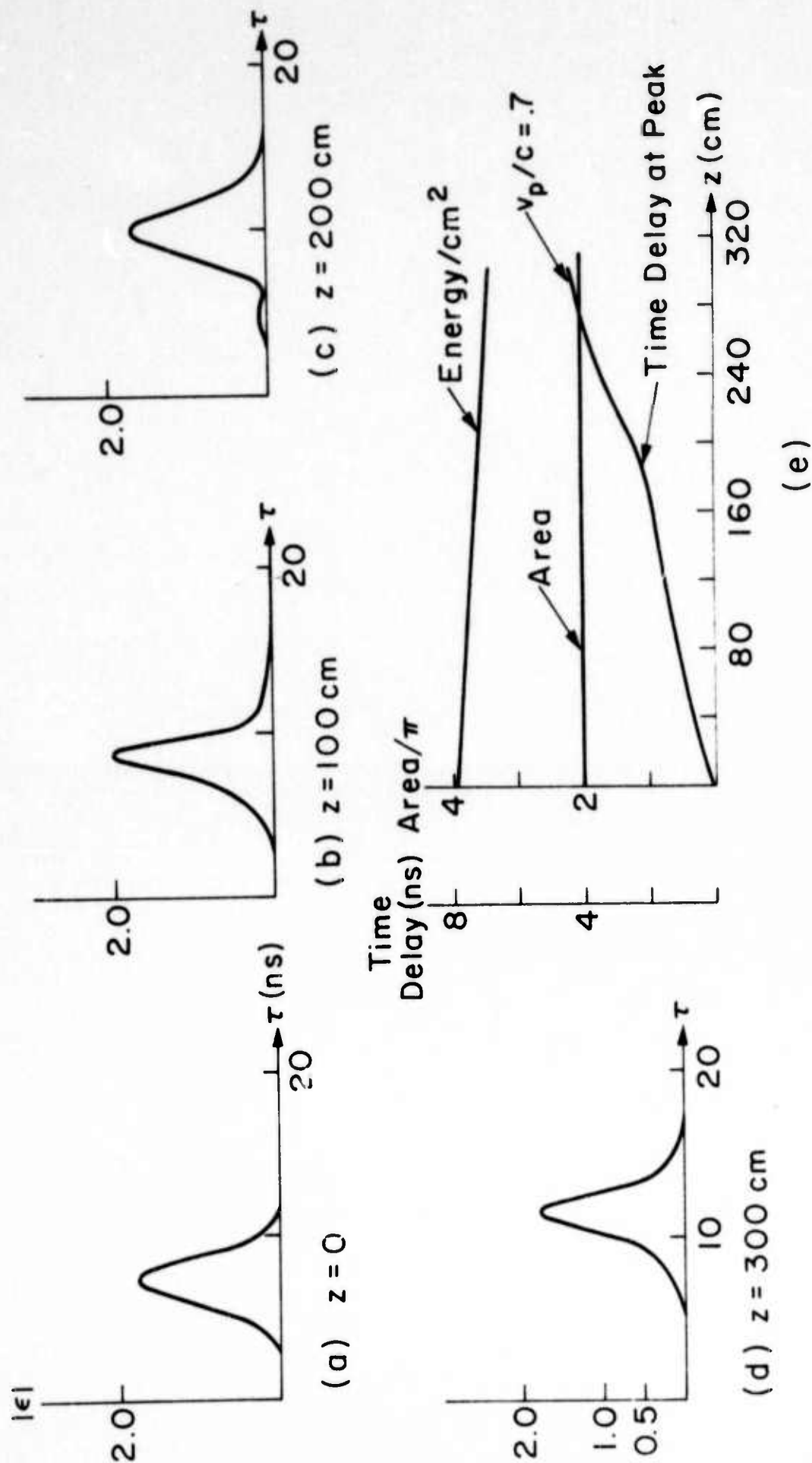


Fig. 8 - Absorber, one dimensional propagation. $T_1 = 2T_2 = 20T_p$ (T_p = pulse duration). Figures (a) to (d) illustrate the time behavior of a 2π input pulse at various planes. The retarded time τ is measured in nanoseconds. Figure (e) gives the integrated intensity (Energy/cm²) = $\int d\tau |\mathcal{E}|^2$, pulse area, and time delay at the peak all against the propagation distance z .

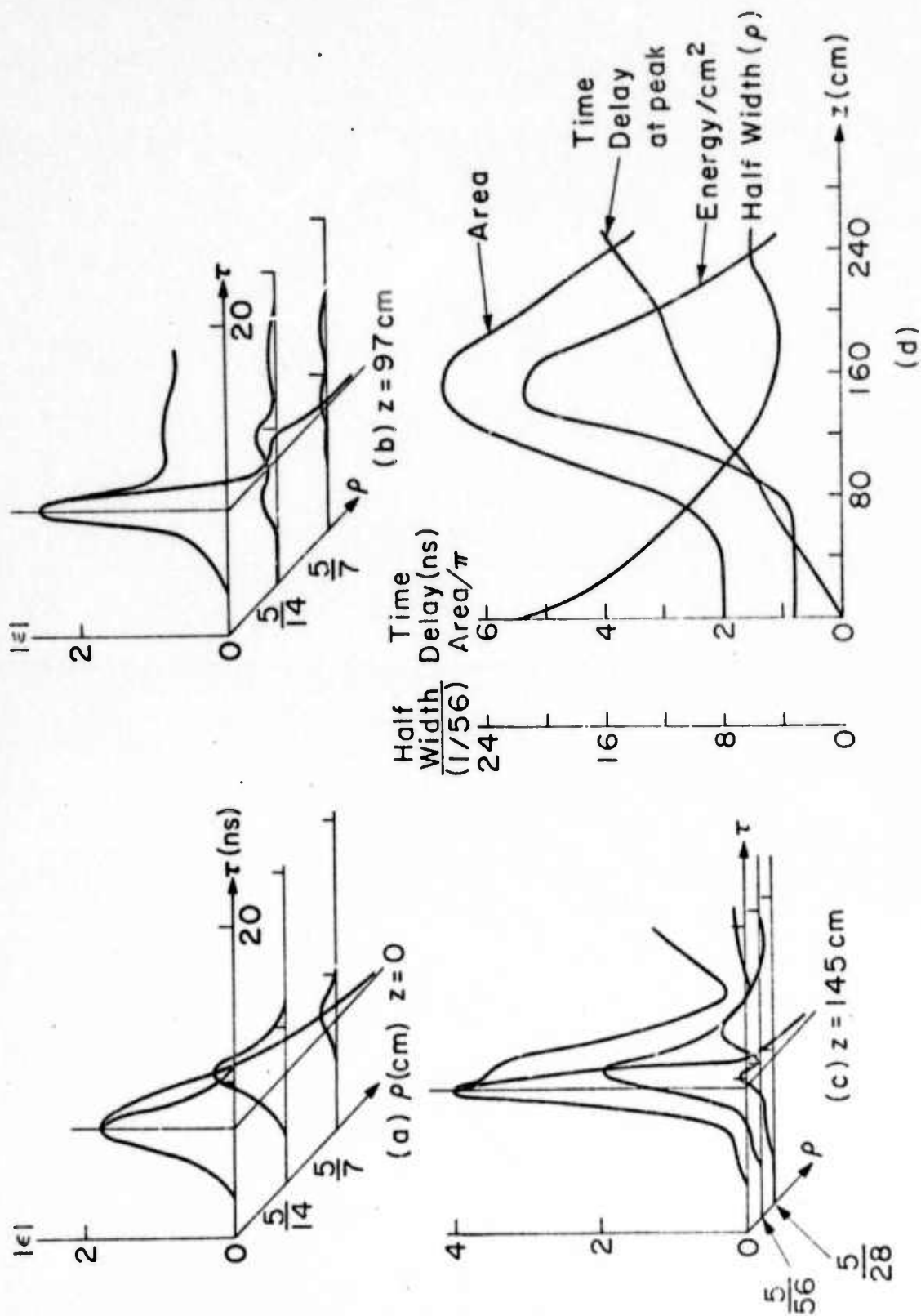


Fig. 9 - Absorber, three dimensions. $T_1 = 2T_2 = 20T_p$. Figures (a), (b), and (c) illustrate the transverse as well as temporal evaluation of an incident pulse of area 2π along the axis ($\rho = 0$). These describe the input plane, $z = 0$, a plane where self focussing has affected transverse behavior, $z = 97$ cm and the focal plane, $z = 145$ cm. Figure (d) gives the integrated intensity, pulse area, and time delay at $\rho = 0$ as a function of propagation distance.

their behavior in the one dimensional case. The half-width in the ρ dimension is decreasing, however, indicating transverse reshaping without transverse energy flow. When this reshaping process has reached a critical point there is a sudden increase in the area and energy density along the central axis. This shows that there must be substantial transverse energy flow. The energy density goes through a peak at 145 cm where it is seven times its input value. After this point, it starts to decay. This subsequent energy loss is not accomplished by a full expansion of the beam size. It is noteworthy that substantial ringing has occurred after the pulse peak -- although this effect was absent in the one-dimensional case. The energy density plotted in Fig. 9(d) is integrated up to 20 nanoseconds from $\tau = 0$, and thus is an underestimate. The existence of transverse energy flow is clearly illustrated in Fig. 10 which gives the amplitude and phase of the complex field amplitude as a function of ρ after two propagation distances, $z = 97$ cm and $z = 145$ cm. For each propagation distance the field amplitude and phase are examined for two values of τ , one at the peak of the pulse and the other shortly after. A downward curvature to the phase as a function of ρ corresponds to a focussing field. At the 97 cm distance, the phase variation is considerably stronger after the peak than on the peak. Had the remaining propagation been in free space, the cut through the peak would have focused after 675 cm whereas the cut after the peak would have focused after only 107 cm. The actual focus occurred after 40 cm.

The self-focussing effects just described disappear when the transverse relaxation time is shortened to equal the pulse duration, keeping other parameters constant. When the pulse is short compared to the transverse relaxation time and the carrier frequency is sufficiently offset with respect to the central resonance frequency opposite signs of the curvature of the phase as a function of ρ develop on either side of the resonance, consistent with the results of Grischowsky and Armstrong.¹⁶

3.4 Summary

We have studied the temporal and transverse spatial evolution of optical pulses in resonant media. Numerical integration of the coupled field-material system equations shows the phenomena of transverse reshaping and self-focussing. Self-focussing is associated with transverse energy flow. This effect is specific to coherent interactions between the pulse and resonant medium, and disappears when the pulse duration is comparable to, or longer than, the transverse relaxation time. The effect is distinct from self-focussing due to adiabatic following since it occurs when the carrier frequency is at line center.

The implications of this study for the BALAD receiver are discussed in Section 4.

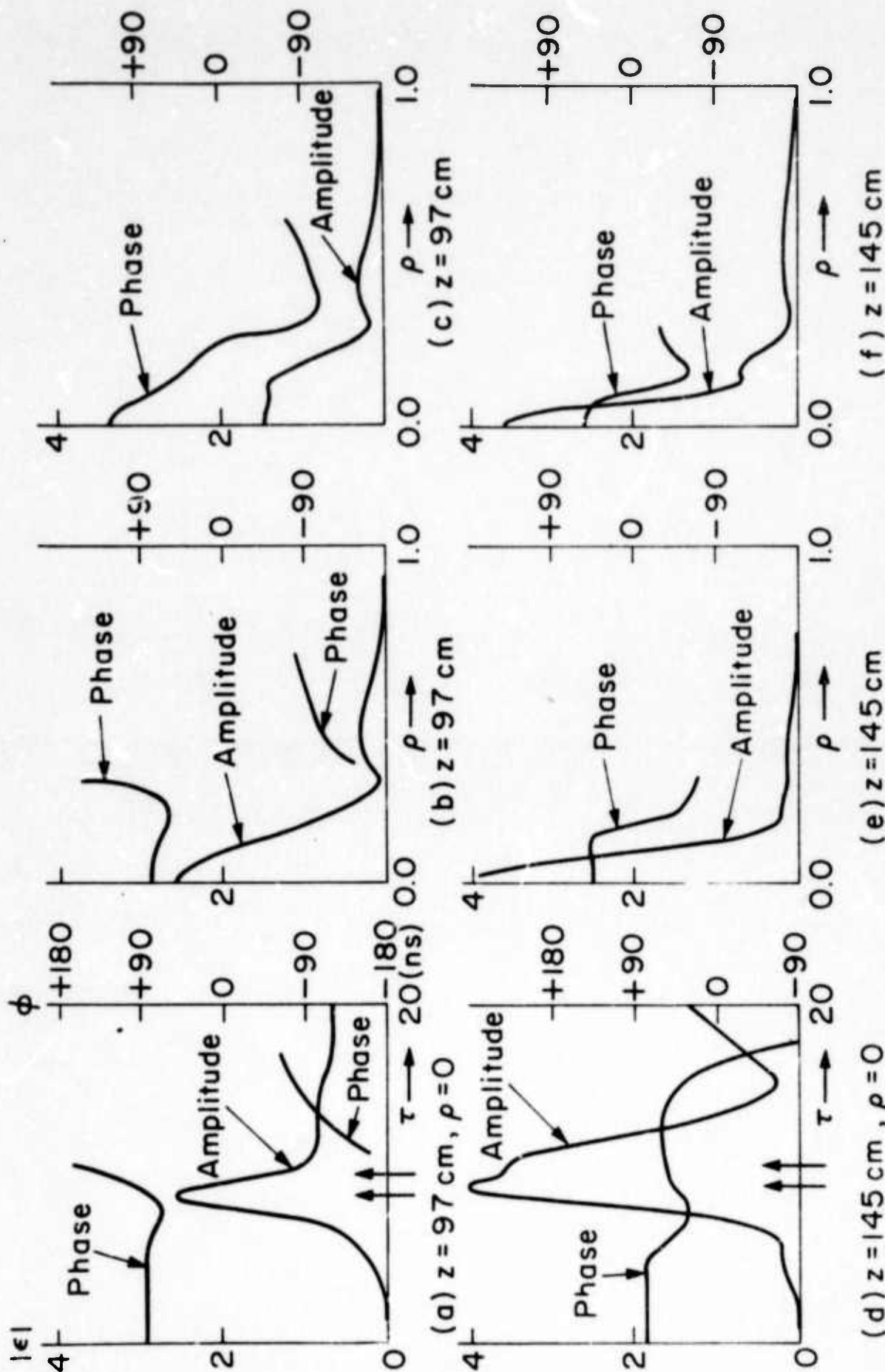


Fig. 10 - Absorber, three dimension, $T_1 = 2T_2 = 20T_p$. Figures (a) and (d) represent the temporal behavior of the amplitude $|\epsilon|$ and phase ϕ of the field at the 97 cm and 145 cm planes, respectively. Figures (b) and (c) give the radial dependence of the amplitude and phase at the times when the respective pulses have passed through their peaks (first arrow). Figures (e) and (f) give the radial behavior 1.5 nanoseconds after peak (second arrow). A downward curvature to the phase as a function of ρ indicates focussing.

4.0 POSSIBLE IMPROVEMENTS IN THE BALAD RECEIVER SYSTEM

4.1 Comments on Alternative BALAD Geometries

A previous report¹ discussed alternative geometries for a BALAD receiver system. The basic features of the BALAD receiver are shown in Fig. 11(a), and a rather impractical multistage absorber alternative is shown in Fig. 11(b). The alternatives which were studied in particular, were the optical waveguide configuration and the Fly's Eye lens train configuration shown in Figs. 12 and 13. In both of these cases, the use of a waveguiding structure in the saturable absorber allows the use of a much shorter focal length lens (i.e., a smaller f/number lens) at the input to the saturable absorber. Because of this, the signal beam cross-section is much smaller and the signal beam intensity is correspondingly larger than would otherwise be the case. As a result, substantial improvements were predicted in the performance of a BALAD system employing these alternatives.

The present contract concentrated on the demonstration of a Xe-Xe BALAD system. The saturable absorber for this system is a gaseous discharge. Because of the difficulty in obtaining quiet operating conditions in the xenon absorber discharge, it is apparent that the optical waveguide geometry would not be appropriate for the Xe-Xe BALAD receiver system. It would be difficult, if not impossible, to run a discharge in a single long small diameter capillary tube of the type which would form the optical waveguides. Based on our present experience, such a discharge (in xenon) would surely be noisy. Finally, the array of waveguides, which would require running many such discharges in parallel, would present an impossible task.

A passive absorber, such as the SF_6 employed in the CO_2 - SF_6 BALAD system, is clearly compatible with the "array of waveguides" geometry. However, with such a system, one would be tempted to provide a matching array of waveguide amplifiers to precede the waveguide absorber, to take advantage of the larger gains achievable in CO_2 waveguide lasers.¹⁸ If so, the difficulty of running parallel discharges would have to be faced.

The Fly's eye lens train geometry would appear to be compatible with a xenon discharge absorber. The generally observed $1/d$ dependence of the absorption coefficient of the Xenon absorber must be recognized in the design of such a system. This tends to restrict the absorber aperture. Finally, the task of producing arrays of Fly's eye lenses using infra-red transmitting materials is non-trivial.

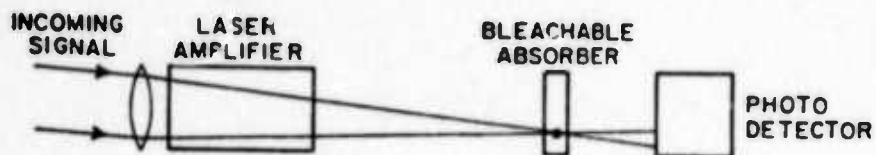


Fig. 11(a) - BALAD receiver. Absorber becomes transparent at the focus and frequency of the signal beam.

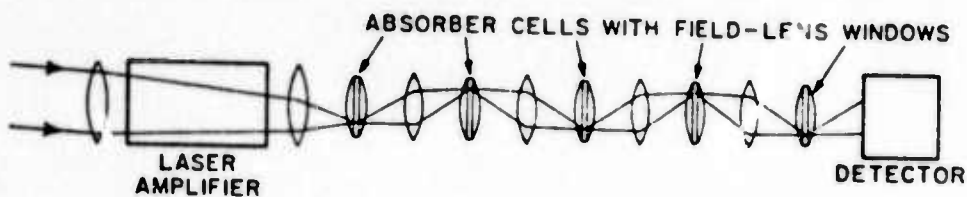


Fig. 11(b) - BALAD receiver with fine-focus multi-stage absorber required for gas with low attenuation and high saturation intensity.

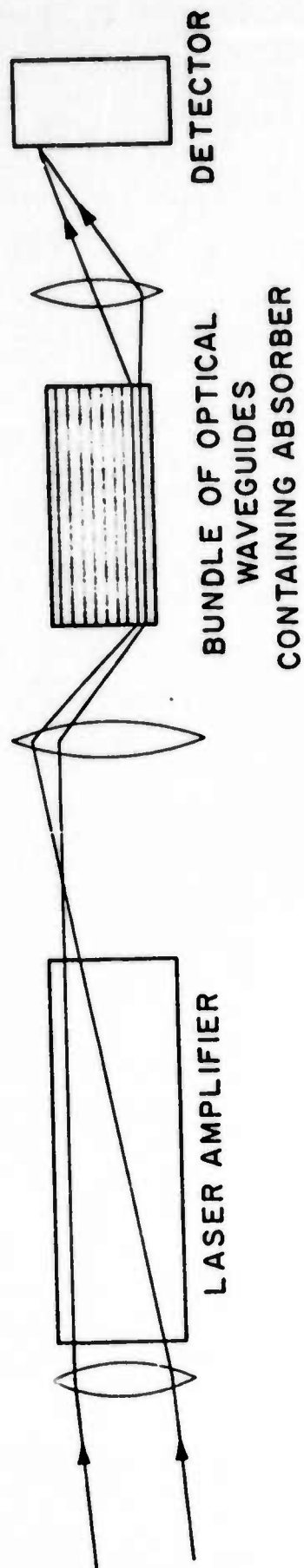


Fig. 12 - Alternative BALAD arrangement to that of Fig. 11.
Periodic refocussing through absorber is unnecessary
if light is confined in a waveguide.

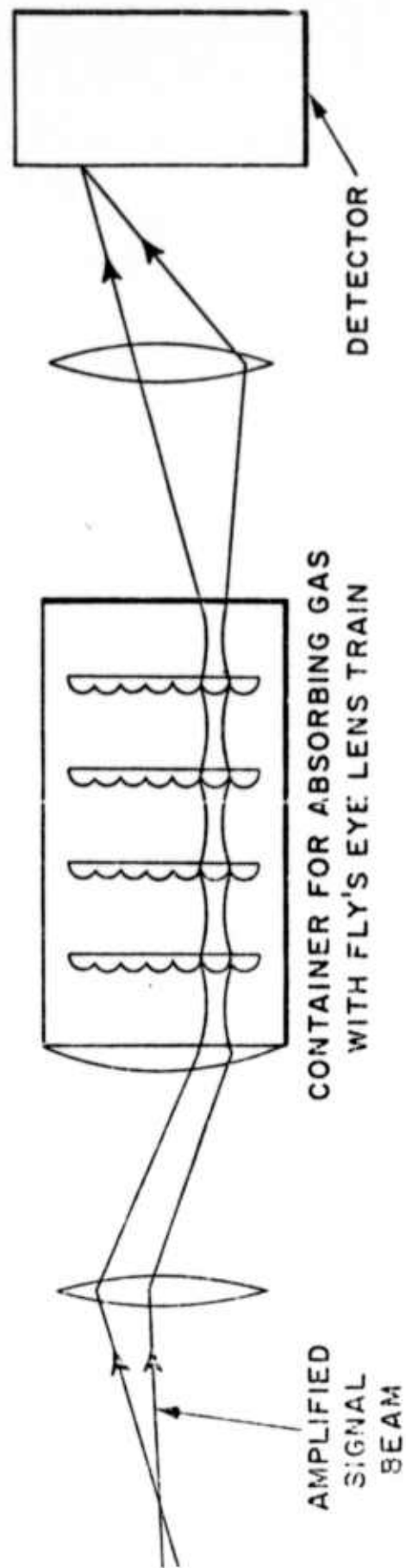


Fig. 13 - Alternative BALAD arrangement to Fig. 11(b). Fly's Eye lens train configuration. Focused signal beam is confined in absorber by series of lenslets in a molded fly's eye lens train. Each lenslet corresponds to a resolution element of the field-of-view.

4.2 The Application of Non-linear Self-focussing to a Geometrical Loss Filter

As discussed in Section 3, the analysis of the propagation of a coherent optical pulse in a resonant absorber revealed a strong self-focussing effect. In other words, the presence of the optical pulse locally modified the focussing properties of the absorber. The effect was strong enough to focus the optical pulse into small spot when otherwise it would have been diverging.

If the diameter of the optical beam at the input to the saturable absorber is reduced, then it should be possible to find a beam diameter for which the focussing effect is just balanced by the spreading due to diffraction. If so, then the non-linear self-focussing effect would guide the optical pulse with a constant diameter. If such is the case, then the design of a geometrical filter for improving the performance of the BALAD receiver is straightforward. In essence, the non-linear self-focussing effect would provide an automatically aligned optical waveguide which exists only for the signal beam and not for the background noise.

Further work is required to completely analyze the behavior of such non-linear self-focussing and to experimentally test the propagation of optical pulses in saturable absorbers. The purpose of the following discussion is to anticipate what can be done if that work were successfully completed. Thus, the discussion may be useful in justifying support for such further work.

4.3 Design of a Geometrical Loss Filter Using Non-linear Self-focussing

The essential features of a geometrical loss filter using non-linear self-focussing can be developed from the BALAD arrangement shown in Fig. 14.

First, a few general comments about the overall optical system are in order. For simplicity of analysis, the figure is drawn with the distances $L_1 = L_2 = L_3$, and the lens apertures $D_1 = D_2 = D_3 = D_4$. More generally, the receiving aperture D_1 would be larger than the laser amplifier aperture which determines D_2 and D_3 . Also, the length L_3 would be adjusted in order for the beam size at lens No. 4 to match that beam diameter which results in self-focused waveguiding in the saturable absorber.

It is clear from Fig. 14 that the desired performance of the indicated optical system is as follows: a signal beam, incoming from a direction θ_1 is focused to a (diffraction limited) spot at lens No. 2, displaced a distance $X_2 = L_2 \theta_1$ from the optical axis. Thus, the linear field of view of the receiver is given by $\Delta\theta_1 = D_2/L_1$. If lens No. 2 images aperture D_1 on aperture D_3 , then all rays which pass through D_1 (within the field of view) will also pass through D_3 . The spot on lens No. 2 is imaged by lens No. 3 at lens No. 4 where it is displaced by $X_4 = (L_3/L_2)X_2$ from the optical axis. Finally, lens No. 4 renders the central ray, of the bundle of rays within the signal beam, parallel to the optical axis. Thus the central ray would still be displaced by

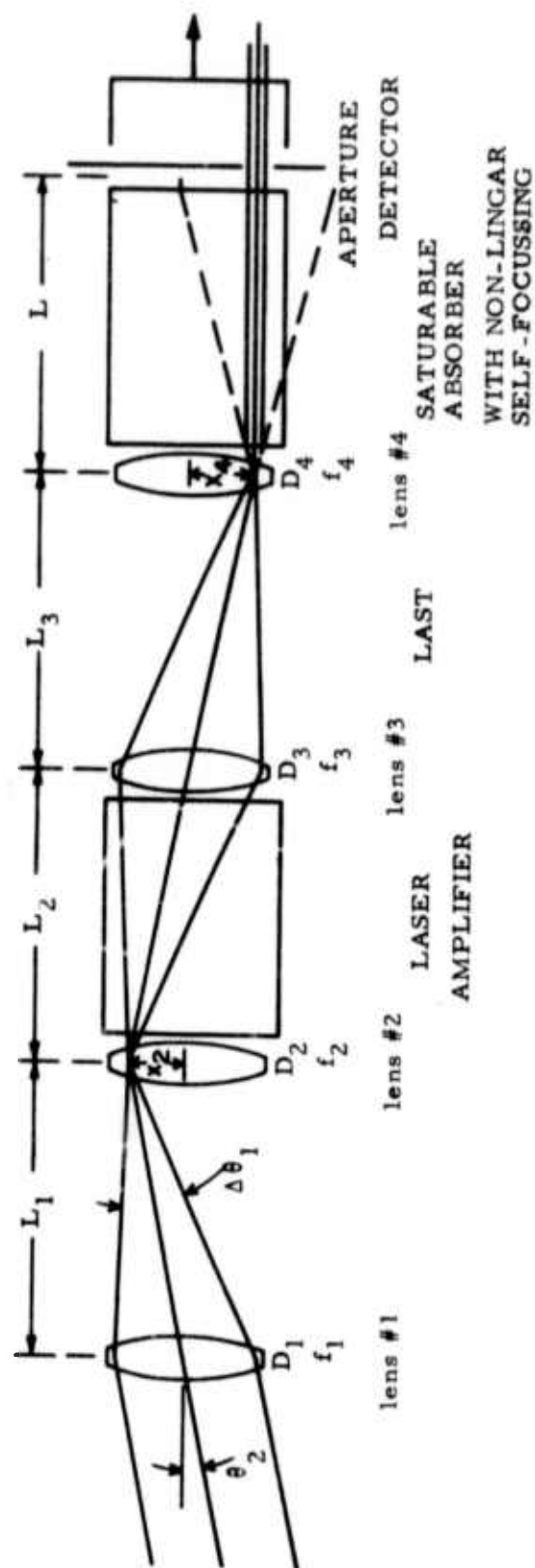


Fig. 14 · The BALAD receiver with a self-focussing saturable absorber

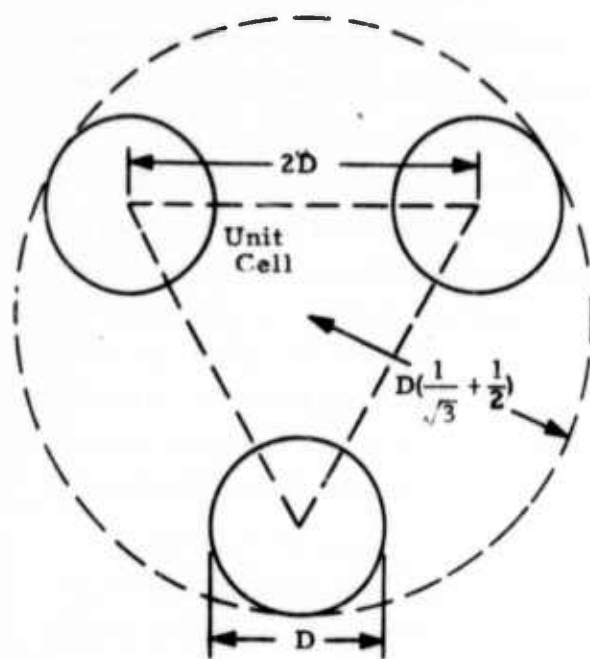
X_4 at the output of the saturable absorber. The desired focal lengths of the various lenses are determined by: $f_1 = L_1$; $1/f_2 = 1/L_1 + 1/L_2$; $1/f_3 = 1/L_2 + 1/L_3$ and $f_4 = L_3$. Also, the (useful lens apertures are given by: $D_1 = L_1/L_2 \cdot D_3$, $D_4 = L_3/L_2 \cdot D_2$. Note that the optical arrangement in Fig. 4 shows the signal beam diverging in the laser amplifier so that at the amplifier output, the signal beam has expanded out to fill the full laser amplifier aperture. If the signal beam diameter at the amplifier input is d , then if the amplifier gain $e^{aL_2} > (D_3/d)^2$, this arrangement minimizes saturation of the laser amplifier while maintaining the maximum field of view allowed by the laser amplifier aspect ratio.

As mentioned previously, the purpose of lens No. 4 is to render the central ray of the signal beam parallel to the optical axis. This is accomplished by the requirement $f_4 = L_3$. Beyond lens No. 4, in the absence of waveguiding, the signal beam would form a diverging wavefront as shown with dotted lines. The angle of this cone of diverging rays would be the same as the bundle incident on lens No. 4, which is D_3/L_3 or $(L_2/L_3) \cdot (D_1/L_1)$. On the other hand, if the non-linear self-focussing of the saturable absorber produces waveguiding, the signal beam would be confined to the narrow bundle of rays outlined by the solid lines in Fig. 14.

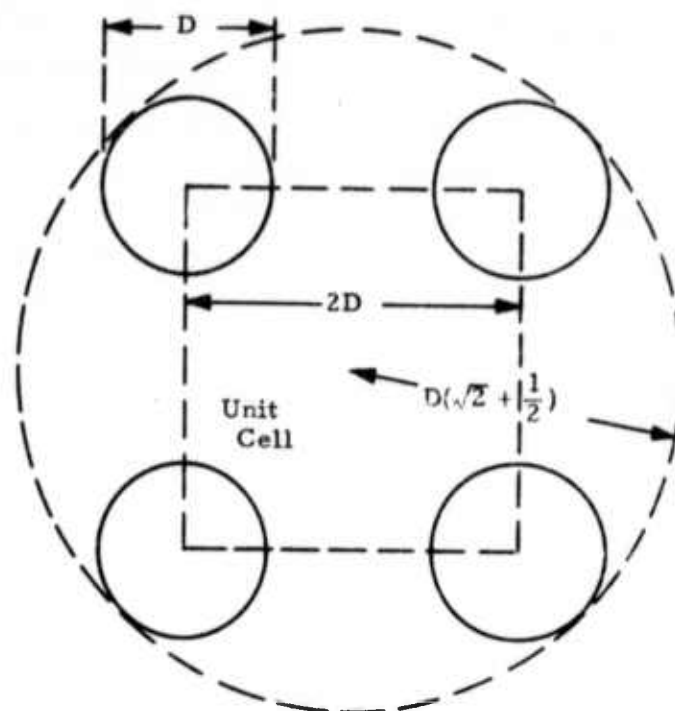
Now the evolution of the geometrical loss filter begins. If there were an aperture at the output of the saturable absorber, and if this aperture were properly positioned and its diameter matched the signal beam diameter, then in the second case above, (non-linear self-focussing) the entire signal beam would pass through the aperture to the detector. Whereas, in the absence of non-linear self-focussing, only a small fraction of the signal beam would pass through and be detected. The fraction of the total power received in the absence of self-focussing, would in fact, be given by $1/(\text{number of resolution elements in the BALAD receiver field of view})$. That is, such a (hypothetical) filter would, in fact, introduce an attenuation due to geometrical loss for any signal (or noise) which is precisely that factor which is desired in order to optimize the performance of the BALAD receiver. (See Ref. 19).

Now, of course, so far the filter is hypothetical, since it requires the automatic positioning of an iris or diaphragm to follow the signal beam. The means for achieving this result is to introduce a matched array of apertures at the input as well as at the output and at selected locations down the length of the saturable absorber. The geometrical considerations for such a "geometrical filter" are illustrated in Fig. 15.

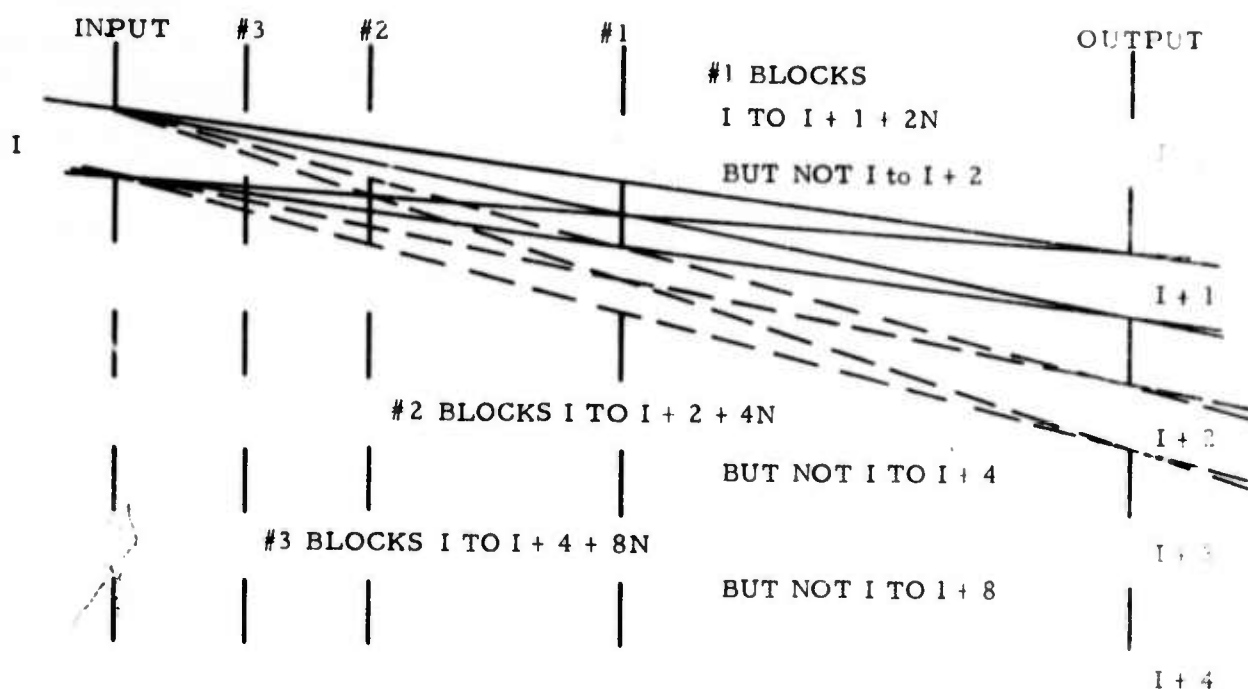
Consider, for example, a close packed array of circular apertures with centers separated by twice the diameter of the apertures. The "unit cell" of such an array is an equilateral triangle with a circle centered at each apex; the radius of the circle is one fourth of the side of the triangle. The average transmission of such an array (the fraction of the area which is open) is $T = \pi/8\sqrt{3} = 0.226$. A rectangular array with the



a) CLOSE PACKED



b) RECTANGULAR



c) PLACEMENT OF APERTURE ARRAYS

Fig. 15 - Aspects of geometrical filters

same nearest separation would have $T = \pi/16 = .196$. Either type of array has an acceptably large transmission for the use contemplated here.

If a pair of such arrays were closely spaced and perfectly aligned, the pair would have the same transmission as a single array. Since the transmission of a succession of optical elements in series is equal to the product of the individual transmissions, we would conclude that the transmission of the second array is unity ($T_1 \cdot T_2 = T_1$ implies $T_2 = 1$) when it immediately follows the first and is perfectly aligned. Conversely, if the second array were laterally displaced by an aperture diameter in any direction, the transmission of the pair of arrays would be zero. From this we conclude, that the transmission of the second filter is zero if it immediately follows the first and is perfectly misaligned ($T_1 \cdot T_2 = 0$ and $T_1 = 0 \rightarrow T_2 = 0$).

Now, if the pair of arrays were separated longitudinally, it is clear that the transmission of the pair of arrays would depend strongly on the direction of the incident light. Collimated light incident normally (if the two are perfectly aligned) would exhibit nearly the same transmission, reduced only by the diffraction spreading between the two arrays. Clearly, collimated light travelling at an angle θ from the normal, would be (nearly) perfectly blocked if $\tan \theta = D/L$ where D is the aperture diameter and L is the separation between the two arrays. Again, diffraction spreading of the light would produce some transmission.

But then, collimated light travelling at about twice that angle ($\tan \theta_2 = 2D/L$) would again be perfectly transmitted by the second filter -- if the azimuthal direction of the light path produces an overlap with a neighboring aperture. So, one is forced to introduce at least a third array of apertures to discriminate against those off axis light rays.

Before proceeding to investigate the minimum number and optimum placement of such arrays of apertures or "masks," let us consider the behavior of the proposed improved BALAD system making use of non-linear self-focussing in a saturable absorber.

First, we insist that an input signal beam, whatever its incident direction (or lateral displacement at the input to the saturable absorber) be transmitted by the filter. Thus, the signal beam diameter must be large enough so that at least one aperture is illuminated by (nearly) the full intensity of the signal beam. The worst case, of course, is to have the signal beam precisely centered between apertures -- at the center of a "unit cell" of the aperture array. In this case, 3 (or 4) apertures would be illuminated, but the fraction of the incident power falling on one aperture would be $1/(3.3)^2 \doteq 1/11$ for the close packed array or $1/(3.83)^2 \doteq 1/14.6$ for the rectangular array. This loss of signal power can be compensated by increasing the laser amplifier gain. An additional consideration is the resulting intensity distribution. Clearly, the beam transmitted

by an aperture would not be a gaussian. It would be closely approximated by a uniform cylindrical beam which is sharply truncated at the radius of the aperture. The behavior of such a beam within the saturable absorber would have to be investigated. More precisely, it will be necessary to investigate the performance of an "aperture waveguide" which is formed by the sequence of aligned apertures down the length of the absorber.

It is clear that in the absence of self-focussing, there is a "bundle of rays" in the signal beam so that precise alignment of the axis of the aperture array with optical axis would be unnecessary. There will be some ray within the bundle which would propagate down the axis of the array sequence. However, the non-linear self-focussing will presumably confine the beam, and cause it to propagate as a constant diameter beam in the direction determined by the incident direction. Thus it will be necessary to carefully align the sequence of apertures so that it is parallel to the optical axis, and the effect of this misalignment should be investigated theoretically.

One method of distributing the arrays of apertures down the length is to use a geometric progression. If there are a total of N^2 apertures, so that there are N apertures along a line drawn in an array, then we can number these sequentially as $I = 1, 2, 3, \dots, N$. The problem is to block the path from any aperture (I) in the first array to any other aperture ($I+J$) in the final array. The first additional array, if placed midway (at $L/2$) will block paths from I to $I + (1 + 2M)$ for all integer values of M , but the paths from I to $I + 2M$ would be open. The second additional array placed at $L/4$ (or $3L/4$) will block half of these, leaving paths from I to $I + 4M$ open. The third, at $L/8$ (or $7L/8$) will block half of these leaving paths from I to $I + 8M$ open. The K^{th} additional array, placed at a distance of $L/2^K$ away from any of the previous arrays, will leave open only those paths from I to $I + (2^K M)$. Clearly, when $2^K > N$, all paths except $I=I$ will be blocked. Thus for this method of placement, one needs $(2 + \log_2 N)$ masks, including the mask at the input and output of the saturable absorber.

For example, 5 masks are required for $N=8$; 6 masks for $N=16$, and 7 masks for $N=32$ (which would be a 1024 element array). Thus, the number of masks required is not excessive, and the minimum spacing between two masks is L/N which is also reasonable.

Finally, it can be mentioned that the construction of such arrays of apertures is much simpler and less exacting than the construction of an array of "fly's eye lenses" (or an array of waveguides). Fewer masks should be required, and the problem of mounting and alignment is certainly no more severe than the corresponding problems for the lenses.

4.4 The Geometrical Loss Filter - A Universal Attenuator

The fact that the geometric loss filter is universal is also notable. That is, it will attenuate any and all incident signals and noise, except that signal for which the saturable absorber exhibits non-linear self-focussing.

The absorption of the saturable absorber will contribute additional attenuation for signals which coincide in frequency. However, one major point of the geometrical loss filter with non-linear self-focussing is that it should operate and produce adequate attenuation with a length of absorber which is much shorter than that which would be required if one was relying on attenuation alone. That is, the absorption of the saturable absorber will probably be small compared to the geometric loss.

The geometrical loss of the filter can easily be calculated from Fig. 14. Let us recall that each aperture of the array represents, optically, a resolution element of the BALAD receiver, and that the total area of the array represents the field of view of the receiver. From Fig. 14, the bundle of rays incident on an aperture at the input to the absorber cell will have the (linear) divergence angle D_3/L_3 , thus at the end of the cell it will spread out to illuminate an area $(D_3 \cdot L/L_3)^2 \cdot \pi/4$ at the detector. Since the total area is $(\pi/4)D_4^2 = N^2 \cdot (\text{unit cell area})$, and only rays within one aperture at the output will reach the detector, the transmission of the filter will be:

$$\frac{(\text{area of one aperture})}{(\text{illuminated area})} = \left(\frac{T \cdot \text{cell area}}{\text{TOT area}} \right) \times \left(\frac{\text{TOT area}}{\text{illum. area}} \right) = \left(\frac{T}{N^2} \right) \left(\frac{D_4 L_3^2}{D_3 L} \right)$$

where T is the average transmission of one array, i.e., area of aperture/area of a unit cell. In the simplified geometry of Fig. 14, the latter factor is unity, and the attenuation is T/N^2 . Now noise uniformly illuminates the first mask (at the input), so that noise is attenuated by an additional factor of T .

In comparison, a signal, when present, will be focused to a spot whose size is by design somewhat larger than the area of one unit cell. So the signal passes entirely through one aperture (3 or 4 apertures) and suffers an attenuation of T_s at the input. But due to the non-linear self-focussing, it should suffer only minimal loss thereafter. Thus, the signal-to-noise ratio would be improved by the factor:

$$\frac{(S/N)_{\text{out}}}{(S/N)_{\text{in}}} = \frac{N^2 \cdot T_s}{T_s \cdot \frac{B_s}{\text{TOT}} + T^2 \left(\frac{D_4 L_3^2}{D_3 L} \right)} \quad (48)$$

where the added term in the denominator is due to that noise which is spatially (and spectrally) coherent with the signal which will "benefit" from the non-linear self-focussing of the signal, and only be attenuated by the signal factor T_s . The coherent

noise represents $1/N^2 \times (B_s)/(B_{TOT})$ of the total noise power, where B_s = bandwidth of the signal and B_{TOT} = total noise bandwidth which is determined by the laser pre-amplifier.

Compared to the theoretical ideal signal-to-noise ratio ($S/N = P/h\nu B_s$), the signal-to-noise ratio would be:

$$\frac{(S/N)_{out}}{(S/N)_{ideal}} = \frac{1}{1 + \frac{T^2}{T_s} \left(\frac{B_{TOT}}{B_s} \right) \left(\frac{D_4 L_3}{D_3 L} \right)^2} \quad (49)$$

For a molecular gas laser amplifier such as CO_2 or even for an atomic laser amplifier such as xenon, there are a multitude of transitions which exhibit gain and thus B_{TOT}/B_s can be large, which will degrade the signal-to-noise ratio. However, the output of the geometrical loss filter, which is collimated, is easily adapted to the insertion of a Fabry-Perot etalon which can easily filter out all but the "working" laser line. In such a case, B_{TOT} = Bandwidth of laser lines which are transmitted by the etalon.

Note that in this case we have not been concerned with the overlap of the absorber with all laser lines (although the absorption would always help). The added term in the denominator of Eq. (49) is the penalty for having the multitude of apertures.

In contrast, in the "standard" BALAD arrangement, where the absorber must do all of the attenuation, the existence of a non-overlapped laser line is disastrous -- the corresponding expression for this case is

$$S/N = \frac{1}{1 + N^2 \cdot \frac{B_{TOT}}{B_s}} \quad (50)$$

which is worse by the factor N^2 , but in this case, of course, B_{TOT} would only be the sum of lines which do not overlap the absorber. Moreover, the problem of filtering is more severe, since the noise input (and output from the absorber cell) is not collimated.

Thus, in addition to its other attractive features, the geometrical loss filter would solve the problem of filtering out radiation from all but the working line in the $10.6\mu CO_2$ laser amplifier and in amplifiers in the 3-5 μ spectral range.

5.0 SYSTEM HAZARD ANALYSIS

The directly applicable section of MIL-STD-882 is paragraph 5.8.2.1, Preliminary Hazard Analysis. According to this paragraph, a preliminary hazard analysis shall be performed as the initial analysis task during the acquisition of a system. This analysis shall be a comprehensive qualitative study. Such information shall be used in the development of safety criteria to be imposed in performance or design specifications. The most relevant areas of those listed to be considered are: (f) Effect of transient current, electro-static discharges, electromagnetic radiation, and ionizing radiation to or by the system. Design of critical controls to prevent inadvertent activation and employment of electrical interlocks, and (g) Use of pressure vessels and associated plumbing, fittings, mountings, and hold-down devices. In addition, for related applications, items (h), (i), (j), (n), (o), (p), (q), (s), and (t) should be considered.

The device under development is a coherent laser receiver. Under normal proper operation of the device, there is no optical output whatsoever. It is conceivable that if improperly used, the laser preamplifier could be made to oscillate. In the present system, it would almost require a deliberate act to set up oscillation conditions. But as a general rule, the alignment of optical windows or other partial reflectors normal to the optical beam axis should be avoided. A surface from which such unwanted reflection might occur is the optical detector, so the surface of the detector and any associated filters should be deliberately misaligned to avoid the possibility of feedback. The BALAD receiver is particularly protected from such reflections, since the gaseous bleachable absorber would strongly attenuate the reflected beam unless the frequency of the detected signal happens to coincide with the saturable absorber line center.

Thus, the hazard of eye damage would be practically non-existent in the operation of the BALAD receiver. In contrast, this could be a serious problem at the site of the associated laser transmitter.

The BALAD receiver system, as currently realized, does involve gaseous discharges. These present two types of hazards: high voltage power supplies and vacuum systems requiring optical windows.

Utmost care is called for in handling the high voltages, and all standard precautions and the use of interlocks are strongly recommended. The level of the high voltages required can often be reduced by paralleling sections of discharges. This procedure is strongly recommended since a reduction in the length of discharge sections is also desirable from the point of view of achieving quiet discharge conditions. Of course, all such parallel discharge sections must be separately ballasted to avoid instabilities.

The vacuum system considerations relate more to reliability rather than safety. Because of the small size and the geometry of the discharge system, the danger from the implosion which results from failure of the vacuum system are generally minimal. The use of glass or other insulators is unavoidable in parts of the discharge system, but the system ruggedness and reliability can be improved by the use of metal and metal-ceramic structures where possible. The optical windows are obvious weak links, but the use of O-ring seals on the one hand and metal to ceramic sealing techniques on the other have resulted in rugged, vacuum-tight seals. Alkali halides, which are often used as infra-red optical components because they are relatively cheap, are to be avoided because they are fragile.

The BALAD receiver is a precision optical device. Thus, the same techniques used for optical telescopes should be employed for mounting and supporting this system. Greater care must be exercised at the site of the associated laser transmitter -- which requires far more isolation from vibration and acoustical noise sources. The safety considerations are similar for the transmitter and BALAD receiver, except that the eye hazard must be a major concern at the transmitter, but not at the receiver.

6.0 CONCLUSIONS AND RECOMMENDATIONS

The essential features of an xenon-xenon BALAD receiver system have been demonstrated. The measured properties of the system are given in Table I. As discussed in Section 2, this demonstration has been hampered by the noise in the xenon discharge.

The noise performance of the xenon discharge can be improved by:

- 1) using well-regulated, low-ripple, power supplies, and
- 2) using shorter discharges which are well ballasted.

The xenon cells can be sealed off from the vacuum station, and the xenon pressure can be stabilized by controlling the temperature of a liquid-solid xenon reservoir.²⁰ The noise performance of the He-Xe amplifier at $3.5\mu\text{m}$ has been measured. Under proper operating conditions the effective noise per mode is $11 \pm 0.9 \times 10^{-1}$, which is close to ideal.²¹ Thus the He-Xe amplifier is a good quantum amplifier under proper operating conditions.

Because the greater difficulty was encountered with the absorber discharge, a major effort should be expended to improve that discharge. Clearly, the system could be improved substantially if the xenon absorber were replaced by a passive absorber. Thus, the search for suitable saturable absorbers at 3.5μ and at other wavelengths should also continue.

The theoretical analysis of the propagation of short coherent pulses in resonant absorbers has revealed a non-linear self-focussing effect. This effect would make possible a geometrical loss filter. A modified BALAD receiver system employing such a filter has been analyzed. This system would provide substantial direct filtering of the radiation from other transitions in the CO_2 or other laser preamplifier, and would facilitate the use of standard filters for eliminating the remainder of such broadband background radiation. Thus, the further study of non-linear self-focussing is recommended, to be followed by the development of the geometrical loss filter if the results of the study are favorable.

TABLE I
Xe-Xe BALAD RECEIVER CHARACTERISTICS

Input signal from a He-Xe laser at 3.5 μm	0.28 μW
Output signal to the detector	6.7 μW
Amplifier length	68 cm
Amplifier diameter	1 cm
Absorber length	20 cm
Absorber diameter	0.5 cm
Gas pressure in He-Xe amplifier	2 Torr He, 0.1 Torr Xe
Gas pressure in Xe absorber	0.1 Torr Xe
Small signal gain coefficient of amplifier	$\sim 31 \text{ dB/m}$
Small signal absorption coefficient of absorber α_0	$\sim 60 \text{ dB/m}$
Saturation intensity of amplifier	$\sim 2.5 \text{ mW/cm}^2$
Saturation intensity of absorber	$\sim 0.51 \text{ mW/cm}^2$
Amplification bandwidth at 3.5 μm	$\sim 100 \text{ MHz}$
Absorption bandwidth at 3.5 μm ($\Delta\nu_D$)	$\sim 100 \text{ MHz}$
Saturated transmission hole width in absorber B	$\sim 16 \text{ MHz}$
Possible number of spectral modes ($\Delta\nu_D/B$)	6
Figure-of-Merit of absorber [$F = (\alpha_0 B/I_s)$]	$2.9 \times 10^8 \text{ m/joule}$
Possible number of spatial modes (resolution elements) of amplifier	48
Possible number of spatial modes (resolution elements) of absorber	7
Minimum spot size in absorber	0.17 mm

REFERENCES

1. G. Gould and J. T. LaTourrette, "Bleachable Absorber Laser Amplifier and Detector (BALAD)," RADC TR-72-313, October 1972.
2. J. T. LaTourrette, S. F. Jacobs, and P. Rabinowitz, "Improved Laser Angular Brightness Through Diffraction Coupling," *Appl. Optics*, Vol. 3, p. 981, 1964.
3. J. Nella, Ph.D. Dissertation, Polytechnic Institute of Brooklyn, 1972.
4. C. P. Christensen, C. Freed, and H. A. Haus, "Gain Saturation and Diffusion in CO₂ Lasers," *IEEE J. Quant. Elect.*, Vol. QE-5, p. 276, 1969.
5. S. C. Wang, R. L. Byer, and A. E. Siegman, "Observation of an Enhanced Lamb Dip with a Pure Xe Gain Cell Inside a 3.5 μ m He-Xe Laser," *Appl. Phys. Lett.*, Vol. 17, p. 120, 1970.
6. J. T. LaTourrette, "Doppler Optical Navigator," TRG Technical Report AFAL-TR-67-116, 1967.
7. S. L. McCall and E. L. Hahn, *Phys. Rev. Letters*, 18, 908, 1967.
8. G. L. Lamb, Jr., "Analytic Descriptions of Ultra Short Optical Pulse Propagation in a Resonant Medium," *Rev. Mod. Phys.*, 43, 99-124.
9. H. M. Gibbs and R. E. Slusher, "Optical Pulse Compression by Focusing in a Resonant Absorber," *Appl. Phys. Lett.*, 18, 505, 1971.
10. H. M. Gibbs and R. E. Slusher, "Sharp-Line Self-Induced Transparency," *Phys. Rev. A*, 6, 2326, 1972.
11. S. L. McCall and E. L. Hahn, "Pulse Area-Pulse Energy Description of a Traveling Wave Laser Amplifier," *Phys. Rev.*, Vol. A2, 861-670, 1970.
12. S. Barone and S. Shi, "Propagation of Ultra-Short Optical Pulses in Resonant Non-linear Media," Progress Report No. 36 to JSTAC, PIB, Report No. R452. 36-71, 144-146, 1971.
13. C. K. Rhodes and A. Szoke, "Transmission of Coherent Optical Pulses in Gaseous SF₆," *Phys. Rev.*, Vol. 184, pp. 25-37, 1969.
14. S. A. Akhmanov, A. P. Sukhorukov, and R. V. Khokhlov, "Self-Focusing and Diffraction of Light in a Nonlinear Medium," *Soviet Phys., Uspekhi* (Russian Vol. 93), p. 609, March-April 1968.
15. A. Javan and P. L. Kelley, "Possibility of Self-Focusing Due to Intensity Dependent Anomalous Dispersion," *IEEE J. Quantum Electronics*, Vol. QE-2, p. 470, 1966.
16. D. Grischkowsky and J. A. Armstrong, "Self-Defocusing of Light by Adiabatic Following in Rubidium Vapor," *Phys. Rev.*, A6 p. 1566, October 1972.
17. J. A. Fleck, Jr. and C. Layne, "A Study of Self-Focusing Damage in a High Power Nd Glass Rod Amplifier" (to be published).
18. T. J. Bridges, S. G. Burkhardt, and P. W. Smith, "CO₂ Waveguide Lasers," *Appl. Phys. Lett.*, 20, 403-405, 15 May 1972.
19. J. T. LaTourrette and J. R. Wilson, "Bleachable Absorber Laser Amplifier and Detector (BALAD)," RADC TR-73-172, May 1973.
20. D. R. Armstrong, "A Method for the Control of Pressure in Xenon Laser," *IEEE J. Quantum Electronics*, Vol. 4, p. 966, 1968.
21. J. W. Kluver, "Laser Amplifier Noise at 3.5 Microns in Helium-Xenon," *J. Appl. Phys.*, Vol. 37, p. 2987, 1966.

Appendix A

Propagation of a CW Gaussian Beam in a Saturable Absorber

The propagation of a continuous wave ("cw") confocal beam which has a Gaussian radial profile has been studied to investigate the possibility of self-focusing of such beams. This analysis is based on the formalism which was developed to describe the propagation of a non-saturating beam in a medium with a specified radial dependence of gain coefficient α and/or index of refraction n . In order to present the formalism, a brief review of the latter problem,⁽¹⁾ will first be given. A parabolic radial variation is assumed for the gain coefficient and index of refraction

$$\alpha = \alpha_0 - \frac{1}{2} \alpha_2 r^2, \quad (\text{A. 1})$$

$$n = n_0 - \frac{1}{2} n_2 r^2, \quad (\text{A. 2})$$

where the index of refraction is proportional to the (real) propagation constant θ

$$\theta = \theta_0 - \frac{1}{2} \theta_2 r^2 = (2\pi/\lambda)n. \quad (\text{A. 3})$$

For an absorber, α is negative. L. Casperson, et al.⁽²⁾ extended H. Kogelnik's result to include the frequency dependence of both gain and index of refraction (that is, the "anomalous dispersion") to apply to a high gain 3.5 μm xenon laser operated near threshold. A. Javan, et al.⁽³⁾ studied the problem of self-focusing due to intensity dependent anomalous dispersion. In their treatment of the problem, the inhomogeneous broadening was approximated by a Lorentzian. In the following, the propagation of a cw Gaussian beam is studied, taking into account both a specified radial dependence of gain or absorption and index of refraction such as that caused by a discharge and also the radial dependence caused by saturation by the Gaussian beam profile.

It is convenient to combine (A. 1) and (A. 3) by using the complex propagation constant $k = \theta + i\alpha$, i. e.,

$$k = k_0 - \frac{1}{2} k_2 r^2 \quad (\text{A. 4})$$

where

$$k_0 = \beta_0 + i\alpha_0 \quad \text{and} \quad k_2 = \beta_2 + i\alpha_2 \quad .$$

Assuming the Gaussian beam is of the form

$$E = \exp\{-i[k_0 z + \psi(z)]\} \exp[-i \frac{1}{2} \frac{k_0}{q(z)} r^2] \quad (\text{A. 5})$$

where

k_0 is assumed to be a constant independent of z ,

$\psi(z)$ is a complex phase parameter,

$r = \sqrt{x^2 + y^2}$ is the distance from the optic axis,

and

$q(z)$ is the complex beam parameter given by

$$\frac{1}{q(z)} = \frac{1}{R(z)} - i \frac{\lambda}{\pi w^2(z)} \quad (\text{A. 6})$$

where

$R(z)$ is the radius of curvature of the beam,

$w(z)$ is the spot size of the beam,

and

λ is the wavelength of the beam.

If the Gaussian beam given by (A. 5) is substituted into the scalar wave equation

$$\nabla^2 E + k^2 E = 0 \quad (\text{A. 7})$$

where

$$k^2 \approx k_0^2 - k_0 k_2 r^2 \quad ,$$

one gets the Ricatti equation which governs the propagation of the complex beam parameter, i. e.,

$$\left(\frac{1}{q}\right)^2 + \frac{d}{dz} \left(\frac{1}{q}\right) + \frac{k_2}{k_0} = 0 \quad (\text{A. 8})$$

and the relation between the complex phase parameter and the complex beam parameter is given by

$$\frac{d}{dz} \psi(z) = -i \frac{1}{q(z)} \quad . \quad (\text{A. 9})$$

For a given input beam parameter q_1 , the output beam parameter q_2 can be obtained from the solution of (A. 8), i. e.,

$$\frac{1}{q_2} = \frac{\frac{1}{q_1} \cos \sqrt{(k_2/k_0)}z - \sqrt{k_2/k_0} \sin \sqrt{(k_2/k_0)}z}{\frac{1}{q_1} \sqrt{k_0/k_2} \sin \sqrt{(k_2/k_0)}z + \cos \sqrt{(k_2/k_0)}z} \quad (\text{A. 10})$$

Consider the following cases:

(a) $\sqrt{k_2/k_0} = \pm (\delta + i\epsilon)$, $\delta > 0$, $\epsilon > 0$, i. e., δ and ϵ have the same signs where δ and ϵ are the real and imaginary part of $\sqrt{k_2/k_0}$ respectively. Writing cosine and sine functions in terms of exponential function in (A. 10) and taking the limit $z \rightarrow \infty$, one gets the stationary solution

$$\left(\frac{1}{q_2} \right)_{z \rightarrow \infty} = -i(\delta + i\epsilon) = \epsilon - i\delta \quad (\text{A. 11})$$

From the definition of q given by (A. 6), the stationary radius of curvature R_∞ and the spot size w_∞ are given by

$$R_\infty = \frac{1}{\epsilon} \quad (\text{A. 12})$$

$$w_\infty = \sqrt{\lambda / \pi \delta} \quad (\text{A. 13})$$

(b) $\sqrt{k_2/k_0} = \pm (\delta + i\epsilon)$, $\delta > 0$, $\epsilon < 0$, i. e., δ and ϵ have opposite signs.

Similar to case (a), one gets the stationary value

$$\left(\frac{1}{q_2} \right)_{z \rightarrow \infty} = i(\delta + i\epsilon) = -\epsilon + i\delta \quad (\text{A. 14})$$

$$R_\infty = \frac{1}{-\epsilon} \quad (\text{A. 15})$$

$$w_\infty = \sqrt{\lambda / -\pi \delta} \quad (\text{A. 16})$$

One can see that the spot size w_∞ as given by (A. 16) will be imaginary.

(c) $\sqrt{k_2/k_0} = \pm \delta$, i. e., either (1) $\alpha_2 = \alpha_0 = 0$, i. e., no gain or absorption or (2) $\alpha_2/\alpha_0 = \beta_2/\beta_0$, i. e., an identical radial dependence of gain or absorption and index of refraction. (Note that $\beta_0 = 2\pi m/\lambda \neq 0$ always.)

From solution (A. 10), one obtains that for any input beam parameter q_1 , the output beam parameter q_2 oscillates periodically without approaching a stationary value.

(d) $\sqrt{(k_2/k_0)} = 0$, i. e., $\alpha_2 = 0$, $\theta_2 = 0$, no radial dependence of either gain or absorption coefficient and index of refraction.

From solution (A. 10), one gets the free space result, i. e.,

$$q_2 = q_1 + z \quad . \quad (A. 17)$$

Consider the expression

$$\begin{aligned} \sqrt{\frac{k_2}{k_0}} &= \sqrt{\frac{\theta_2 + i\alpha_2}{\theta_0 + i\alpha_0}} = \sqrt{\frac{\theta_2}{\theta_0} \left(\frac{1 + i(\alpha_2/\theta_2)}{1 + i(\alpha_0/\theta_0)} \right)} \\ &= \left(\frac{\theta_2^2 + \alpha_2^2}{\theta_0^2 + \alpha_0^2} \right)^{1/4} e^{i\phi} \end{aligned} \quad (A. 18)$$

where

$$\phi = \frac{1}{2} \left(\tan^{-1} \frac{\theta_2}{\alpha_2} + \tan^{-1} \frac{\alpha_2}{\theta_2} - \tan^{-1} \frac{\alpha_0}{\theta_0} \right) \quad . \quad (A. 19)$$

Hence the real and imaginary part of $\sqrt{k_2/k_0}$ can be written as

$$\begin{aligned} \delta &= \left(\frac{\theta_2^2 + \alpha_2^2}{\theta_0^2 + \alpha_0^2} \right)^{1/4} \cos\phi \\ \epsilon &= \left(\frac{\theta_2^2 + \alpha_2^2}{\theta_0^2 + \alpha_0^2} \right)^{1/4} \sin\phi \end{aligned} \quad (A. 20)$$

It can be shown that the condition for $\delta > 0$ and $\epsilon > 0$ is given by

$$\alpha_2 > \theta_2 \frac{\alpha_0}{\theta_0} \quad . \quad (A. 21)$$

Radial dependence of gain or absorption coefficient and index of refraction can be caused by either the discharge in the plasma tube or the saturation by a radial dependence Gaussian beam or the combination of the above two effects.

The radial dependence of gain coefficient due to discharge can be assumed to have the form⁽¹⁾

$$\alpha(x) = \alpha_o(x) \left(1 - \frac{r^2}{r_o^2}\right) \quad (\text{A. 22})$$

where

$$\alpha_o(x) = \alpha_P e^{-x^2}, \quad x = 2\sqrt{\ln 2} \frac{\nu - \nu_o}{\Delta\nu_D} \quad (\text{A. 23})$$

α_P : the peak gain value at line center

$\Delta\nu_D$: the full doppler width at half the central value

r_o : the radius of the plasma tube.

In the case of absorber, α_P is negative. Comparing (A. 22) with (A. 1), we have

$$\alpha_o = \alpha_o(x) \quad (\text{A. 24})$$

$$\alpha_2 = \frac{2\alpha_o(x)}{r_o^2} \quad (\text{A. 25})$$

The corresponding index of refraction can be calculated by Kramers Kronig relations

$$\frac{2\pi}{\lambda} (n - 1) = \frac{1}{\pi} \text{P. V.} \int_{-\infty}^{\infty} \frac{\alpha(\nu')}{\nu' - \nu} d\nu' \quad (\text{A. 26})$$

$$= \frac{2\alpha_P}{\sqrt{\lambda}} F(x) \left(1 - \frac{r^2}{r_o^2}\right) \quad (\text{A. 27})$$

where $F(x)$ is Dawson's integral⁽⁴⁾ given by

$$F(x) = e^{-x^2} \int_0^x e^{t^2} dt \quad (\text{A. 28})$$

The index of refraction can be written as

$$n(x) = 1 + \frac{\lambda \alpha_P}{\pi^{3/2}} F(x) \left(1 - \frac{r^2}{r_o^2}\right) \quad . \quad (A. 29)$$

Comparing (A. 29) with (A. 2), we have

$$n_o = 1 + \frac{\lambda \alpha_P}{\pi^{3/2}} F(x) \quad (A. 30)$$

$$n_2 = \frac{2\lambda \alpha_P}{\pi^{3/2} r_o^2} F(x) \quad . \quad (A. 31)$$

The radial dependence of gain or absorption and index of refraction caused by saturation of a Gaussian beam can be calculated as follows. The gain coefficient of the doppler broadened medium in the presence of a saturation field I' is given by

$$\alpha(x) = \frac{\alpha_o(x)}{\sqrt{1 + (I'/I_s)}} \quad (A. 32)$$

where broad doppler width has been assumed. I_s is the saturation intensity of the medium. Let the Gaussian beam be

$$I' = I \exp[-(r^2/w^2)] \quad (A. 33)$$

where w is the spot size which reduces the intensity by $1/e$ of its central value. Substituting (A. 33) into (A. 32) and making an expansion in the region $(r^2/w^2) \ll 1$, one gets

$$\alpha(x) \approx \frac{\alpha_o(x)}{\sqrt{1 + (I/I_s)}} \left[1 + \frac{1}{2} \frac{I/I_s}{1 + (I/I_s)} \frac{r^2}{w^2} \right] \quad . \quad (A. 34)$$

Comparing (A. 34) with (A. 1), the following results are obtained

$$\alpha_o = \frac{\alpha_o(x)}{\sqrt{1 + (I/I_s)}} \quad (A. 35)$$

$$\alpha_2 = - \frac{\alpha_o(x)}{\sqrt{1 + (I/I_s)}} \frac{I/I_s}{1 + (I/I_s)} \frac{1}{w^2} \quad . \quad (A. 36)$$

The index of refraction for inhomogeneous broadening laser medium in the limit

$$2\sqrt{\ln 2} \left(\frac{\Delta\nu}{\Delta\nu_D} \right) \sqrt{1 + (I/I_s)} \ll 1, \quad (A. 36)$$

where $\Delta\nu$ is the full homogeneous line width at half the central value can be written as⁽⁵⁾

$$n(x) = 1 + \frac{\lambda\alpha_P}{\pi} \left[\frac{F(x)}{\sqrt{\pi}} - 2\sqrt{\ln 2} \left(\frac{\Delta\nu}{\Delta\nu_D} \right) \sqrt{1 + (I/I_s)} x \exp(-x^2) \right]. \quad (A. 37)$$

Substituting the Gaussian beam (A. 33) into (A. 37), we get the following expression in the limit $(r^2/w^2) \ll 1$,

$$n(x) = 1 + \frac{\lambda\alpha_P}{\pi} \left[\frac{F(x)}{\sqrt{\pi}} - 2\sqrt{\ln 2} \left(\frac{\Delta\nu}{\Delta\nu_D} \right) \sqrt{1 + (I/I_s)} \left(1 - \frac{1}{2} \frac{I/I_s}{1 + (I/I_s)} \frac{r^2}{w^2} \right) x \exp(-x^2) \right]. \quad (A. 38)$$

Comparing (A. 38) with (A. 2), one gets

$$n_0 = 1 + \frac{\lambda\alpha_P}{\pi} \left[\frac{F(x)}{\sqrt{\pi}} - 2\sqrt{\ln 2} \left(\frac{\Delta\nu}{\Delta\nu_D} \right) \sqrt{1 + (I/I_s)} x \exp(-x^2) \right] \quad (A. 39)$$

$$n_2 = - \frac{\lambda\alpha_P}{\pi} 2\sqrt{\ln 2} \left(\frac{\Delta\nu}{\Delta\nu_D} \right) \frac{I/I_s}{\sqrt{1 + (I/I_s)}} \frac{x \exp(-x^2)}{w^2}. \quad (A. 40)$$

If radial dependence of gain or absorption and index of refraction due to both discharge and the saturation effect are taken into considerations, then the gain coefficient and the index of refraction are given by

$$\alpha_0 = \frac{\alpha_0(x)}{\sqrt{1 + (I/I_s)}} \quad (A. 41)$$

$$\alpha_2 = \alpha_0(x) \left\{ \frac{2}{r_0^2} - \frac{I/I_s}{[1 + (I/I_s)]^{3/2}} \frac{1}{w^2} \right\} \quad (A. 42)$$

$$n_0 = 1 + \frac{\lambda\alpha_P}{\pi} \left[\frac{F(x)}{\sqrt{\pi}} - 2\sqrt{\ln 2} \left(\frac{\Delta\nu}{\Delta\nu_D} \right) \sqrt{1 + (I/I_s)} x \exp(-x^2) \right] \quad (A. 43)$$

$$n_2 = \frac{\lambda\alpha_P}{\pi} \left[\frac{2F(x)}{\sqrt{\pi} r_0^2} - 2\sqrt{\ln 2} \left(\frac{\Delta\nu}{\Delta\nu_D} \right) \frac{I/I_s}{\sqrt{1 + (I/I_s)}} \frac{x \exp(-x^2)}{w^2} \right]. \quad (A. 44)$$

In the following, the focusing and defocusing effects of saturable absorber will be studied. The results will be compared with those obtained from an amplifier. Generally, θ_0 is much larger than α_0 , i.e., $\theta_0 \gg \alpha_0$, one can write

$$\sqrt{k_2/k_0} \approx \sqrt{\theta_2 + i\alpha_2/\theta_0} = \sqrt{\alpha_2/\theta_0} \sqrt{i[1 - i(\theta_2/\alpha_2)]} \quad (\text{A. 45})$$

The ratio θ_2/α_2 can be shown to be much smaller than one for small frequency deviation from the line center for the following two cases:

Case 1: α_2 and θ_2 caused by the discharge.

Taking the ratio of (A. 31) and (A. 25), we have

$$\frac{\theta_2}{\alpha_2} = \frac{(2\pi/\lambda)n_2}{\alpha_2} = \frac{2}{\sqrt{\pi}} \frac{F(x)}{\exp(-x^2)} \quad (\text{A. 46})$$

(A. 46) is smaller than one if x is much smaller than about $1/2$.

Case 2: α_2 and θ_2 caused by saturation of a Gaussian beam.

From (A. 36) and (A. 40), we have

$$\frac{\theta_2}{\alpha_2} = (1 + \frac{I}{I_s}) 4\sqrt{\ln 2} \left(\frac{\Delta\nu}{\Delta\nu_D} \right) x \quad (\text{A. 47})$$

(A. 47) is much smaller than one if

$$x \ll \frac{1}{[1 + (I/I_s)] 4\sqrt{\ln 2} (\Delta\nu/\Delta\nu_D)}$$

For small frequency deviation from the line center, expression (A. 45) can be expanded in series.

Consider the case where a weak Gaussian beam is propagating through an absorber which has the absorption coefficient and index of refraction given by (A. 22) and (A. 29) respectively. In this case, α_p given by (A. 23) is negative. From (A. 24) and (A. 25), the absorption coefficient of the absorber has the following sign:

$$\alpha_0 < 0 \quad \text{and} \quad \alpha_2 < 0.$$

(i) For small frequency shift to the high frequency side from the atomic line center, i. e., $x > 0$, the radial dependent part of refractive index n_2 has a positive sign as can be seen from (A. 31). This implies that $\theta_2 > 0$. Writing $\alpha_2 = -|\alpha_2|$, we have from (A. 45) the following result

$$\begin{aligned}\sqrt{k_2/k_0} &= \sqrt{|\alpha_2|/2\theta_0} \frac{(1-i)}{\sqrt{2}} \left(1 + i \frac{1}{2} \frac{\theta_2}{|\alpha_2|}\right) \\ &= \sqrt{|\alpha_2|/2\theta_0} \left[\left(1 + \frac{1}{2} \frac{\theta_2}{|\alpha_2|}\right) - i \left(1 - \frac{1}{2} \frac{\theta_2}{|\alpha_2|}\right) \right].\end{aligned}\quad (\text{A. 48})$$

Expression (A. 48) is valid for $\theta_2/|\alpha_2| \ll 1$.

The real and imaginary part of $\sqrt{k_2/k_0}$ are given by

$$\delta = \sqrt{|\alpha_2|/2\theta_0} \left(1 + \frac{1}{2} \frac{\theta_2}{|\alpha_2|}\right) \quad (\text{A. 49})$$

$$\epsilon = -\sqrt{|\alpha_2|/2\theta_0} \left(1 - \frac{1}{2} \frac{\theta_2}{|\alpha_2|}\right). \quad (\text{A. 50})$$

δ and ϵ have opposite signs. If (A. 49) is substituted into (A. 16), one sees that ω_∞ will be imaginary. Focusing cannot occur.

(ii) For small frequency shift to the low frequency side from the line center, θ_2 will be negative, i. e., $\theta_2 < 0$. Writing $\theta_2 = -|\theta_2|$, we have from (A. 45) in the limit $\frac{|\theta_2|}{|\alpha_2|} \ll 1$,

$$\sqrt{k_2/k_0} = \sqrt{|\alpha_2|/2\theta_0} \left[\left(1 - \frac{1}{2} \frac{|\theta_2|}{|\alpha_2|}\right) - i \left(1 + \frac{1}{2} \frac{|\theta_2|}{|\alpha_2|}\right) \right]. \quad (\text{A. 51})$$

Therefore δ and ϵ are given by

$$\delta = \sqrt{|\alpha_2|/2\theta_0} \left(1 - \frac{1}{2} \frac{|\theta_2|}{|\alpha_2|}\right) \quad (\text{A. 52})$$

$$\epsilon = -\sqrt{|\alpha_2|/2\theta_0} \left(1 + \frac{1}{2} \frac{|\theta_2|}{|\alpha_2|}\right). \quad (\text{A. 53})$$

Again, δ and ϵ have opposite signs so that focusing cannot be obtained.

Consider the case where the absorber is saturated by a strong Gaussian beam. The radial dependence of absorption coefficient and index of

refraction are assumed to be mainly produced by the strong field so that (A. 34) and (A. 38) are applicable. The absorption coefficient of the saturable absorber have the following signs: $\alpha_0 < 0$, $\alpha_2 > 0$. α_0 and α_2 are given by (A. 35) and (A. 36), respectively, where $\alpha_0(x)$ is negative.

(iii) On the high frequency side from the line center ($\theta_2 > 0$), we can obtain from (A. 45) in the limit $\theta_2/\alpha_2 \ll 1$,

$$\delta = \sqrt{\alpha_2/2\theta_0} [1 + (\theta_2/\alpha_2)] \quad (\text{A. 54})$$

$$\epsilon = \sqrt{\alpha_2/2\theta_0} [1 - (\theta_2/\alpha_2)] \quad (\text{A. 55})$$

δ and ϵ have the same sign. There is a stationary value of w_∞ . Focusing will occur. From (A. 12), (A. 13), (A. 54), and (A. 55), one can obtain the expressions of stationary spot size and radius of curvature

$$w_\infty = \left[(\pi/\lambda)^2 \frac{\alpha_2}{2\theta_0} \left(1 + \frac{\theta_2}{\alpha_2}\right)^2 \right]^{-1/4} \quad (\text{A. 56})$$

$$R_\infty = \left[\frac{\alpha_2}{2\theta_0} \left(1 - \frac{\theta_2}{\alpha_2}\right)^2 \right]^{-1/2} \quad (\text{A. 57})$$

If the expressions of α_0 , n_0 and θ_2/α_2 as given by (A. 36), (A. 39), and (A. 47) are substituted into (A. 56) and (A. 57), one obtains after some calculations

$$w_\infty(x) = \left[\frac{4 \left\{ 1 + \frac{\lambda \alpha_P}{\pi} \left[\frac{F(x)}{\sqrt{\pi}} - 2\sqrt{\ln 2} \left(\frac{\Delta\nu}{\Delta\nu_D} \right) \sqrt{1 + (I/I_s)} x \exp(-x^2) \right] \right\}}{\frac{\pi}{\lambda} \left(\frac{\alpha_P \exp(-x^2)}{\sqrt{1 + (I/I_s)}} \frac{1/I_s}{1 + (I/I_s)} \right) \left[1 + \left(1 + \frac{I}{I_s} \right) + \sqrt{\ln 2} \left(\frac{\Delta\nu}{\Delta\nu_D} \right) x \right]^2} \right]^{1/2} \quad (\text{A. 58})$$

$$R_{\infty}(x) = \frac{4 \left\{ 1 + \frac{\lambda \alpha_P}{\pi} \left[\frac{F(x)}{\sqrt{\pi}} - 2 \sqrt{\ln 2} \left(\frac{\Delta \nu}{\Delta \nu_D} \right) \sqrt{1 + (I/I_s)} x \exp(-x^2) \right] \right\}}{\frac{\alpha_P \exp(-x^2)}{\sqrt{1 + (I/I_s)}} \frac{I/I_s}{1 + (I/I_s)}} \cdot \left[\frac{1}{\left\{ 1 - \left[\left(1 + \frac{I}{I_s} \right) 4 \sqrt{\ln 2} \left(\frac{\Delta \nu}{\Delta \nu_D} \right) x \right]^2 \right\}} \right] \quad (\text{A. 59})$$

(A. 58) and (A. 59) are valid for

$$0 < x \ll \frac{1}{\left(1 + \frac{I}{I_s} \right) 4 \sqrt{\ln 2} \left(\frac{\Delta \nu}{\Delta \nu_D} \right)}$$

(iv) On the low frequency side from the line center, $\theta_2 < 0$, we can obtain from (A. 45) in the limit $\frac{|\theta_2|}{|\alpha_2|} \ll 1$,

$$\delta = \sqrt{\alpha_2/2\theta_0} \left(1 - \frac{|\theta_2|}{\alpha_2} \right) \quad (\text{A. 60})$$

$$\epsilon = \sqrt{\alpha_2/2\theta_0} \left(1 + \frac{|\theta_2|}{\alpha_2} \right) \quad (\text{A. 61})$$

δ and ϵ have the same sign so that focusing occurs. As the frequency shifts more to the lower frequency side from the line center, $|\theta_2|$ will increase and δ will decrease, as can be seen from (A. 60). Since the spot size varies inversely as the square root of δ , it will increase as δ decreases. Similarly, the stationary spot size is found to be

$$w_{\infty}(x) = \left[\frac{4 \left\{ 1 + \frac{\lambda \alpha_P}{\pi} \left[\frac{F(x)}{\sqrt{\pi}} - 2 \sqrt{\ln 2} \left(\frac{\Delta \nu}{\Delta \nu_D} \right) \sqrt{1 + (I/I_s)} x \exp(-x^2) \right] \right\}}{\frac{\pi}{\lambda} \left(\frac{\alpha_P \exp(-x^2)}{\sqrt{1 + (I/I_s)}} \frac{I/I_s}{1 + (I/I_s)} \right) \left[1 - \left(1 + \frac{I}{I_s} \right) 4 \sqrt{\ln 2} \left(\frac{\Delta \nu}{\Delta \nu_D} \right) x \right]^2} \right]^{1/2} \quad (\text{A. 62})$$

$R_{\infty}(x)$ has identical expression as (A. 59). (A. 62) is valid for

$$\frac{-1}{\left(1 + \frac{I}{I_s}\right) 4 \sqrt{\ln 2} \left(\frac{\Delta v}{\Delta v_D}\right)} \ll x < 0 \quad .$$

(A. 58) and (A. 62) can be combined to one expression

$$u_\infty(x) = \left[\frac{4 \left\{ 1 + \frac{\lambda \alpha_P}{\pi} \left[\frac{F(x)}{\sqrt{\lambda}} - 2 \sqrt{\ln 2} \left(\frac{\Delta v}{\Delta v_D} \right) \sqrt{1 + (I/I_s)} x \exp(-x^2) \right] \right\}}{\frac{\pi}{\lambda} \left(\frac{\alpha_P \exp(-x^2)}{\sqrt{1 + (I/I_s)}} \frac{I/I_s}{1 + (I/I_s)} \right) \left[1 + \left(1 + \frac{I}{I_s} \right) 4 \sqrt{\ln 2} \left(\frac{\Delta v}{\Delta v_D} \right) |x| \right]^2} \right]^{1/2} \quad (A. 63)$$

where

$$|x| \ll \frac{1}{\left(1 + \frac{I}{I_s}\right) 4 \sqrt{\ln 2} \left(\frac{\Delta v}{\Delta v_D}\right)} \quad .$$

A plot of (A. 63) and (A. 59) are shown in Figs. A.1 and A.2 for the case of xenon absorber at different intensities. The following value of parameters are used: $\lambda = 3.5 \mu\text{m}$, $\alpha_P = 13.85/\text{m}$, $\Delta v/\Delta v_D \approx 0.1$.

As a comparison to the amplifier, one can easily show that for the case of unsaturated amplifier which has the radial dependence of gain coefficient and index of refraction due to the discharge alone has the same expressions as (A. 54) and (A. 55) for $\alpha_0 > 0$, $\alpha_2 > 0$, $\beta_2 > 0$ (i. e., high frequency side and the same expression as (A. 60) and (A. 61) for $\alpha_0 > 0$, $\alpha_2 > 0$, $\beta_2 < 0$ (i. e., low frequency side). Therefore, focusing can be obtained on the high frequency side from line center and defocusing will be obtained on the low frequency side from the line center. The above results have been pointed out by L. Caspersen, et al. (2)

In the case of a saturated amplifier whose radial dependence of gain coefficient and index of refraction are dominated by the saturating Gaussian field, identical results as given by (A. 49) and (A. 50) will be obtained for $\alpha_0 > 0$, $\alpha_2 < 0$, $\beta_2 > 0$ (high frequency side), and identical results as given by (A. 52) and (A. 53) will be obtained for $\alpha_0 > 0$, $\alpha_2 < 0$, $\beta_2 < 0$ (low frequency side). Therefore focusing will not occur on either side of the line center.

One interesting case is when there is only radial dependence of refractive index and neither radial dependence of gain nor absorption, i. e., $\beta_2 \neq 0$, $\alpha_2 = 0$.

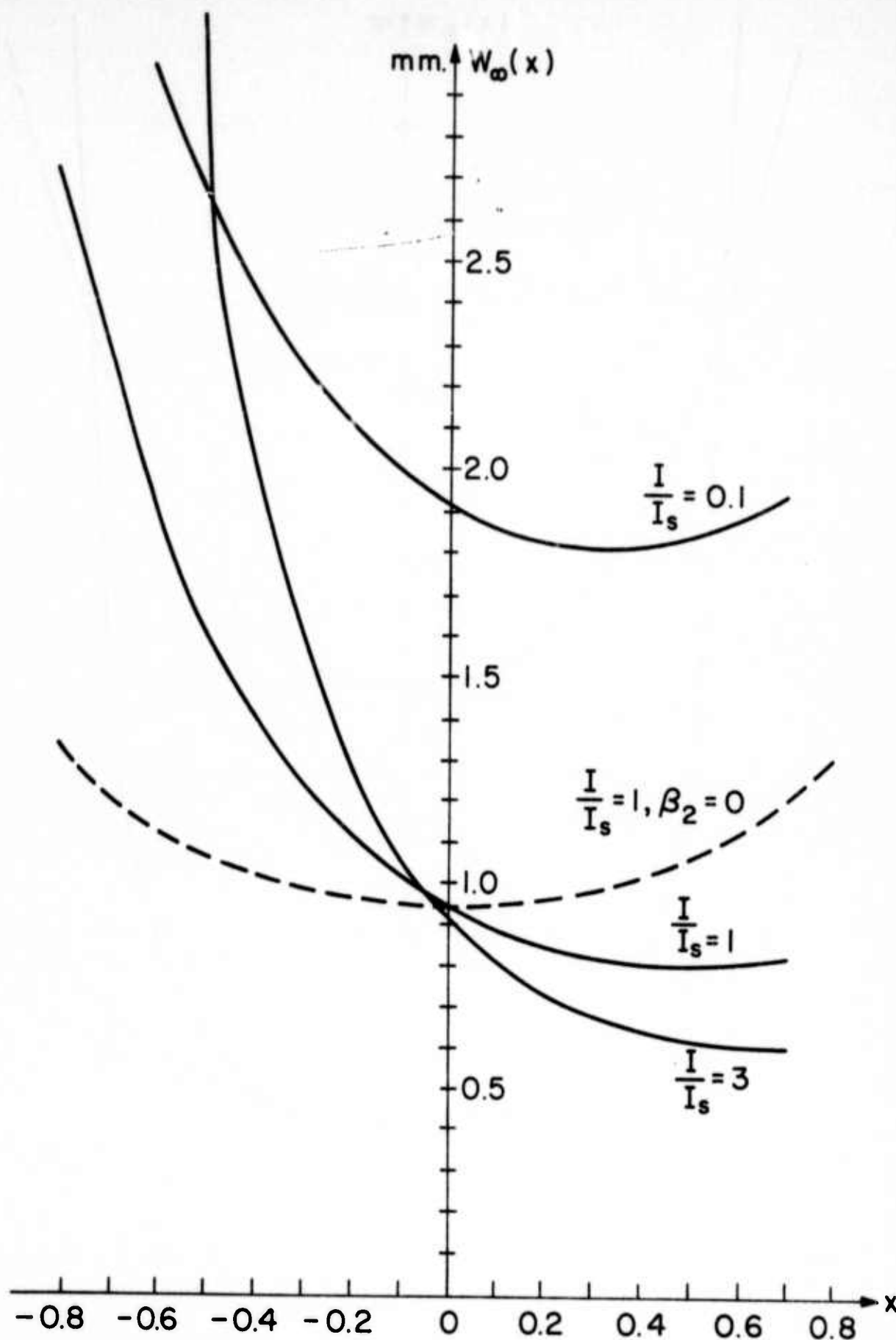


Fig. A.1 - (Solid Line) Stationary beam radius vs. frequency deviation from line center ($x = 2\sqrt{\log 2} \frac{\nu - \nu_0}{\Delta \nu D}$) for $I/I_s = (0.1, 1, 3)$, $\beta_2 \neq 0$ (i.e., radial dependence of index of refraction). (Broken Line) $I/I_s = 1$, $\beta_2 = 0$ (i.e., no radial dependence of index of refraction).

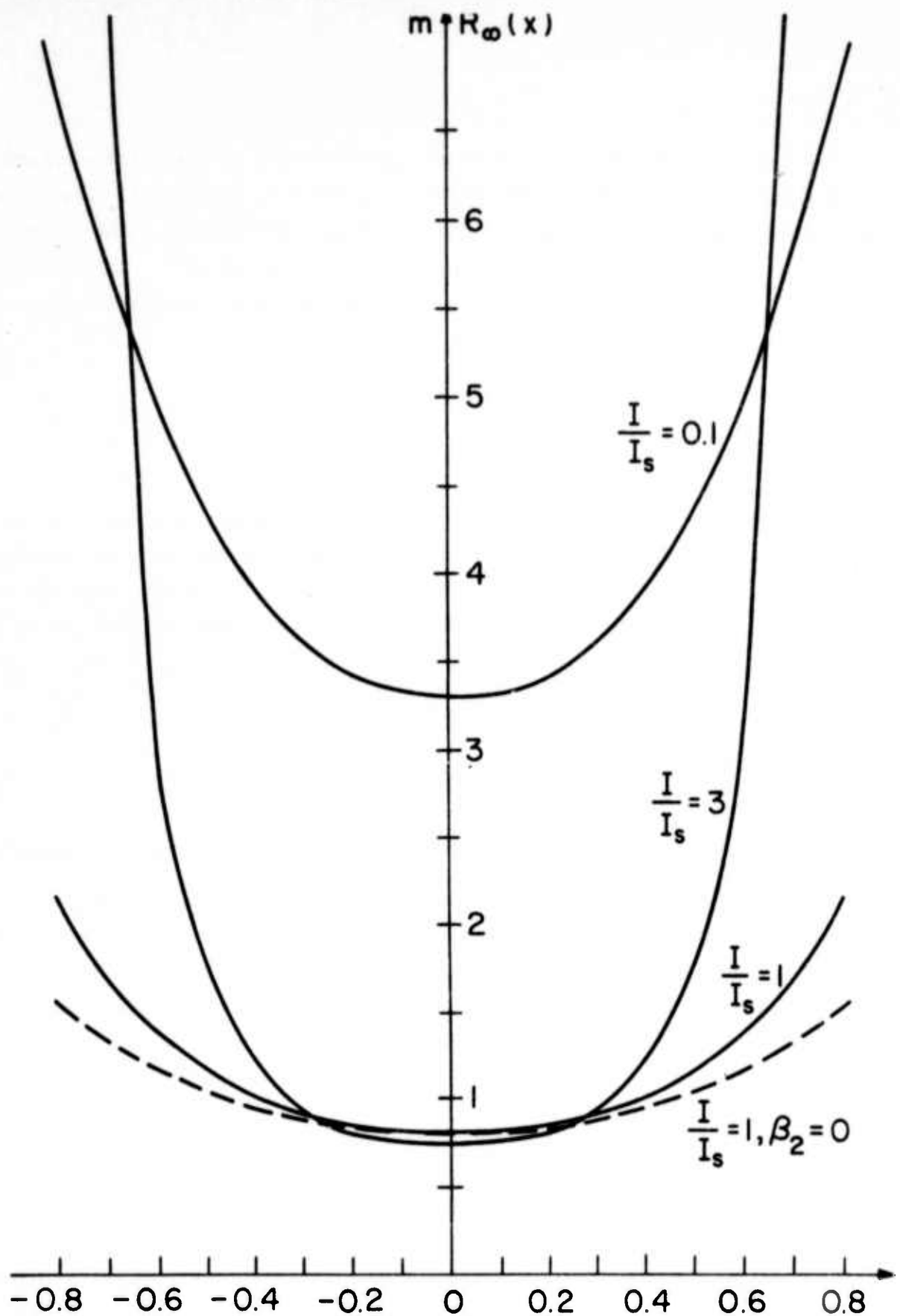


Fig. A. 2 - (Solid Line) Radius of curvature of the Gaussian wave vs. frequency deviation from line center for I/I_s ($=0.1, 1, 3$), $\beta_2 \neq 0$ (i.e., radial dependence of index of refraction). (Broken Line) $I/I_s = 1$, $\beta_2 = 0$ (i.e., no radial dependence of index of refraction).

the medium behaves like a converging lens only on one frequency side from line center. In the case of absorber ($\alpha_0 < 0$), there will be focusing on high frequency side from the line center and defocusing on low frequency side from the line center. The stationary spot size and radius of curvature for $\alpha_0 < 0$, $\beta_2 > 0$ (high frequency side) can be found to be

$$w_\infty = [(\pi/\lambda)^2 (\beta_2/\beta_0)]^{-1/4} \quad (\text{A. 64})$$

$$R_\infty = \left[\frac{1}{4} (|\alpha_0|/\beta_0)^2 (\beta_2/\beta_0) \right]^{-1/2} \quad (\text{A. 65})$$

In the case of the amplifier ($\alpha_0 > 0$), there will be focusing on low frequency side from the line center and there will be defocusing on high frequency side from the line center. The stationary spot size and radius of curvature for $\alpha_0 > 0$, $\beta_2 < 0$ (low frequency side) can be found to be

$$w_\infty = \left[(\pi/\lambda)^2 \frac{1}{4} (\alpha_0/\beta_0)^2 (|\beta_2|/\beta_0) \right]^{-1/4} \quad (\text{A. 66})$$

$$R_\infty = (|\beta_2|/2\beta_0)^{-1/2} \quad (\text{A. 67})$$

The above properties have been pointed out by A. Javan, et al.⁽³⁾

The other interesting case is when there is only radial dependence of either gain or absorption and no radial dependence of refractive index, i. e., $\alpha_2 \neq 0$, $\beta_2 = 0$, the medium behaves as a converging lens only when the amplifier is not saturated and also when the absorber is saturated. The stationary spot size and radius of curvature of an unsaturated amplifier, i. e., $\alpha_0 > 0$, $\alpha_2 > 0$ can be found to be

$$w_\infty = [(\pi/\lambda)^2 (\alpha_2/2\beta_0)]^{-1/4} \quad (\text{A. 68})$$

$$R_\infty = (\alpha_2/2\beta_0)^{-1/2} \quad (\text{A. 69})$$

Results (A. 68) and (A. 69) have been calculated by H. Kogelnik.⁽¹⁾ For a saturated absorber, i. e., $\alpha_0 < 0$, $\alpha_2 > 0$, the stationary spot size and radius of curvature are identical to (A. 68) and (A. 69). A plot of (A. 68) and (A. 69) are shown in Figs. A.1 and A.2 by a dash line as a comparison for the cases where $\beta_2 \neq 0$.

REFERENCES

1. H. Kogelnik, "On the Propagation of Gaussian Beams of Light through Lenslike Media including those with a Loss or Gain Variation," Appl. Optics, Vol. 4, p. 562, 1965.
2. L.W. Casperson and A. Yariv, "Gain and Dispersion Focusing in a High Gain Laser," Appl. Optics, Vol. 11, p. 462, 1972.
3. A. Javan and P.L. Kelley, "Possibility of Self-Focusing Due to Intensity Dependent Anomalous Dispersion," IEEE J. Quant. Elect. Vol. QE-2, p. 470, 1966.
4. Handbook of Mathematical Functions, edited by M. Abramowitz and I.A. Stegun (U.S. Department of Commerce, National Bureau of Standards, Washington, D.C. 1964), p. 297-304, 325-328.
5. D.H. Close, "Strong Field Saturation Effects in Laser Media," Phys. Rev., Vo. 153, p. 360, 1967.

Appendix B

Analysis and Description of Numerical Procedure

We will now discuss the numerical integration of the normalized working equations:

$$\partial_z \mathcal{E} = ic_1 [\partial_{\phi\phi} + \frac{1}{\phi} \partial_{\phi}] \mathcal{E} - \sigma \mathcal{E} + g\theta \quad (\text{B. 1})$$

$$\partial_{\tau} \theta = -(\frac{1}{T_2} + \Delta\omega) \theta + \mathcal{E} W \quad (\text{B. 2a})$$

$$\partial_{\tau} W = -(W - W_0)/T_1 - \text{Re}\{\theta \mathcal{E}^*\} \quad (\text{B. 2b})$$

where c_1 , σ , g , T_1 , T_2 , $\Delta\omega$, W_0 are constants and θ and \mathcal{E} are the normalized slowly varying complex envelopes of the macroscopic polarization and electric field respectively. W is the macroscopic population inversion of the two-state atomic system. The numerical scheme we have chosen is basically described in the paper by Içsevçi and Lamb.¹ The normalized transformed independent variables (τ, ϕ, ϕ) are defined in the text. The input conditions are $\mathcal{E}(z=0, \phi, \tau)$ and $\theta, W(\tau, \phi, \tau=0)$. That is, the \mathcal{E} -field is prescribed just inside the beginning of the medium (the wave propagates in the positive z -direction) and W, θ assume their initial status before the arrival of the perturbing \mathcal{E} -field. Computation always begins at $\tau = 0$ which physically would correspond to an observer at some position z down range turning on his detector only after the a time z/c has past since the pulse entered the medium at $z = 0$. The 3-dimensional grid space ϕ_m, τ_n where the field is to be evaluated is filled in a manner consistent with the proper use of a predictor-corrector numerical integration scheme for both the field equation and medium equations. Once the \mathcal{E} -field is known at some z -plane, we use Eq. (B. 1) to guess (predict) the \mathcal{E} -field in the entire $z + \Delta z$ plane. The value of Δz is necessarily small since we are assuming τ and ϕ variations are small between z and $z + \Delta z$. Now, given the values of θ and W at $\tau = 0$ for all ϕ , we march θ and W in τ using Eqs. (B. 2a) and (B. 2b) as if they were initial value ordinary differential equations. The values of the mesh separations are determined by the combined considerations of local stability tests, experimentation, and cost effective use of computation time. The dependent variable guessed (predicted) at the next forward mesh point is evaluated using only quantities that have been corrected. For example, to predict θ at some time point $\tau + \Delta\tau$ only previously corrected values of

θ , \mathcal{E} , and W at mesh points τ and $\tau - \Delta\tau$ are used. This is absolutely necessary if the predictor-corrector (P-C) is to be used at maximum accuracy. We have analyzed the scheme and found it to be conditionally stable and consistent to within 2nd order in $\Delta\tau$, $\Delta\phi$, Δn . A more detailed derivation of these results is given in N. Wright's Ph. D. thesis². It is known for maximum efficiency of the P-C scheme one should use only one iteration. This we have done. We found only one special case where the θ and W equations become unstable (namely, the rate equation limit of very short $T_2 \leq T_P/5$). The stability problem always arose in the \mathcal{E} -field equation since the ratio of $c_1(\Delta\tau)/(\Delta\phi)^2$ does have values where the scheme is conditionally unstable. For maximum accuracy the parameter $\Delta\tau/\Delta\phi^2$ was chosen to be as close to the unstable region as possible. Other researchers have also found this condition to be true.⁽³⁾ We have used the well-known trick of transforming to a stretched coordinate frame.⁽³⁾ Stability considerations are unaffected by such a transformation since the stability is evaluated locally where the equations are linear. The transformation we used clustered sampling data where the derivatives with respect to τ were largest. The explicit transformation was: $T = 1/2(1 + \tanh\{(\tau - \tau_0)/\alpha\})$ where α is the stretching factor making mesh points more dense about τ_0 the center of the transformation. τ_0 is chosen to reside near the peak of the electric field amplitude. This transformation allowed us to obtain with 60 computational time points an accuracy obtainable only with 150 or better real time mesh points. This saves a significant amount of C-P time for multi-dimensional equations. There are penalties associated with the use of this procedure. In our case at $T \approx 1$ which corresponds to τ near infinity the inverse transformation needed to calculate ∂_T tends to infinity. Thus information gathered near $T \approx 1$ is necessarily regarded with skepticism. In the normal situation, the field has decayed to zero at this point. The number of mesh points at $T \approx 1$ and $T = 0$ is very sparse. At $T \approx 0$ the field is always zero or near zero. Also, the field at $T \approx 1$ cannot effect the field at $T = 1 - \Delta T$ via causality. Peculiarities at $T = 1$ are discarded.

The transverse boundary condition applied to the explicit scheme can play a substantial role in determining the propagating field when the field gets large at the transverse boundaries. Strictly speaking, a linearly polarized electric field is inconsistent with the rotationally symmetric vector wave equation despite the fact nearly linearly polarized fields do exist in laser oscillators. If the walls are at infinity where the field is zero, they play no role and the

boundary conditions are physically realistic. In the absorbing type medium, this condition is always satisfied even though the walls are at ≈ 1 cm. In an amplifying type medium, the field at the walls is quite substantial after a few amplifying lengths and play a large role in determining the overall \mathcal{E} -field. Mathematically this boundary condition is $(\partial \rho \mathcal{E} / \mathcal{E}) = 0$. Numerically this is translated into $\mathcal{E}_1 = (4\mathcal{E}_2 - \mathcal{E}_3)/3.0$ where 1, 2, 3 correspond to the 3 mesh modes at the wall of the medium ($0 = \text{wall}$ corresponds to 0_1). This expression is accurate to 1st order in Δo .

The propagation of the \mathcal{E} -field in free space or under the action of a focusing lens is handled by a simple quadrature integration in subroutine LENS. In free space, one can obtain the solution of the reduced wave equation by examining a good table of integrals. The Green's function propagator can sometimes be integrated analytically with some reasonable input field. However, for the case where the input field at some z is given only at specific mesh points the integration is easily handled numerically. Care must be taken to insure enough mesh points are given to handle large phase variations over the aperture. By comparing results with a known integrable case (Gaussian input) we experimentally determined how many 2π -phase cycles are allowed to obtain reasonable results. The finite difference equations for the coupled equations are:

$$e'_{m,n}{}^{+1} = \frac{\tilde{e}'_{m,n}{}^{+1} + e'_{m,n}}{2.0} + \frac{\Delta \pi}{4.0} \{ \partial_- \tilde{e}'_{m,n}{}^{+1} + \partial_- e'_{m,n} \}$$

where

$$\begin{aligned} \partial_- e'_{m,n}{}^{+1} = & g\theta_{m,n} + ic_1 \left\{ \frac{e'_{m+1,n}{}^{+1} + e'_{m-1,n}{}^{+1} - 2e'_{m,n}{}^{+1}}{(\Delta o)^2} \right. \\ & \left. + \frac{e'_{m+1,n}{}^{+1} - e'_{m-1,n}{}^{+1}}{(2\Delta o)(m\Delta o)} \right\} - \pi e'_{m,n}{}^{+1} \end{aligned}$$

and

$$\tilde{e}'_{m,n}{}^{+1} = e'_{m,n}{}^{+1} + 2\Delta \pi \partial_- e'_{m,n}{}^{+1}$$

where

- ℓ corresponds to longitudinal position $z_\ell = \ell \Delta z$
 n corresponds to time point τ_n , i. e., $\tau_1 = -\infty$
 m corresponds to space point $o_m = m \Delta o$.

Similarly for W and ϕ :

$$W_{m,n+1}^{\ell+1} = \frac{\tilde{W}_{m,n+1}^{\ell+1} + W_{m,n}^{\ell+1}}{2} + \frac{\Delta\tau}{2} \{ \partial_\tau \tilde{W}_{m,n+1}^{\ell+1} + \partial_\tau W_{m,n}^{\ell+1} \}$$

where

$$\tilde{W}_{m,n+1}^{\ell+1} = W_{m,n-1}^{\ell+1} + 2\Delta\tau \partial_\tau W_{m,n}^{\ell+1}$$

and

$$\partial_\tau W_{m,n}^{\ell} = -(W_{m,n}^{\ell} - W_{m,0}^{\ell})/T_1 - \text{Re}\{\phi_{m,n}^{\ell} e_{m,n}^{\ell*}\}.$$

To further understand the numerical procedure, the flow charts of the main and integration subroutines are given in Figs. B1, B2, and B3 with additional descriptions. The main subroutine acts as an executive supervising routine which controls the flow of computation. Its main functions are to calculate the electric field at $z = \Delta z$, refresh memory allocations, call input and output functions and terminate execution. The integration of ϕ , W , and ℓ requires three space or time levels. Thus, to obtain ℓ at $z = 2\Delta z$ will require ℓ at $z = 0$, and $z = \Delta z$. This method cannot be applied in determining ℓ at $z = \Delta z$. The main subroutine calculates ℓ at $z = \Delta z$ using a simple iterated Euler finite difference approximation. This calculation of ℓ at $z = \Delta z$ uses subroutine "SUM" but the logic for this one-time only calculation is not included in the flow chart for "SUM." Subroutines "LYGRE" and "GRAHAM" perform almost all input and output functions, respectively.

The purpose of the flow charts is to give the reader the overall flow of the logic. It is not a detailed road map. The detailed flow chart would include various straight forward programming techniques to save memory space and time. The logic for conversion of ∂_τ to $g_T^{-1}(T)\partial_T$ of the stretching computational space is not given. Also there is no need to have ϕ and W as two-dimensional arrays indicated in the diagrams. Making them one dimensional also requires the inclusion of a special output format instruction. Such a detailed flow chart would be unnecessarily complicated. A listing of the program with copious comments is included below for the interested reader.

FLOW CHART OF NUMERICAL SCHEME

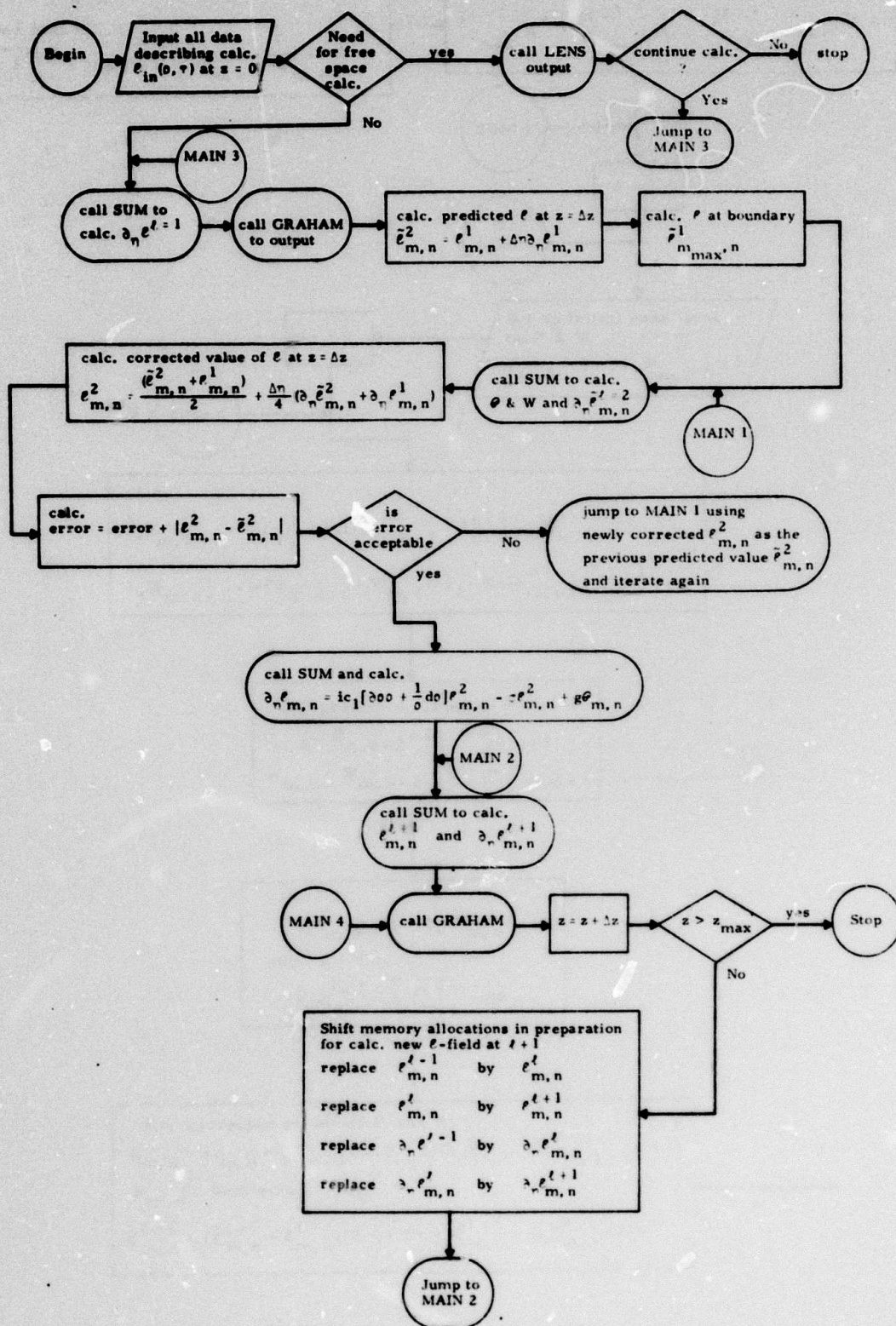


Fig. B1 - Main Subroutine

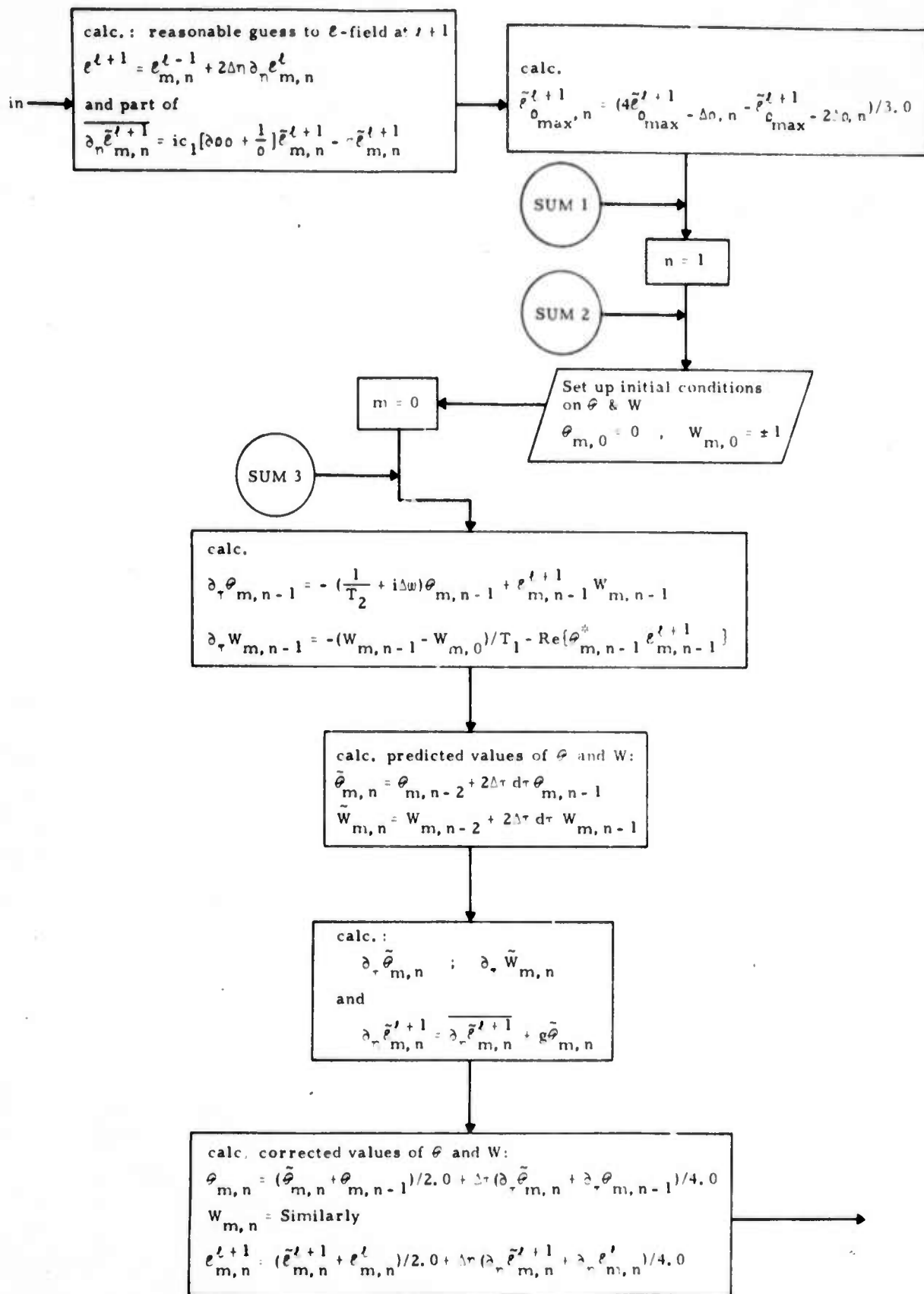


Fig. B2 - Integration Subroutine SUM

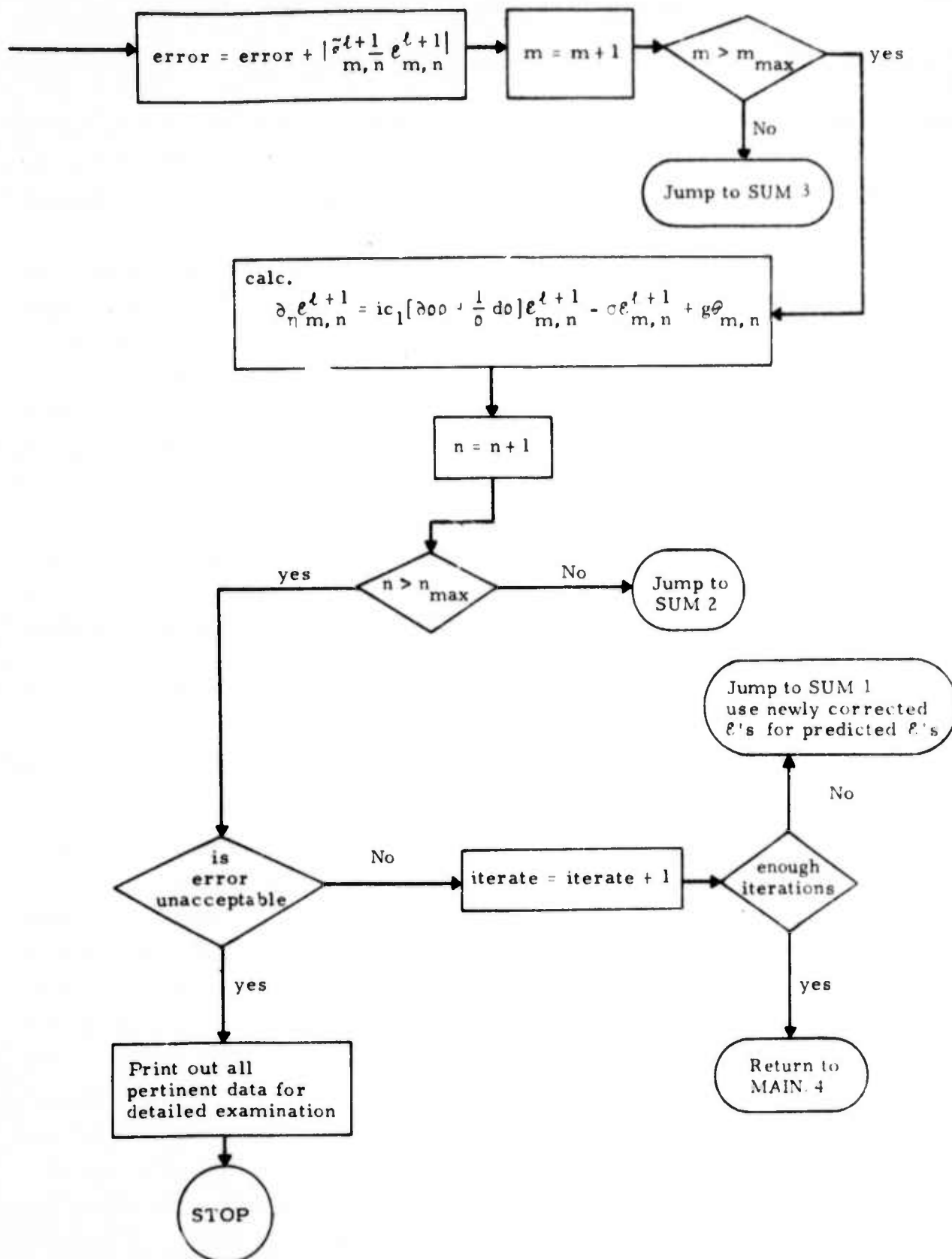


Fig. B3 - Integration Subroutine SUM

Stability analysis:

In real space time the reduced wave equation is

$$\partial_t \epsilon + \frac{c}{n} \partial_z \epsilon - ic_1 \nabla_0^2 \epsilon = g\theta \quad . \quad (B.3)$$

No matter what scheme is used to numerical integrate this equation, one should only gather information in the light cone of the input. There is the obvious physical restriction that we cannot numerically estimate the electric field at $t+\Delta t$, $z+\Delta z$ from the fields at t, z if $(c\Delta t/\Delta z) \geq 1$. If this is violated, it means the scheme is systematically introducing unphysical data which will lead to meaningless results (usually an instability). Thus a stability analysis of any scheme applied to Eq. (B.3) will have the conditional requirement $(c/n)(\Delta t/\Delta z) = \text{const} < 1$ in the limit $\Delta t, \Delta z \rightarrow 0$. A practical way to avoid this instability is to transform to a frame moving at velocity c/n . This procedure has been demonstrated by Hopf and Scully in their numerical work.⁽⁴⁾ This transformation has two important benefits from a numerical point of view. The transformation to this co-moving frame reduces by one the number of independent variables, thereby saving considerable calculation time. Another useful result of this transformation is that it automatically insures physically realizable discretized integration in the z, t plane. The transformation is defined as

$$\begin{cases} \tau = t - \frac{z}{c} \\ \eta = z \end{cases} \quad .$$

For any positive $\Delta\tau$ including the limit $\Delta\tau \rightarrow 0$, the ratio $(c\Delta t/\Delta z)$ is always greater than or equal to unity independent of the size of $\Delta\eta \equiv \Delta z$. Thus the stability with respect to η, τ is built into the integration scheme. A drawback of this type of transformation will occur when trying to handle pulses with velocities substantially different from c/n . Since only a finite number of time mesh points will be used to discretize the time domain, it follows the time window in the co-moving frame is finitely restricted. If a pulse has a velocity less than c/n , after passing through a calculable distance z into the media, the pulse will eventually drift out of this fixed time window. This could be compensated for by using a variable velocity co-moving frame. However, the code becomes more complex and time consuming. Fortunately, for the transient type problems we have analyzed, this difficulty does not restrict the numerical procedure. In approaching steady state, the problem becomes more serious.

The numerical scheme that we have used effectively treats the coupled equations like two coupled ordinary differential equations. While τ is held fixed, the field equation is marched in z by a Δz , and when z is held fixed, ψ and W are stepped in time τ . The stability analysis is applied to each of these processes separately and the combined criterion is applied to the coupled equations. It can be shown that for these equations, this result is valid as well as easy to apply. This result is more apparent once the analysis is demonstrated for the two separated calculations. A complete description of the methods of numerical stability is given in Richtmyer and Morton.⁵ The stability check is applied locally to the linearized equation. One of the separated integrations carried out is for the case $g = 0$. The reduced wave equation becomes a hyperbolic diffusion type equation with an imaginary diffusion constant " ic_1 ." After a Fourier series expansion of the discretized dependent variables, the finite difference equations can be assembled in the form

$$V^{n+1} = \overline{A} V^n$$

where V^{n+1} is the vector representation of the dependent variables at the mesh point z_{n+1} and \overline{A} is the so-called amplification matrix. The VonNeumann necessity condition for stability requires the amplification matrix to be bounded. This generally requires its eigenvalues to have absolute values less than or equal to unity. The detailed calculations and results are shown in the next section. The other effective ordinary differential equation will be the case where $c_1 = 0$ (the one-dimensional problem). The results of the 3-level predictor-corrector scheme (levels $n - \Delta n$, n , $n + \Delta n$) requires

$$v = \frac{2\Delta n c_1}{(\Delta \sigma)^2} \leq 0.49 \quad \{ \text{in our calc. we used } v = 0.33 \}$$

and no condition on $\Delta \sigma$, $\Delta \tau$ other than they be consistently small. Via numerical experimentation, we have found the cut-off value of v to be $v_c \approx 0.4$. Thus the local stability check comes reasonably close to the actual value (as is usually the case). Global instability almost always results from local instability. Included in the next section is a figure plotting the absolute values of the amplification matrix's two eigenvalues λ_+ and λ_- for various values of the critical parameter $v = (2\Delta n c_1 / (\Delta \sigma)^2)$. Again, stability requires $|\lambda| \leq 1$.

Stability check for p-c integration scheme

Case 1. $g = 0$ Reduced wave equation: $\partial_\eta e = k \partial_y^2 e$.

The 3-level finite difference solution for e is:

$$e_{j+1}^{n+1} = \frac{1}{2} [e_{j+1}^n + e_{j+1}^{n-1} + \frac{2\Delta\eta k}{(\Delta y)^2} \{e_{j+2}^n + e_j^n - 2e_{j+1}^n\}] + \frac{\Delta\eta k}{4(\Delta y)^2} [e_{j+2}^n + e_j^n - 2e_{j+1}^n + e_{j+2}^{n-1} + e_j^{n-1} - 2e_{j+1}^{n-1} + \frac{2\Delta\eta k}{(\Delta y)^2} \{e_{j+3}^n - 4e_{j+2}^n + 6e_{j+1}^n - 4e_j^n + e_{j-1}^n\}] ,$$

where $n \rightarrow \eta$ and $j \rightarrow y$. The Fourier series substitution is simply accomplished by letting

$$\lambda e e^{\pm i\kappa\Delta y} \quad \text{replace} \quad e_{j\pm 1}^{n+1} ,$$

$$e e^{\pm i\kappa\Delta y} \quad \text{for} \quad e_{j\pm 1}^n ,$$

and

$$S^n = e^{n-1} .$$

The resulting amplification matrix with this substitution is (2 x 2)

$$\overline{A} = \begin{bmatrix} a & b \\ -1 & \lambda \end{bmatrix} \quad \text{where} \quad \overline{A} \begin{bmatrix} e \\ S \end{bmatrix} = 0$$

and

$$a = \lambda - \frac{1}{2} + i \frac{5}{2} \gamma \sin^2 \left(\frac{\kappa\Delta y}{2} \right) + 2\gamma^2 \sin^4 \left(\frac{\kappa\Delta y}{2} \right)$$

and

$$b = -\frac{1}{2} + i \frac{\gamma}{2} \sin^2 \left(\frac{\kappa\Delta y}{2} \right) .$$

The characteristic equation is $a\lambda + b = 0$. After some straightforward algebra the absolute value of its roots are:

$$|\lambda \pm|^2 = \frac{1}{4} \{x_1^2 + y_1^2 + \sqrt{x_1^2 + y_1^2} \pm 2x_1 \left(\frac{x}{2} + \frac{1}{2} \sqrt{x^2 + y^2} \right)^{1/2} \pm 2y_1 \left(-\frac{x}{2} + \frac{1}{2} \sqrt{x^2 + y^2} \right)^{1/2} \} ,$$

where

$$x_1 = \frac{1}{2} + 2\gamma^2 \sin^4\left(\frac{\kappa\Delta y}{2}\right) ,$$

$$y_1 = -\frac{5}{2}\gamma \sin^2\left(\frac{\kappa\Delta y}{2}\right) ,$$

$$x = \frac{9}{4} - \frac{33}{4}\gamma^2 \sin^4\left(\frac{\kappa\Delta y}{2}\right) + 4\gamma^4 \sin^8\left(\frac{\kappa\Delta y}{2}\right) ,$$

and

$$y = -\frac{9}{2}\gamma \sin^2\left(\frac{\kappa\Delta y}{2}\right) + 10\gamma^3 \sin^6\left(\frac{\kappa\Delta y}{2}\right) .$$

For all real values of γ and κ , the sin is restricted to the range

$$0 \leq \sin^2\left(\frac{\kappa\Delta y}{2}\right) \leq 1 .$$

The absolute values of the roots $|\lambda \pm|$ are plotted over this range in Fig.

B.4.

Case 2. $c_1 = 0$ coupled one-dimensional linearized system equations are:

$$\partial_\eta \ell = -\sigma \ell + g \theta$$

$$\partial_\tau \theta = -\alpha \theta - a \ell + b W$$

$$\partial_\tau W = k_0 - \beta W - c \ell - d \theta .$$

After writing the complete three-step complete discretized equations for ϕ_{n+1}^{j+1} , W_{n+1}^{j+1} , and ℓ_{n+1}^{j+1} and substituting $\lambda i x e^{\pm i \kappa \Delta \tau}$ for $i x_{n \pm 1}^{j+1}$ yield,

$$\lambda W \left[e^{i \kappa \Delta \tau} - \frac{1}{2} - \frac{e^{-i \kappa \Delta \tau}}{2} \right] + \Delta \tau [\dots] = 0 ,$$

$$\lambda \theta \left[e^{i \kappa \Delta \tau} - \frac{1}{2} - \frac{e^{-i \kappa \Delta \tau}}{2} \right] + \Delta \tau [\dots] = 0 ,$$

$$\lambda \ell = \frac{\ell}{2} + \frac{S}{2} ,$$

and

$$\lambda S = \ell .$$

Where ℓ corresponds to η and n corresponds to τ . Letting $\Delta \tau, \Delta \eta \rightarrow 0$ yield

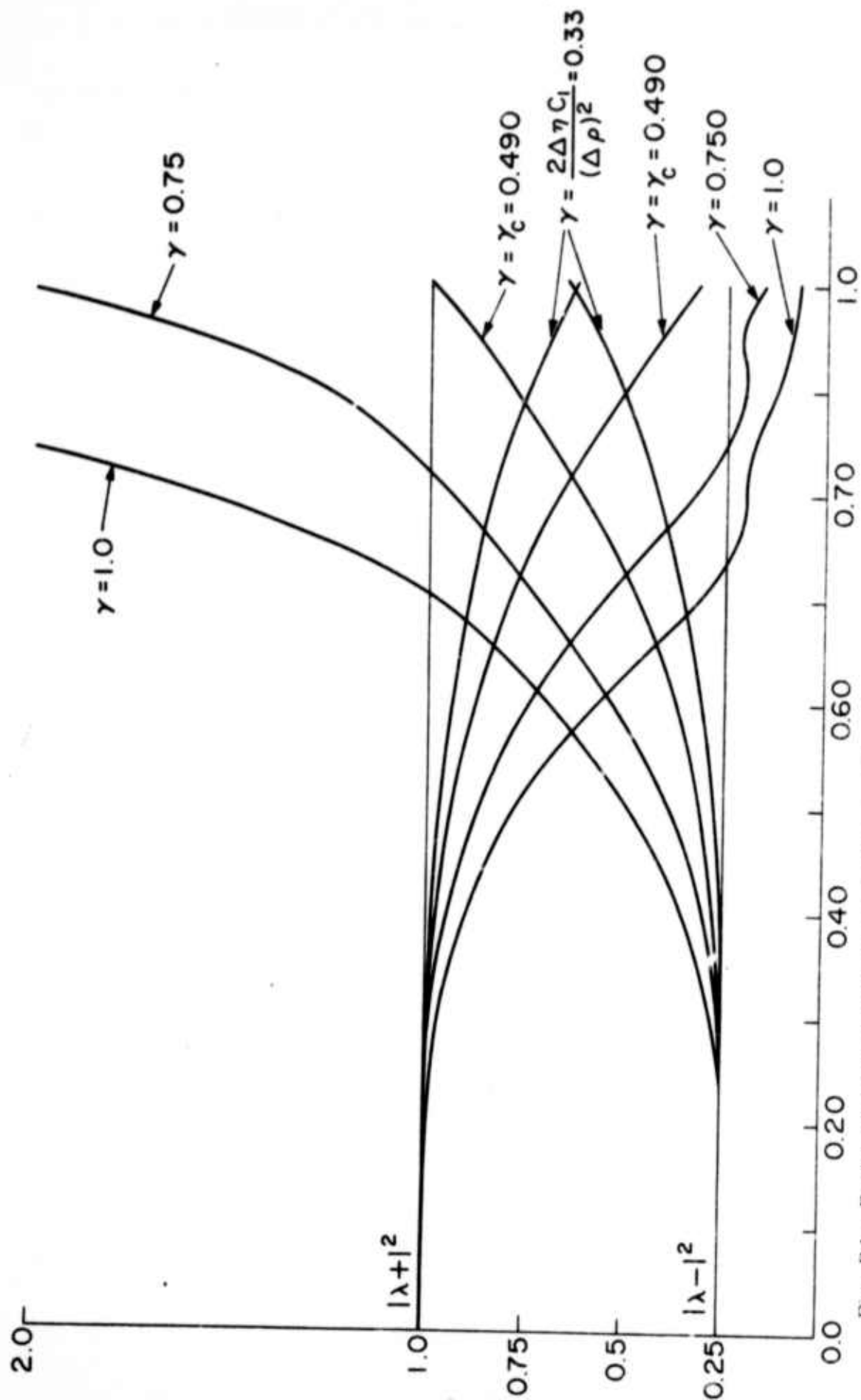


Fig. B4 - Evaluation of the eigenvalues for the amplification matrix of the numerical scheme. The numerical method was a two level predictor-corrector. The eigenvalues are $|\lambda+|$ and $|\lambda-|$ and the finite difference critical parameter is $\gamma = 2\Delta\tau C_1/(\Delta\rho)^2$. A stable finite difference scheme requires the eigenvalues to be less than unity absolute value.

$$\lambda_{\pm} = \frac{(1/2) \pm \sqrt{(1/4)+2}}{2} \leq 1 \quad .$$

This verifies the stability of τ, η integrations. We note that no mutual restrictions are placed on $\Delta\tau, \Delta\eta$ as noted in text on physical grounds.

REFERENCES

1. A. Icsvgi and W.E. Lamb, Jr., "Propagation of Light Pulses in a Laser Amplifier," Phys. Rev. Vol. 185, pp 517-45, 1969.
2. N. Wright, "Pulse Propagation in Non-Linear Resonant Media," Ph.D. Dissertation, Department of Electrical Engineering/Electrophysics, Polytechnic Institute of New York, 1974.
3. Private communication, Prem Khosla.
4. F.A. Hopf and M.O. Scully, "Theory of an Inhomogeneously Broadened Laser Amplifier," Phys. Rev. Vol. 179, pp. 399-416, 1969.
5. R.D. Richtmyer and K.W. Morton, Difference Methods for Initial Value Problems, 2nd Ed., Interscience Publ., New York, London, and Sydney, 1967.